# Cambrian foreland phosphogenesis in the Khuvsgul Basin of Mongolia

**Eliel S. C. Anttila[1a*], Francis A. Macdonald[1b], Blair Schoene[2], and Sean P. Gaynor[2c]**
[1]*Department of Earth Science, University of California Santa Barbara, Santa Barbara, CA, 93117, USA*
[2]*Department of Geosciences, Princeton University, Princeton, NJ, 08544, USA*
[a]*Now at the Department of Earth Sciences, ETH Zürich, Zürich, 8092, CH*
[b]*Now at the Department of Earth and Planetary Science, University of California Berkeley, Berkeley, CA, 94720, USA*
[c]*Now at the Geology, Geophysics, and Geochemistry Science Center, United States Geological Survey, Denver, CO, 80225, USA*
**Corresponding author: eanttila@ethz.ch*

**ABSTRACT**
Ediacaran-Cambrian phosphorite deposits in northern Mongolia have been associated with a putative increase in nutrient delivery to the global oceans that drove oxygenation and the rise of animals. However, like many phosphorites from this ~130 Myr interval, the precise age and depositional setting of these deposits remain poorly constrained. Here, we integrate new geological mapping, lithostratigraphy, chemostratigraphy, and U-Pb zircon geochronology to develop a new age and tectonic basin model for the Cryogenian to Cambrian Khuvsgul Group of northern Mongolia. We demonstrate that Cambrian strata were deposited into two composite foreland basins: a ~535-524 Ma pro-foreland basin formed during collision of the Khantaishir-Agardag oceanic arc, and a younger ~523-505 Ma retro-arc foreland developed behind the Ikh-Mongol continental arc. The Kheseen Formation phosphorites, which include a Doushantuo-Pertatataka-type microfossil assemblage, were deposited in the pro-foreland basin between 534 and 531 Ma, at least 40 million years later than the phosphatized Weng'an Biota of the Doushantuo Formation of South China. Tectonically-mediated basinal topography associated with foreland development was a necessary condition for phosphogenesis along the Tuva-Mongolia-Zavkhan margin, with different styles of phosphate mineralization associated with sediment starvation and migrating redox boundaries across the margin. The apparent Ediacaran-Cambrian increase in preserved phosphorite deposits was not an event associated with an increase in nutrient delivery to the oceans, but rather represents the opening of a taphonomic window in which a long-term, sustained increase in redox potential enabled increased authigenic phosphate accumulation over a protracted period in marginal marine environments with the requisite tectono-stratigraphic and sedimentological conditions.

## 1. INTRODUCTION

On geological timescales, phosphate is thought to be a limiting nutrient of bioproductivity (Tyrrell, 1999), with phosphorus fluxes in Earth's surface environments responding to changes in both silicate weathering (Hartmann and Moosdorf, 2011; Horton, 2015) and environmental redox state (Dodd et al., 2023; Ruttenberg, 2003; Colman and Holland, 2000). The stratigraphic record preserves an apparent global increase in the size, grade, and frequency of concentrated phosphate deposits, or phosphorites, near the Ediacaran-Cambrian boundary

(Cook, 1992; Cook and McElhinny, 1979). Ediacaran-Cambrian phosphorites have been found in Asia (Ilyin and Zhuraleva, 1968; Ilyin and Ratnikova, 1981; Anttila et al, 2021; Meert et al., 2011; Xiao and Knoll, 1999; Sergeev et al., 2020; Banerjee et al., 1980; Mazumdar et al., 1999), Africa (Flicoteaux and Trompette, 1998; Bertrand-Sarfarti et al., 1997), Australia (Valetich et al., 2022; Southgate, 1980) and South America (Misi and Kyle, 1994; Shiraishi et al., 2019; Sanders and Grotzinger, 2021; Morais et al., 2021), and include some of the largest known phosphate deposits in the world (Cook and Shergold, 1986). These occurrences have inspired hypotheses that link a global increase in phosphate deposits around the Ediacaran-Cambrian boundary to changes in nutrient fluxes to the oceans (Papineau, 2010), concomitant oxygenation of the Earth's surface (Reinhard et al., 2017; Laakso et al., 2020), and the rise and expansion of life (Shields et al., 2000).

However, phosphorus delivery to the oceans (Föllmi, 1996) is only one potential controlling aspect of phosphogenesis: sedimentological (Föllmi, 1990; Föllmi et al 2005; 2017), paleotopographic (Föllmi et al., 2017), and biogenic (Sanders et al., 2024; Schulz and Schulz, 2005) factors have been shown to control the locus and concentration of phosphate accumulation in phosphogenic environments. To this end, detailed investigations that constrain the age, duration, and depositional context of individual phosphorite localities are a prerequisite of any holistic model for the drivers of Ediacaran-Cambrian phosphogenesis. Furthermore, constraining the age of Ediacaran-Cambrian phosphorites is particularly important given the taphonomic potential of phosphogenic environments: early authigenic precipitation of phosphate minerals (dominantly calcium fluorapatite, or CFA) can result in the exceptional preservation of biogenous material, including soft-bodied organisms and putative animal embryos (Xiao et al., 1998). Phosphatized lagerstätten, such as the Weng'an biota of the Doushantuo Formation (Xiao and Knoll, 2000) and the Portfjeld Formation, northern Greenland (Willman et al., 2020) provide some of the best windows into the evolution and expansion of metazoans around the Ediacaran-Cambrian boundary.

The Khuvsgul Group of northern Mongolia (Ilyin and Ratnikova, 1981; Anttila et al., 2021) contains one of the largest ore-grade phosphorites in the world (Ilyin, 1973; Munkhtsengel et al., 2021), and hosts glacial diamictites associated with Cryogenian Snowball Earth glaciations (Macdonald and Jones, 2011) as well as a diverse Doushantuo-Pertatataka-Type microfossil assemblage (Anderson et al., 2017; 2019). Although the Khuvsgul Group has been the subject of geological investigation for more than half a century (Donov et al., 1967), age models for these strata rely on biostratigraphy (Ilyin and Zhuraleva, 1968; Korobov, 1980; 1989; Zhegallo et al., 2000; Demidenko et al., 2003, Korovnikov and Lazarev, 2021), which is of limited used in the Neoproterozoic and Early Cambrian. Lithostratigraphic correlations to radiometrically-dated sections elsewhere provide additional age constraints on the Khuvsgul Group (Macdonald and Jones, 2011).

Here, we develop a new age model for the Khuvsgul Group by combining new lithostratigraphic observations, carbonate chemostratigraphy, and U-Pb zircon geochronology from the Khuvsgul region. This framework is paired with new geologic mapping and structural data to create a tectonic basin model for the Khuvsgul Group. Within the context of this model, we compare Khuvsgul Group strata to adjacent Cryogenian to Cambrian strata of the Zavkhan Terrane in southwest Mongolia (Bold et al. 2016a, b, Smith et al. 2016, Macdonald and Jones, 2011, Macdonald et al., 2009), and explore how differences in sedimentology and basin morphology may have impacted the mode of phosphogenesis observed in each basin. Finally, our chronostratigraphic model provides new age constraints on the phosphatic lagerstätten of the Kheseen Formation (Fm) of the Khuvsgul Group, which are then discussed in relation to other Doushantuo-Pertatataka-Type microfossil assemblages and Ediacaran-Cambrian phosphorites from around the world.

## 2. GEOLOGIC BACKGROUND

### *2.1 Tectonic setting of the Khuvsgul Group*

The Khuvsgul Group comprises the Cryogenian-Cambrian sedimentary cover of the Khuvsgul Terrane, which forms the central component of an amalgamated composite terrane previously referred to as the Tuva-Mongolia Massif (Ilyin, 1971), the Tuva-Mongolia Microcontintent (TMM; Kuzmichev, 2015), Central Mongolian Terranes (CMT; Domeier, 2018), and our preferred nomenclature of the Tuva-Mongolia Terrane (TMT; Bold et al., 2019). The TMT (fig. 1) is embedded within the Central Asian Orogenic System (CAOS; Kröner et al., 2007; Windley et al., 2007; Kröner et al., 2014), which formed through collision and accretion of arcs, oceanic tracts, and microcontinental fragments from the late Mesoproterozoic (Khain et al., 2002) to late Paleozoic (Xiao et al., 2003; Windley et al., 2007; Wilde, 2015).

The oldest rocks in the TMT are 2702 ± 6 Ma basement gneisses (the Salig Complex) of the Gargan Block (U-Pb LA-ICPMS on zircon, Bold et al., 2019). During the Tonian Period, volcanic and ophiolitic rocks associated with the ~1000 Ma Dunzhugur arc (Khain et al., 2002) were obducted along the northern TMT margin prior to the emplacement of the Sumsunur Complex, which includes tonalite-trondjeimites that have been dated to 785 ± 11 Ma (Kuzmichev et al., 2001), and potentially during 814 ± 10 Ma metamorphism of the Salig Complex (Bold et al., 2019). The Sumsunur Complex is an intrusive complement to volcanic, rocks of the coeval Sarkhoi Fm (Kuzmichev and Larionov, 2011), which have also been correlated with volcanic rocks of the Zavkhan Fm (see Bold et al., 2016b) in southwest Mongolia. Geochemical data suggest that volcanic rocks of the Zavkhan and Sarkhoi Fms formed a continental arc system across both terranes (Kheraskova et al., 1995; Kuzmichev et al., 2001; Kuzmichev, 2015, Bold et al. 2016b).

### *2.3 Cryogenian-Cambrian stratigraphy of the Tuva Mongolia Terranes: The Khuvsgul Group*

Carbonate, siliciclastic, and volcaniclastic rocks of the Khuvsgul Group overlie the Sarkhoi Fm (and coeval siliclastic and volcaniclastic rocks of the Darkhat Group). Here, we build on the stratigraphic framework developed from the Khuvsgul region of the TMT (fig. 2; Anttila et al., 2021) with new chemostratigraphic, lithostratigraphic, and sequence stratigraphic data.

The Cryogenian strata of the Khuvsgul Group include two diamictites separated by a carbonate sequence, which have been correlated with the Cryogenian Sturtian and Marinoan Snowball Earth glaciations and the middle Cryogenian, respectively (Macdonald and Jones, 2011). The laterally-variable thicknesses of Cryogenian strata on the Khuvsgul Block have been interpreted to reflect syn-depositional topography: it has been proposed that the Sturtian Ongolog diamictite was deposited along active Tonian to Cryogenian rift shoulders (Osokin and Tyzhinov, 1998; Macdonald and Jones, 2011).

Much of the early geologic inquiry in the Khuvsgul region (Donov, et al., 1967; Ilyin, 1973, 2004; Osokin and Tyzhinov, 1998) focused on the phosphatic strata of the Kheseen Fm, which are stratigraphically above the Cryogenian sequence and make up one of the largest economic-grade phosphorite deposits in the world (Cook and Shergold, 1984). Trenches and roadcuts from prospecting are still visible, but economic development of mineral resources in the area was prevented initially by the remote location of the Khuvsgul region, and more recently by the recognition of the environmental fragility of the surrounding ecosystem. In addition to their economic significance, phosphorites of the Kheseen Fm host a Doushantuo-Pertatanka-Type microfossil assemblage (Anderson et al., 2017, 2019), with fossiliferous strata located in the eastern Khoridol Saridag mountain range, on the western shores of Lake Khuvsgul (fig. 3).

The phosphatic strata of the Kheseen Fm are separated from the underlying Cryogenian units by a thin package of Ediacaran carbonate, lutite, and shale (fig. 2). For this reason, previous workers argued for a genetic relationship between Cryogenian glacial episodes and the phosphorite deposits (Sheldon, 1984; Osokin and Tyzhinov, 1998; Ilyin, 2004). However, a disconformity surface first recognized by Ilyin (2004) at several sites around the basin may be potentially correlative to an Ediacaran hiatus observed in the Zavkhan Terrane (Macdonald et al., 2009; Bold et al., 2016a), casting doubt upon glaciogenic interpretations of phosphogenesis in the Khuvsgul basin.

The upper Khuvsgul Group includes the ~2 km-thick carbonate succession of the Erkhelnuur Fm, which disconformably overlies the Kheseen Fm. Reported trilobite and archaeocyathid occurrences within the Erkhelnuur Fm (Korobov, 1989) suggest a Cambrian age for this interval. A coarse siliciclastic unit, the Ukhaatolgoi Fm, overlies the Erkhelnuur Fm, and is the youngest pre-Cenozoic sedimentary sequence on the TMT. The accumulation of the Cambrian platformal carbonate sequence of the Khuvsgul basin has been attributed to continued thermal subsidence along the TMT margin (Khukhuudei et al, 2020; Kuzmichev, 2015), and deposition into a riftogenic graben (Ilyin, 2004). Conversely, Macdonald and Jones (2011) suggest that, like on the Zavkhan Terrane, Cambrian subsidence on the TMT margin was driven by collisional tectonics related to the Salarian Orogeny (Ruzhentsev and Burashnikov, 1995; Smith et al., 2016; Bold et al., 2016b).

### *2.4 Phanerozoic deformation of the Tuva Mongolian Terranes*

Khuvsgul Group strata in the Khoridol Saridag Range (fig. 1) were previously mapped as km-scale south-plunging, north-south-trending anticlinoria (Buihover et al., 1968; Mongolian Survey, 1988), intruded by Ordovician post-metamorphic monzogranites and granodiorites (Kuzmichev, 2015). However, these pre-Ordovician structures have not been explicitly associated with a specific collision or compressional event, highlighting the need for detailed structural characterization of the greater Khuvsgul region. Following early Paleozoic deformation, TMT-Siberian sutures were reactivated and intruded by Carboniferous and early Permian plutons (Buslov et al., 2001; 2009). The Neogene development of the Baikal Rift system resulted in the generation of new N-S trending normal fault structures and basaltic magmatism in the Khuvsgul region. The Neogene extensional regime also reactivated extant older structures, leading to block rotation along older faults in the region. Seismic activity along both normal and sinistral transverse structures in the Khuvsgul region continues today (Liu et al., 2021).

## *3. METHODS*

### *3.1 Geological mapping and stratigraphy*

Over the course of three field seasons, we mapped the geology of the Khuvsgul region of the TMT, with an emphasis on exposures of the Khuvsgul Group in the Khoridol Saridag Range and Darkhat Valley (fig. 1C). Outcrop mapping was performed using FieldMove software on Apple iPads. Structural measurements and field photographs were also taken and geotagged within the FieldMove program. Shapefiles generated from outcrop mapping and structural measurements were imported into QGIS and used, in addition to satellite imagery and scanned geologic maps from previous workers (Buihover et al., 1968; Mongolian Survey, 1988), as constraints for the placement of structures and contacts in our geologic map of the region. Stratigraphic sections were measured with a meter-stick; the locations of all measured sections referenced in this manuscript are collated in the Supplementary Information (Table S1).

### *3.2 Bulk carbonate carbon and oxygen isotope analyses*

Carbonate rocks were collected for stable carbon and oxygen isotope ($\delta^{13}C$ and $\delta^{18}O$) analyses within measured sections throughout the field area. Limestone and dolomite hand samples (200-500 g) were collected at 0.5 to 2 m intervals within selected measured sections, with samples chosen from outcrops with minimal evidence of late-stage alteration. Each collected sample was shipped back to the University of California, Santa Barbara and cut into slabs with a rock saw, with slab surfaces cut orthogonal to bedding features. Approximately 1 mg of carbonate powder was then procured from each slab via microdrilling (0.5 mm bit on a vertical press), with a focus on producing a representative and reproducible powder aliquot for each sample: samples with laminar bedding features were drilled along single bedding surfaces whenever possible, and micritic matrix material was targeted for allodapic samples. Drilled slabs were labeled and stored. All $\delta^{13}C$ and $\delta^{18}O$ data are collated in the Supplementary Information (Table S2), while details of analytical procedures are summarized in the Appendix.

### *3.3 U-Pb zircon geochronology*

Samples for U-Pb zircon geochronology were collected during the course of mapping. Zircons derived from each sample were analyzed with laser ablation inductively coupled plasma mass spectrometry (LA-ICPMS), and a subset of zircon from igneous samples, as well as young zircon grains from detrital samples, were analyzed with chemical abrasion isotope dilution thermal ionization mass spectrometry (CA-ID-TIMS). Results are summarized below, and are collated, along with sample locations, in the Supplementary Information (Table S3). Mineral separation and analytical methods are detailed in the Appendix.

## 4. RESULTS

### *4.1 Lithostratigraphy and facies associations of the Khuvsgul Basin*

The Khuvsgul Group, formalized by Anttila et al. (2021), is divided into the Ongolog, Bakh, Shar, Khirvesteg, Kheseen, and Erkhelnuur Fms, with the Bakh and Erkhelnuur Fms further divided into three Members (Mbs). The Khuvsgul Group is underlain by the volcanic, volcaniclastic, and siliciclastic rocks of the Darkhat Group, which includes the Sarkhoi and Arasan Fms, and is overlain by siliciclastic rocks of the Ukhaatolgoi Fm.

Lithofacies of the Khuvsgul Group and bounding units are described below. These descriptions inform interpretations of the depositional environments of each unit, which are subsequently incorporated into a general tectonostratigraphic model for the Khuvsgul Group in Section 5.4.

*Sarkhoi Formation description.* – The Sarkhoi Fm outcrops in the Khoridol Saridag Range and Darkhat Valley, and consists of purple, red, and green fine-grained rhyolite and rhyodacite flows, ignimbrites, volcaniclastic breccias, siltstone, fine-grained sandstone with linguoid and lunate ripples, and feldspathic and lithic wacke. The Sarkhoi Fm is estimated to be

~4 km thick near the Zabit River of southern Siberia (Kuzmichev, 2015), whereas the maximum thickness in the Khoridol-Saridag Range and Darkhat Valley is ~1.5 km.

*Sarkhoi Formation interpretation*. – Although the Sarkhoi Fm has been interpreted to have formed in a rift setting (Ilyin 1973, 2004), geochemical characterizations of volcanic rocks of the Sarkhoi Fm suggest a continental arc affinity (Kuzmichev and Larionov, 2011), with east-dipping subduction inferred to have occurred along the western margin of the TMT (Kuzmichev, 2015). In the Khuvsgul region, the close association of volcanic flows and ignimbrites with a suite of siliciclastic rocks records volcanic flows interfingering with a marginal marine depositional environment, suggesting the proximity of an actively-subsiding basin adjacent to an active volcanic edifice.

*Arasan Formation description*. – Above the Sarkhoi Fm, the Arasan Fm outcrops as tan-to-brown laminated siltstone with occasional 1–3 cm fining-upward packages of medium- to coarse-grained quartz arenite to sublitharenite. In the lower Arasan Fm, discontinuous quartz-rich granule to pebble lags occur within fine-grained sandstone or shale layers directly above thicker sandstone beds. 10–20 cm thick recrystallized dolomite beds punctuate the uppermost ~100 m of very fine-grained sandstone and siltstone, with minor coarse-grained sandstone beds intercalated throughout the uppermost portion of the section. Poor exposure precludes both the measurement of a complete stratigraphic section through the Arasan Fm, as well as identification of the basal contact.

*Arasan Formation interpretation*. – Though the contact with the underlying Sarkhoi Fm is not exposed, the well-sorted, moderately-mature siliciclastic rocks of the Arasan Fm likely indicate a transition, from mass-wasting-dominated deposition in an actively subsiding basin during Sarkhoi Fm time, to shoaling, the development of mature sediment sources, and deposition within a more-quiescent marginal environment. The close association of shales and laterally-continuous graded sandstones in the upper Arasan Fm suggests a marine shelf-margin to upper slope depozone, with episodic instability on the shelf and upper slope driving both gravity-flow and suspension-dominated deposition.

*Ongolog Formation description*. – Intercalated graded and massive sandstone, siltstone, and shale horizons of the basal Ongolog Fm are populated up-section by increasing numbers of lonestones, forming a stratified, matrix-supported diamictite. The base of the Ongolog Fm is rarely exposed: at Kheseen Gol, the ochre to tawny-brown well-sorted siltstone and sandstone of the upper Arasan Fm grades into poorly-sorted green and purple siltstone and wacke of the overlying Ongolog Fm. However, this contact has been reported to be unconformable elsewhere in the region (Osokin and Tyzhinov, 1998). In some cases, the Arasan Fm is completely absent from the stratigraphy, with the basal Ongolog Fm directly overlying volcanics of the Sarkhoi Fm (Kuzmichev et al, 2001). In the Khoridol Saridag Range, with the exception of the exposures described above, the base of the Ongolog Fm is faulted.

The most complete Ongolog sections outcrop in the easternmost exposures of the Khoridol Saridag Range, where the basal clast-free portion of the Ongolog Fm is up to 400 m thick, and the overlying diamictite ranges from 100 – 250 m thick. The lower, clast-free interval is exposed along the northern ridge bordering the eponymous Ongolog Gol (fig. 3), with poorly sorted, green to tawny-brown wacke transitioning up-section into olive to dark-brown siltstone with discontinuous lenses of medium-grained sandstone to poorly-sorted granule conglomerate, and thin beds of blue to dark gray micritic limestone. Arkosic wackes that make up the coarser sandstone beds include subangular quartz and plagioclase grains amidst a fine-grained green to brown matrix.

Up-section, sparse, rounded to subangular quartzite and carbonate granule-to-cobble lonestones are suspended in laminated green to brown siltstone and fine-grained sandstone beds. The frequency and maximum size of outsized clasts increases dramatically in the top ~200 m of section, with nearly continuous exposure on the ridge north of Kheseen Gol (Macdonald and Jones, 2011). In the easternmost Khoridol Saridag Range, the top ~100 m of the Ongolog Fm is composed of a matrix-supported, polyclastic, stratified diamictite. Clasts include rounded to sub-angular gravel to cobbles of quartzite, plutonic and volcanic rocks, and carbonates, and are locally observed to be faceted and striated (Osokin and Tyzhinov, 1998). The upper 30-50 m of the Ongolog Fm consists of resistant, dark-weathering, argillite-matrix-supported diamictite dominated by subrounded dolomite clasts with minor quartzite and granite clasts. This facies, termed the "perforated shale" by Ilyin (1973), is most dramatically exposed along the banks of Ongolog Gol, where dolomite clasts are recessively weathered, leaving pockmarked holes in the black argillite matrix (fig. 4A). A different facies of the uppermost Ongolog diamictite outcrops to the west in the Darkhat Valley, where only the top of the formation is exposed: subangular quartzitic, plutonic, and volcanic cobbles are supported in a dark brown massive sandstone matrix.

*Ongolog Formation interpretation*. – The Ongolog Fm has been assigned to the ~717-661 Ma Sturtian Snowball Earth glaciation (Macdonald and Jones, 2011). Striated and faceted clasts within diamictites of the Ongolog Fm (Osokin and Tyzhinov, 1998) support a glaciogenic origin. The gradational transition from clast-free shales and wackes at the base of the unit to stratified or massive diamictite at the top likely represents the evolution of a subaqueous glaciomarine depositional environment, with stratified diamictites interpreted as flow tills deposited in front of a marine ice-grounding line. It is unclear if the clast-free basal portion of the Ongolog Fm was deposited in open water or below an ice shelf, but the gradational contact with the overlying diamictite suggests the latter: initial sparse outsized clasts seen lower in the section, many of which truncate bedding planes, are likely ice rafted debris. An up-section increase in clast frequency, from isolated lonestone-bearing horizons amidst clast-free laminated shales to stratified diamictite without much evidence for bed-penetrating clasts, indicates the advance of the ice grounding line towards the depozone.

*Bakh Formation*. – Composed of variably laminated limestone and dolomite grainstone and rhythmite (finely laminated, graded beds of calcisiltite and micrite), the Bakh Fm is subdivided into three lithologically distinct Mbs.

*Khurts Member description*. –The Khurts Mb of the Bakh Fm is dominated by heavily recrystallized carbonate strata that form resistant ridges in the Khoridol Saridag Range. Its thickness increases, from ~20 to >110 m, east to west across the Khoridol Saridag Range. Dolomite and limestone micrite and calcisiltite of the Khurts Mb sharply overlie the Ongolog diamictite. Above this cap carbonate, the Khurts Mb is composed of homogenous <2 m-thick dolomitized wackestone beds separated by <40 cm-thick allodapic dolomite grainstone beds that occasionally contain sub-rounded < 1 cm carbonate clasts. Up-section, wackestone beds thin to ~1 m, with interstitial 50-70 cm intervals of finely-laminated, 1-2 cm grainstone beds containing subrounded carbonate clasts, small ooids, and rare domal stromatolites. Coarse grainstone beds increase in frequency up-section.

*Khurts Member interpretation*. – The sharp transition from the Ongolog Fm diamictite to laminated carbonate rocks of the Khurts Mb is interpreted as a flooding surface associated with eustatic sea-level rise following the termination of the Sturtian glaciation. Facies associations of the Khurts Mb are consistent with deposition in a subtidal marginal marine setting on a carbonate ramp. A shift from laminated micrite in the basal portion of the Khurts Mb to coarser wackestone and grainstone up-section suggests a transition from an outer-ramp to middle-ramp environment (Burchette and Wright, 1992). Infrequent, tabular carbonate allochems in some of the thicker grainstone beds towards the top of the Khurts Mb are interpreted as rip-up clasts, which, along with the occurrence of domal stromatolitic horizons in adjacent grainstone beds, are interpreted to reflect cyclic shoaling in a relatively energetic upper middle-ramp depositional setting. This interpretation is further supported by the appearance of ooids as allochems within some of the larger grainstone beds, suggesting relative proximity and/or intermittent sediment transport connectivity to shallow, energetic environments above fair-weather-wave base.

*Bumbulug Member Description*. – The base of the Bumbulug Mb of the Bakh Fm is marked by a sharp transition from recrystallized dolomite wackestone and grainstone of the uppermost Khurts Mb to limestone micrite-wackestone, lutite, and rhythmite interbeds. In the eastern Khoridol Saridag Range, grainstone and rhythmite beds are stippled with <3 cm-long ellipsoidal black and grey chert nodules, creating a dappled, almost spongelike appearance on the tan- to grey-weathering limestone beds. Chert nodules are concentrated primarily in micrite beds and are associated with 1-3 mm-thick chert interbeds in adjacent rhythmite and lutite. Rare chert-free micrite and wackestone beds weather dark grey in contrast to tan-weathering chert-bearing carbonates. Exposures of the Bumbulug Mb in the western Khoridol Saridag Range and the Darkhat Valley contain less chert. Parasequences of micrite and lutite to grainstone and wackestone range in thickness from 0.8-2 m. Towards the top of the Bumbulug Mb, wackestone becomes the dominant component of each parasequence. The thickness of the Bumbulug Mb is ~100-150 m across an east-west transect of the central Khoridol-Saridag Range (KSR map area, fig. 3), <50 m in the southern Khoridol Saridag Range and Eg Gol regions (fig. 1B), and >350 m near Bayan Zurgh (fig. 1B), south-southwest of the Darkhat Valley.

*Bumbulug Member interpretation*. – The base of the Bumbulug Mb is marked by an abrupt shift from relatively energetic, peritidal to shallow-subtidal grainstone and wackestone to finely-laminated micrite and lutite. This shift is interpreted as a deepening, from a peritidal to shallow-subtidal carbonate ramp environment to a deeper, less energetic outer ramp setting, below storm-wave base. This transgressive sequence is followed by abundant wackestone and massive mudstone, interpreted to record a return to more energetic, gravity-driven depositional processes in a mid-ramp environment. Despite a substantial increase in stratigraphic thickness to the south-southwest, up-section facies trends are similar throughout the region, with globular chert-bearing micrite overlain by shallowing-upward parasequences at all complete Bumbulug Mb exposures.

*Salkhitai Member description*. – The Salkhitai Mb of the Bakh Fm consists of interbedded limestone grainstone, micrite, and occasional dark, fetid rhythmites, transitioning into coarsening-upward dolomitized grainstone, intraclast breccia, and massive carbonate breccia intervals that include scattered lithic grains. Best exposed and preserved in the Khoridol Saridag Range, dark-colored limestone strata near the base of the Salkhitai Mb consist of ~1.5-2 m-thick parasequences of laminated micrite capped by wackestone and grainstone beds that contain edgewise breccia and ooids in channelized bodies.

Up-section, parasequences are increasingly dominated by wackestone and grainstone, and are capped by carbonate breccia. Fining-upward wackestone and grainstone beds with 5-cm diameter grey chert nodules become increasingly abundant up-section. Fine- to medium-grained, subrounded to subangular quartz and lithic fragments are dispersed throughout the uppermost limestone unit within fining-upwards wackestone and grainstone beds.

This influx of terrigenous material occurs directly before a shift to dolomitized grainstone beds with ~1cm-thick discontinuous bands of nodular black chert, followed by chaotically bedded conglomerates that include dolomite, chert, and quartz and lithic grains. The uppermost portion of the Sakhitai Mb contains massive coarse-grained sandstone with outsized carbonate and lithic clasts, up to granule in size, followed by a dolomite grainstone bed. The sandstone, as well as an erosional surface at the top of the dolomite grainstone, are both best exposed in the eastern Khoridol Saridag Range, particularly at the Bakh Gol section. Thickness of the Salkhitai Mb ranges from ~100-150 m across the basin.

*Salkhitai Member interpretation*. – Rhythmite-grainstone parasequences (fig. 5A) at the base of the Salkhitai Mb are consistent with cyclic carbonate shoaling in a sub-tidal, mid-to-upper ramp environment, with facies associations trending up-section towards increasingly energetic, proximal depositional environments. Episodic reworking and incorporation of carbonate and chert into intraclast breccias suggests deposition near or above storm-wave base, and/or repeated shoaling into a more energetic depositional regime, above fair-weather-wave base. Up-section, channelization and an increase in terrigenous allochems indicate continued shallowing into an upper-ramp or shoreface depositional environment. The deposition of grainstones and carbonate conglobreccias indicates the continued influence of mass-wasting processes, caused either by the migration of tidal channels or by sea-level forced banktop instability. Sandstone beds near the top of the Salkhitai Mb have an erosive contact with the underlying grainstone interval, and are interpreted as bypass channels (e.g. Smith et al., 2016).

*Shar Formation description*. – The Shar Fm is composed of matrix-supported massive diamictite containing carbonate and exotic angular to sub-rounded clasts (0.1–1.2 m) in a cream-to-yellow weathering, gray-when-fresh fine-grained carbonate matrix (fig. 4B) with minor thin lutite and shale. Although clasts are dominated by angular to sub-angular micritic dolomite, similar to that observed in the most proximal underlying strata, limestone rhythmite, oolite, and grainstone are present, as well as subrounded lithic and quartzite clasts. Significant facies changes occur along strike, with massive diamictite with minor laminated beds containing bed-penetrating lonestones at Kheseen Gol (Macdonald and Jones, 2011) stratigraphically equivalent to sedimentary breccia with sub-angular carbonate clasts approaching 1.5 m in diameter <4 km south at Khirvesteg Gol (fig. 3). These massive, ungraded, clast-supported dolomite breccias consist of angular to subangular dolomite clasts up to 30 cm across both above (0-3 m thickness) and below (0-25 m thickness) the Shar Fm diamictite. The matrix of these breccias is micritic and similar to the composition of the clast material, with rare occurrences of terrigenous grains and coarser void-filling grainstone. The Shar diamictite and associated dolomite breccias vary in thickness across the basin from <0.5 m in the central Khoridol Saridag Range to nearly 70 m on the ridge above Ongolog Gol. The base of the Shar Fm is identified by the carbonate breccias and diamictites that occur above an erosional surface that cuts into the upper two members of the Bakh Fm, with Shar Fm diamictite directly overlying Khurts Mb strata in the easternmost Khoridol Saridag Range (figs. 3,4).

*Shar Formation interpretation*. – The Shar diamictite is interpreted to be a glaciogenic deposit correlated with the Marinoan Snowball Earth glaciation (Macdonald and Jones, 2011). The clast and matrix composition of the diamictite suggests that glacial erosion sampled material from the underlying Bakh Fm, with minimal input from siliciclastic or basement sources. The dominance of massive, matrix-supported diamictite suggests deposition in a marine peri-glacial environment at or near the ice grounding line. However, the presence of laminated intervals with bed-penetrating lonestones within massive diamictite-dominated intervals (Macdonald and Jones, 2011) suggests movement of the grounding line, with lonestone-bearing strata putatively associated with episodes of grounding-line retreat and a shift towards distal, suspension-dominated sedimentation punctuated by input from ice-rafted debris (Domack and Hoffman, 2011).

Clast-supported breccias are interpreted to be locally sourced, short transport distance breccias that formed as the result of local glacio-isostatic deformation across the carbonate ramp. The erosional surface observed at the Salkhitai Mb-Shar Fm contact in the eastern Khoridol Saridag Range may have formed following a regression at the onset of the Marinoan glaciation, with the overlying diamictite and carbonate breccia variably recording glacial advance and retreat across the basin.

*Khirvesteg Formation description*. – The basal Khirvesteg Fm includes a ~1-3 m cream-colored dolomite grainstone that overlies the Shar Fm, and hosts twinned barite pseudomorphs (fig. 4C) and bedding-parallel sheet-crack cements (fig. 4D). This interval is overlain by a sequence of lutite in the eastern Khoridol Saridag Range, and by thinly-bedded lime- and dolo-micrite in the central Khoridol Saridag Range and Darkhat Valley. These strata are truncated by an unconformity, which outcrops as an identifiable erosional disconformity at many of the easternmost Khoridol Saridag Range exposures, and ubiquitously as a sharp paraconformable transition from lutite or dolomitized laminated grainstones of the uppermost Khirvesteg Fm to the overlying allodapic phosphatic and siliceous grainstones of the basal Kheseen Fm.

*Khirvesteg Formation interpretation*. – The dolomite grainstone at the base of the Khirvesteg Fm is interpreted to be a basal Ediacaran cap carbonate sequence: in addition to its proximity with the underlying Shar diamictite, the dolomite bed displays features, including sheet-crack cements and crystalline barite, that have been observed in other Marinoan cap carbonate sequences from around the globe (Hoffman et al., 2011). The fine-grained carbonate and siliciclastic sequences that overly the cap dolomite likely reflect a post-Marinoan transgression, with facies across the basin indicating a shift towards suspension-dominated deposition in an outer-ramp to bathyal setting. Mirroring trends observed in the Bakh Fm, the relative abundance of siliciclastic material in lutite in the eastern Khoridol Saridag Range compared to thinly-laminated micrite in the west is consistent with a west-facing margin and deepening to the west in both the Bakh and Khirvesteg Formations.

*Kheseen Formation description*.–The Kheseen Fm displays dramatic lithofacies and thickness variability both within outcrop and across the basin, with total thicknesses ranging from 160-170 m in sections in the eastern Khoridol Saridag Range to over 500 m in the central and southern Khoridol Saridag Range and at Eg Gol (fig. 1B). In the eastern Khoridol Saridag Range, the basal Kheseen Fm disconformably overlies the Khirvesteg Fm above an erosional surface and is composed of interbedded black micritic limestone and dolomite mudstone, organic-rich lutite and shale, and phosphatic and silicified hardgrounds and allodapic carbonate (fig. 5B). Hardgrounds are laterally continuous for only a few meters and are typically in close proximity to cm-scale channels that truncate primary bedding features (fig. 5B), cross-stratified channel fill, and allodapic carbonate packages consisting of edgewise breccia, granular packstone, and grainstone (fig. 5D). Grainstone beds include phosphatic and siliceous grains and clasts. The best-preserved examples of Doushantuo-Pertatataka-type fossils are preserved in this lithofacies, in which individual fossils appear as allochems in packstone and grainstone beds (Anderson et al., 2017, 2019). Up-section, stacked 30 cm-thick beds of nodular black chert, in packages up to 5 m thick, interrupt the hardground/allodapic carbonate sequence. The cherts are superseded by fetid, carbonate-rich shale and thinly bedded lutite with interbedded dolomite grainstone and intraclast conglomerate. Up-section, phosphatic material is found primarily as allochems in graded wackestone and grainstone beds. Chert and phosphorite allochems within limestone wackestone and grainstone beds decrease in abundance up-section, where micrite with black chert nodules, and laminar grey chert beds become dominant towards the top of the formation. Sharp, uneven boundaries are often observed between carbonate and chert horizons.

In the western Khoridol Saridag Range, Darkhat Valley, and Eg Gol localities, evidence of primary authigenic phosphatic and siliceous deposition is less abundant. Instead, fining-upward packages of grainstone, packstone, and wackestone with phosphatic and siliceous allochems dominate and are infrequently punctuated by fetid limestone packstone and wackestone beds containing domal stromatolites and thrombolitic reefs (fig. 5C). These limestone sequences are superseded by a dolomite interval consisting of laminated micrite, domal stromatolites, and oomicritic wackestone and grainstone. In these localities, a 1–6 m-thick bed of black to maroon-red chert is often found at the top of the Kheseen Fm. The chert bed is largely textureless, and sharply bounded, both above and below, by dolomite wackestone or grainstone.

At Kheseen Gol in the eastern Khoridol Saridag Range, the reworked allodapic carbonates of the uppermost Kheseen Fm are interspersed with siliciclastic deposits: the top of the Kheseen Fm is marked by an influx of siliciclastic material, including a 10-12m thick, cobble-to-boulder clast, matrix-supported conglomerate with an erosive base (fig. 5E).

*Kheseen Formation interpretation*. – In the eastern Khoridol Saridag Range, phosphogenesis in the lower Kheseen Fm occurred in a shallow, energetic depositional environment. The co-location of discontinuous, truncated primary bedding surfaces including phosphatic and siliceous hardgrounds, abundant channelization, and cross-stratified allodapic carbonates with angular clasts of phosphatic and siliceous material is consistent with deposition on a shallow carbonate upper ramp or banktop environment subject to tidal currents. Allodapic carbonates contain evidence of local reworking of primary phosphatic and siliceous material, the primary precipitation of which appears to have been concentrated in the easternmost Khoridol Saridag Range. Up-section, phosphatic grainstone and wackestone beds are reworked, consistent with redeposition as mass-wasting deposits in a mid-ramp setting.

In the western Khoridol Saridag Range and Darkhat Valley, Kheseen Fm deposition occurred in a mid- to upper-ramp environment. In these localities, phosphatic material was redeposited as phosphatic and carbonate allochems. Normal grading in the allodapic carbonates with horizons of stromatolites and thrombolites suggests deposition below fair-weather-wave base, but well within the photic zone.

A transition to micrite and bedded chert in the upper Kheseen Fm marks a shift from coarser, gravity flow-dominated deposition to suspension-dominated deposition and continued deepening to a more quiescent basinal environment. Sharp, uneven contacts between chert and micrite beds can be attributed to rheological differences between lithologies, dewatering, and soft-sediment deformation. Together with the geochronological data and carbon isotope data described below, the cobble-to-boulder clast, matrix-supported conglomerate at the top of the Kheseen Fm is interpreted as a debrite (fig. 5E), marking a significant unconformity and major tectonic disturbance to the margin.

*Erkhelnuur Formation*. – The Erkhelnuur Fm is a ~2 km-thick carbonate sequence with Middle Cambrian ichnofossils, archaeocyatha, and trilobites (Korobov et al., 1989). It is separated into three distinct Members (Lower, Middle and Upper) that can be differentiated both litho- and chemo-stratigraphically.

*Lower Member description*. – The Lower Mb of the Erkhelnuur Fm is distinguished by repetitive parasequences above the lime-micrite, cherts, and conglomerate of the uppermost

Kheseen Fm. These parasequences occur as packages of thick dolomite and partially-dolomitized lime-micrite and grainstone-wackestone interbeds, white laminated dolo-micrite and wackestones containing domal or digitate stromatolites (fig. 5F), and allodapic packstone and grainstone beds containing ooids, carbonate clasts, and minor black chert clasts. Throughout the Lower Mb, infrequent and recessive tan-to-green silicified fine-grained lutites stand out as bursts of color in an otherwise blue-gray to white expanse of carbonate. The thickness of the Lower Mb is 250–300 m.

*Middle Member description*. – A transition to limestone-dominated grainstone deposition marks the base of the Middle Mb of the Erkhelnuur Fm. This transition is visible both in the field and on satellite imagery, where the light grey and white dolomites of the Lower Mb give-way to dark blue-grey beds that stand out on ridgetop exposures. Like the Lower Mb, dolo-rhythmites and stromatolite-bearing mudstone beds are bounded by wackestone and grainstone beds in shallowing-upward parasequences. Approximately 20–50 m above the base of the Middle Mb, bed-penetrating bioturbation is more pervasive in micrite and wackestone beds. Irregular tubes, typically 1-2 cm in diameter, increase in frequency and density up-section, eventually obliterating nearly all primary bedding features. Although bioturbation rarely affects the most finely laminated beds, most grainstone beds in the upper Middle Mb are thoroughly perforated with burrows. In the most heavily bioturbated zones, burrows (fig. 5G) tend to focus on individual 5-6 cm bedding-parallel layers, with rare vertical burrows penetrating 3-6 cm interstitial layers that are more sparsely bioturbated. The total thickness of the middle Mb is ~800 m in the Khoridol Saridag Range, and at least 600 m in the Darkhat Valley.

Archaeocyatha occur ~300 m into the Middle Mb, with the best-preserved fossils occurring in zones with minimal bioturbation (fig. 5H). Disassociated, randomly oriented archaeocyathid fossils are present in grainstone beds in the western Arcai Gol drainage, and along the ridgeline between Khirvesteg and Ongolog Gol.

*Upper Member description*. – The base of the Upper Mb of the Erkhelnuur Fm is demarcated by a ≥50 m interval of white dolomite grainstone and wackestone beds. Primary bedding features are obfuscated by dolomitization, but relict 10-60 cm bedding is locally apparent. Like the dark base of the Middle Mb, these white bands are visible and traceable both on distant ridge exposures and on aerial and satellite imagery, which aids the mapping of large-scale structures.

Above the white dolomite sequence, micritic laminites and dolo-grainstones form 1-10 m scale coarsening-upward parasequences for up to 500 m. Ichnofossils are frequent and tend to be concentrated in thicker grainstone beds. Where visible in less-bioturbated strata, the Upper Mb contains cross-bedded and channelized grainstone, microbial mat textures, and ripple cross-stratification. At the top of the sequence, lithic grains and fragments are present in coarse-grained, non-bioturbated grainstone beds, becoming more frequent toward the top of the sequence. Thicker sections of the Upper Mb contain more abundant siliciclastic grains, which occur in graded beds that increase in abundance up-section.

*Erkhelnuur Formation interpretation*. – Repeated, shallowing-upward parasequences of the Lower and Middle Mbs of the Erkhelnuur Fm suggest shoaling in an upper-mid-ramp environment. Interbedded micrite and grainstone beds record repeated gravity flow deposits. The association of domal and digitate stromatolites with thinly-laminated micrite and grainstone beds suggests growth of microbial communities during periods of minimal gravity-flow input. Coarser grainstone and wackestone beds at the top of each parasequence contain allochems, including ooids, likely sourced from an upper ramp setting, and suggest progressive shallowing and increased communication with banktop or inner-ramp depozones at the top of each parasequence. Sparse evidence for tidal or persistent wave action suggests that the Lower and Middle Mbs largely remained below fair-weather-wave base, but within the photic zone, during deposition.

In the Middle Mb, the onset of bed-penetrating bioturbation is broadly associated with an increase in the dominance of wackestone and grainstone. However, in these heavily bioturbated facies, primary depositional fabrics and textures have been destroyed and coarsely recrystallized, potentially causing observational bias towards the apparent dominance of more-energetic carbonate lithofacies. Nonetheless, the appearance of coarser-grained allochems, including archaeocyathid hash, in the Middle Mb indicates increased sediment flux from shallow-water environments, and corroborates an inferred shallowing of the depozone through the Middle Mb.

A transgressive sequence at the base of the Upper Mb is marked by an abrupt shift to ichnofossil-free, well-bedded grainstone. The resumption of shallowing-upward parasequences above this interval also marks the return of abundant ichnofossils, suggesting a return to a similar upper-ramp environment as is inferred for the Middle and Lower Mbs. As with the Lower and Middle Mbs, limited textural evidence for ripple cross-stratification, channelization, and microbial-mat-like textures suggests that the Upper Mb formed in a middle to upper ramp environment. In the uppermost Upper Mb, ichnofossils are not present immediately below and within gravity flows featuring abundant terrigenous allochems that inundate the top of the formation prior to Ukhaatolgoi Fm deposition.

*Ukhaatolgoi Formation description*.–The Ukhaatolgoi Fm is composed of siliciclastic rocks ranging from tuffaceous siltstone to massive subangular boulder conglomerate. Coarse-grained, immature green arkosic wacke is the dominant lithology, with rare granule-to-pebble lithic clasts, angular quartz and plagioclase grains, and carbonate fragments in a green siltstone matrix (fig. 6A). The contact between the uppermost Erkhelnuur Fm and basal Ukhaatolgoi Fm is rarely exposed but appears to be a gradational conformable contact: grainstone beds of the uppermost Upper Mb of the Erkhelnuur Fm incorporate increasing siliciclastic material up-section before being drowned out by massive arkosic wacke, intermittently punctuated by siltstone and gravel lag deposits. Elsewhere, the lower Ukhaatolgoi Fm includes maroon and green siltstone with minor lags of granule-to-pebble conglomerate. The siltstone is typically overlain by several meters of arkosic, angular grit and gravel, which grade into cobble conglomerate. Up-section, green graywacke is interbedded with siliceous siltstone and mudstone and 10 m packages of massive, polyclastic boulder conglomerate.

*Ukhaatolgoi Formation interpretation*.–The accumulation of a thick package of poorly-sorted, immature sandstone, interspersed with coarser lithofacies, reflects the influx of terrigenous material onto a marine, carbonate ramp environment. Though the Ukhaatolgoi Fm includes siliciclastic facies with a range of grain sizes, the dominantly massive and graded bedding observed across all Ukhaatolgoi lithologies suggests that gravity flows, rather than fluvial or fluvio-deltaic processes, were the dominant depositional mechanism during Ukhaatolgoi deposition. Stacked massive and graded beds within the Ukhaatolgoi Fm likely reflect repetitive failures in the stability of terrigenous material accumulating on the margin of what had previously been a carbonate-dominated platform, resulting in extensive siliciclastic gravity flow deposition.

### *4.2 Structure*

The greater Khuvsgul map area can be subdivided into three structurally-distinguishable map areas (fig. 1C): (i) a fold-thrust belt, largely composed of Khuvsgul Group rocks, that makes up most of the Khoridol-Saridag Range (fig. 3); (ii) a region north of Arcai Gol dominated by Sarkhoi Group outcrop, but including exposures of both Khuvsgul Group strata and pre-Sarkhoi gneissic basement (fig. S2, Supplementary Information); and (iii) the Darkhat Valley, which includes limited exposures of the Khuvsgul Group and Sarkhoi Group within a regional topographic lowland bounded by both Paleozoic thrusts and small-scale Neogene normal faulting (fig. S3, Supplementary Information). All three map areas have experienced Neogene-present extensional deformation and volcanism associated with the generation of the failed Baikal Rift system.

*4.2.1 Structure of the Khoridol Saridag map areas*

In the Khoridol Saridag Range map area, N-S trending, gently S-plunging km-scale anticlinoria are separated by W-dipping thrust faults that divide the eastern range into discrete N-S panels (fig. 3; fig. S1, Supplementary Information). These N-S trending structural elements are hereafter referred to as D1 structures. A second set of km-scale folds, the axes of which trend generally E-W and are hereafter termed D2 structures (fig. S1; fig. 7), cross-cut and deform the D1 fold/thrust panels, and are well-developed in the northern and eastern portions of the Khoridol Saridag Range. Along the northern border of the range, fold axes trend WNW-ESE, following the trace of the Arcai Gol Thrust. This generation of folds is accompanied by axial-parallel, S-dipping thrust faults.

The intersection of D1- and D2-generation folds results in domal structures observed throughout the region. These structures are exemplified within the Arcai Syncline, where a D1 N-S anticlinorium is cross-cut by a D2 E-W anticline, resulting in a domal antiform cored by rocks of the Darkhat Group (fig. 3).

Apart from thrust-proximal outcrops, which typically exhibit fault-plane-parallel planar cleavage ~1–3 m on either side of observed fault surfaces, secondary fabrics are not pervasive across the Khoridol Saridag Range. Some axial planar cleavage is apparent near fold axes, and on the limbs m- to cm-scale parasitic folds are present within well-bedded carbonate strata. Siliciclastic strata carry a weak cleavage that is typically subparallel to the nearest major fault plane orientation. Siliciclastic rocks also appear to mediate the location of many of the major thrusts in the region, with faults propagating along or near the contact between carbonate and siliciclastic strata. Furthermore, thrusts that juxtapose two carbonate panels often include entrained slivers of siliciclastic material (fig. 8A).

Traces of E-dipping thrust faults are axial parallel with D1 folds, and those of S-dipping thrust faults are axial parallel with D2 structures (fig. S1). An additional major fault with a D1-parallel trace dips shallowly to the west along the base of the easternmost Khoridol Saridag Range (fig. 3). Although poorly exposed, metasedimentary rocks that make up the footwall of the thrust have a well-developed, planar to undulating cleavage that is similar in character to that observed on the footwall of the Arcai Gol Thrust to the north (fig. 8B).

The faults described above are crosscut by Ordovician and Permian intrusions, which are subsequently cross-cut by E-W trending, steeply dipping oblique sinistral normal faults with typical lateral offsets of a few hundred meters (fig. 3). This fault set is further cut by east-dipping normal faults capped by Neogene basalts.

*4.2.2 Structure of the northern map region*

In the northern map region (fig. 1C), exposure is generally poor, with heavy vegetation and frost-heave on exposed ridges restricting outcrop mapping opportunities to incised river valleys and high-relief ridgetops. Regionally, strata are folded into N-S trending, km-scale anticlinoria, plunging gently to the south (figs. S1, S2), with zones of parasitic meter-to-decameter-scale z-folds concentrated largely on the western limbs of these anticlinoria. Although granitic intrusions that cross-cut the larger-scale D1 folds are found throughout the broader Khuvsgul area, the northern map region also harbors pre-to-syn-D1-deformational intrusive bodies. In the Xachimi Gol drainage (figs. S1, S2), granodiorite plutons intrude the Sarkhoi Fm. At this locality, both the intrusive rocks and the country rock host meter-scale N-S folds and fold-axial-planar foliation.

Secondary fabrics are generally more apparent in northern map region outcrops than elsewhere in the greater Khuvsgul area, with slaty axial-planar cleavage observed in most outcrops that contain meter-to-decimeter scale folds. Darkhat Group exposures often feature a well-developed asymmetrical crenulation cleavage (fig. 8B). This crenulation cleavage is most apparent in the southernmost portion of the northern map region (fig. 1C; fig. S1), where D2-parallel cleavage cuts bedding in outcrops within D1-parallel folds. Here, the resultant crenulation generally indicates a maximum stress direction for the D2 fabric that trends north-

northeast - south-southwest: cleavage orientations broadly dip to the south-southwest, with lengthening of the south-southwest-dipping cleavage planes indicating top-to-the-north-northeast shear (fig. 8A). Although there are only a few exposures of the fault contact, a majority of the footwall rocks at these outcrops feature a single, south-southwest dipping planar foliation, likely the result of intense fault-proximal deformation resulting in the obliteration of the earlier N-S axial-planar fabrics. Due to its proximity to the E-W trending portion of the Arcai Gol drainage, this fault system is referred to as the Arcai Gol Thrust (fig. S1).

*4.2.3 Structure of the Darkhat Valley map region*

In the Darkhat Valley (fig. 1C), Khuvsgul Group rocks exhibit deformation similar to that observed in the other two map areas, including distinct D1 and D2 folds. D2 folds dominate the scattered outcrops found in the center of the Darkhat Valley, with D1 folds and fabrics predominantly observed along the fault bounded edges of the map region and in the limited outcrops of Darkhat Group rocks in the north Darkhat Valley.

Exposures along the southeast edge of the Darkhat Valley and the westernmost Khoridol Saridag Range preserve sets of tight D1 isoclinal folds and east-vergent chevron folds (fig. 8C). These structures are located directly east of a west-dipping, D1-parallel fault plane bounded by several meters of cataclasite and fault breccia (fig. 8D). This fault is inferred to continue north to the outlet of Arcai Gol, defining the western extent of the Khoridol Saridag Range (fig. 1C).

On the western edge of the Darkhat Valley, D1 folds and fabrics dominate the structural motif, with particularly well-developed cleavage observed near the footwall of a west-dipping, D1 fault that thrusts Tonian metasediments of the Oka Prism (Kuzmichev et al., 2007) atop Khuvsgul Group rocks. This cleavage is largely fault-plane parallel, and in many cases is sub-parallel to bedding, which at many outcrops in the westernmost Darkhat Valley appears to be overturned within an east-vergent drag fold along the footwall of the thrust.

Multiple intrusive bodies, ranging from monzogranites to tonalites, outcrop throughout the Darkhat Valley, cross-cutting the folded Darkhat Group and Khuvsgul Group. Several of these intrusions are inferred to be substantially larger in the subsurface than their current mappable outcrops suggest, as surrounding carbonate outcrops are marbleized, or have developed chaotic brecciation that has destroyed primary depositional fabrics in what is interpreted as the metamorphic aureole of the underlying intrusion.

***4.3 U-Pb Zircon Geochronology***

*4.3.1. Detrital zircon geochronology*

Sixteen samples from throughout the Khuvsgul basin yielded detrital zircon, the ages of which are depicted as normalized probability plots (fig. 9). Samples are compiled by formation, with normalized probability plots representing compilations of four samples from the Sarkhoi Fm, one sample from the Khirvesteg Fm, two samples from the Kheseen Fm, and nine samples from the Ukhaatolgoi Fm (see Supplementary Information, Table S2 for all detrital zircon ages and sample locations). The Sarkhoi Fm compilation reveals a strong peak at ~785 Ma, consistent with magmatic ages for volcanics of the Sarkhoi Fm (Kuzmichev and Larionov, 2011). The single detrital sample from the Khirvesteg Fm contains zircons younger than the peak of Sarkhoi magmatism, yielding a maximum depositional age constraint of 687.54 ± 2.05 Ma (LA-ICPMS, n=3). However, this sample is post-Marinoan, and thus must be younger than 635 Ma (Condon et al., 2005). A detrital sample from the Kheseen Fm (above the primary phosphorite strata) yielded a maximum depositional age of 525.19 ± 1.30 Ma (CA-ID-TIMS, n=4). Notably, these samples do not contain the 760-680 Ma detrital peaks observed in the Khirvesteg sample. Finally, the Ukhaatolgoi Fm compilation includes peaks at ~780 Ma, ~630-640 Ma, and ~600 Ma, with a young peak at ~525 Ma and a maximum depositional age of 508.78 ± 0.20 Ma (CA-ID-TIMS, n=2).

*4.3.2. Magmatic zircon geochronology*

A porphyritic rhyolite (KH01) from the Darkhat Valley yielded eighteen concordant young zircon grains, yielding a weighted mean age of 793.7 ± 2.97 Ma. The large MSWD of these young grains is likely due to differential Pb-loss in several of the analyzed grains; alternatively, the younger population represents a true age and the older zircons can be largely interpreted as xenocrystic. As such, we do not attempt to isolate a statistically-homogenous magmatic zircon population from this sample. A porphyritic rhyodacite (KH03) from the Sarkhoi Group, sampled in Darkhat Valley, yielded a weighted mean LA-ICPMS age of 810.9 ± 10.9 Ma (n=5; fig. 10A). A foliated granodiorite (EAGC1942) from the region north of the Arcai Gol Thrust yielded an LA-ICPMS weighted-mean magmatic age of 498.8 ± 2.2 Ma (n=30). CA-ID-TIMS analyses of the five youngest grains from this sample yielded a 2-grain weighted mean magmatic age of 503.83 ± 0.13 Ma, and a single concordant young grain with an age of 503.22 ± 0.45 Ma (fig. 10B). Other granodiorite samples from the same region (EAGC1943, which is heavily foliated, and EAGC 1944, which exhibits relatively light foliation), yielded LA-ICPMS weighted mean ages of 501.3 ± 3.1 Ma (n=15) and 499.2 ± 1.5 Ma (n=88), respectively. All three samples from the northern map area (EAGC1942, EAGC1943, and EAGC1944) reflect variably-foliated examples of a similar metaluminous granodiorite protolith (dominant mineral phases, in order of decreasing abundance, of quartz, plagioclase feldspar, microcline, and variably-chloritized biotite and hornblende, with accessory undifferentiated iron/titanium oxides, zircon, and apatite). Thin section photomicrographs of portions of these samples are collated in the Supplementary Information (fig. S4).

A phaneritic tonalite (dominant mineral phases, in order of decreasing abundance, of quartz, plagioclase, and biotite, with accessory zircon, apatite, and undifferentiated opaque metal oxides) from the southern Darkhat Valley (EAGC1925) yielded an LA-ICPMS weighted-mean age of 447.9 ± 2.5 Ma (n=16). A porphyritic granodiorite (EAGC1926B, featuring 1-2cm euhedral alkali-felsdspar phenocrysts in a medium grained matrix of quartz, plagioclase, alkali feldspar, partially-chloritized biotite, and minor subhedral hornblende, with accessory zircon and apatite) and a porphyritic felsic dike with mm-scale plagioclase phenocrysts in a fine-grained matrix (EAGC1917) from the Muren Gol/Bayan Zurgh region yielded LA-ICPMS weighted-mean ages of 297.4 ± 0.6 Ma (n=210) and 276.59 ± 0.9 Ma (n=74) respectively (fig. 10C). Thin-section photomicrographs of samples EAGC1925 and EAGC1926B are presented in the Supplementary Information (fig. S4). All magmatic zircon ages are visually summarized in fig. 10 and are compiled and tabulated in the Supplementary Information (Table S3).

### *4.4 Carbon isotope chemostratigraphy*

At the base of the Cryogenian Khurts Mb of the Bakh Fm, $\delta^{13}C$ values reach a nadir of ~ -6‰, before returning to values of ~0-2‰ (fig. 4). The Bumbulug Mb is dominated by a positive $\delta^{13}C$ profile of around ~4‰, briefly dipping toward negative values up-section before a recovery to sustained, highly enriched (>6‰) values in the Salkhitai Mb (fig. 4). In general, chemostratigraphically-correlated Cryogenian strata appear to expand to the WSW, with the thickest sections observed in the proximity of Agariin Gol and Bayan Zurgh (fig. 1B). Above the Shar Diamictite, the basal Khirvesteg Fm hosts a distinctive decrease in $\delta^{13}C$, from 0 to -3‰, before a recovery to positive values (fig. 4). In all sections that contain this isotopic profile, the initial decrease in $\delta^{13}C$ occurs in strata that host sheetcrack cements (fig. 4D).

Condensed phosphorite facies of the Kheseen Fm host scattered $\delta^{13}C$ profiles with a negative excursion to ~-4‰ before a recovery to positive $\delta^{13}C$ values (fig. 6). In the more expanded upper portions of the Kheseen Fm, $\delta^{13}C$ profiles are more directly correlated with global composite curves (fig. 11B), and vary from -2 to +2‰.

A decrease of $\delta^{13}C$ values to ~ -3‰, followed by a recovery to 0‰ is a profile diagnostic of the Lower Mb of the Erkhelnuur Fm (fig. 6). In the Middle Mb, positive values of ~ +2‰ are followed by a decrease to ~ -1.5‰ (fig. 6). These are followed a recovery in the Upper Mb to approximately 0‰ to +2‰, with these values persisting up to the base of the Ukhaatolgoi Fm.

## *5. DISCUSSION*

### *5.1 Structural reconstruction of the Khuvsgul basin*

The stratigraphic thickness of the Khuvsgul Group increases to the southwest, with lithofacies changes indicating deepening in the same direction (figs. 4, 6). Similarly, the relative abundance of terrigenous material in the easternmost exposures of the Kheseen and Erkhelnuur Fms suggest a terrestrial source, or at least a paleotopographic high, to the northeast. We suggest that the northern mapping area, which hosts the thinnest Cambrian strata, represents the most proximal region of the Khuvsgul basin, and sections in the Khoridol Saridag Range, Darkhat Valley, and further southwest represent increasingly distal depositional environments. In this model, the northern mapping area is considered to be an autochthonous marginal component, and the fold-and-thrust architecture of the Khoridol Saridag Range map area is likely an amalgamation of parautochthonous platformal material that was folded and thrust-repeated during Paleozoic collision and accretion. The dominance of the north-south trending D1 structures in the northern mapping region and the northern Darkhat Valley suggests a regional episode of east-west compression. The presence of ductile D1-parallel fabrics observed in granodiorites from the northern mapping region (fig. 7) constrain D1 to ≥503.87 ± 0.11 Ma (CA-ID-TIMS; fig. 10). We suggest that this phase of deformation represents terminal collision and accretion along the western TMT margin and the final stages of a Cordilleran-style retro-arc foreland basin inversion that was also responsible for the earlier flysch deposition of the Ukhaatolgoi Fm (see Sections 5.3.4 and 5.5 for additional discussion).

The west-dipping fault observed along the eastern foot of the Khoridol Saridag Range (fig. 1C, fig. S1) is interpreted as the main fault of the Khoridol Saridag Range thrust system, with subsidiary east-dipping backthrusts propagating off this surface (fig. 3). Repeated backthrusts break the Khoridol Saridag Range into distinct thrust panels, with the last major backthrust bounding the eastern edge of the Darkhat Valley (fig. 1C; fig. 8D). Tight, west-vergent isoclinal folds and chevron folds (fig. 8C) in Khuvsgul Group strata exposed along the southeast edge of the Darkhat Valley reflect this area's position as the footwall of a major E-dipping backthrust.

A second major phase of deformation resulted in the generation of east-west trending D2 structures that cross-cut and deform D1 structures in the Khoridol Saridag Range and the Darkhat Valley, as well as a pervasive D2-parallel cleavage that cross-cuts D1-parallel bedding orientations in the northern mapping area. The propagation of the Arcai Gol Thrust (fig. 1C; fig. S1) along the southern margin of the autocthonous northern mapping area, resulting in the juxtaposition of Khuvsgul Group strata atop older Sarkhoi volcanic rocks, suggests that this area was already structurally above the basal Khoridol Saridag Range thrust sheet prior to the generation of the fault. North-northeast - south-southwest compression generated major D2 structures in the Khoridol Saridag Range, including anticlinal folds that crosscut D1 anticlinoria to form domal structures (fig. 3). This compressional regime also generated widespread crenulation cleavage (fig. 8B) in the southernmost portion of the northern mapping area, with cleavage orientations indicating reverse motion plane-parallel to the orientation of the Arcai Gol Thrust. Because Ordovician intrusions in the Khuvsgul region (including the ca. 448 Ma EAGC1925) do not host any fabrics similar to those created by this event, this compressional stress regime likely occurred in the early Paleozoic. We suggest that the D2 deformation is associated with a late Cambrian to Ordovician collision between the northeastern margin of the TMT and Siberia (Buslov et al., 2002; Kuzmichev, 2015; Domeier, 2018), with collision marked by *ca.* 490 Ma magmatic and metamorphic zircon ages from the Olkhon Terrane to the NE (Donskaya et al., 2017).

### *5.2 A new age model and chemostratigraphic framework for the Khuvsgul Group*

Bulk carbonate $\delta^{13}C$ data from measured sections throughout the Khuvsgul Basin were used, in concert with lithostratigraphic, biostratigraphic, and structural context, to generate a basinal composite chemostratigraphic curve for the Khuvsgul Group (fig. 11A). The resultant composite curve was then correlated to contemporaneous, globally distributed $\delta^{13}C$ curves (fig. 11B) by matching the peaks and nadirs of positive and negative $\delta^{13}C$ excursions from the Khuvsgul composite curve. Additional constraints on these correlations are provided both by maximum depositional ages from detrital zircon samples and biostratigraphic constraints from the first observed appearances of archaeocyatha in the Erkhelnuur Fm (figs. 6, 11A). We adopt the nomenclature of the 2020 Geologic Timescale (Gradstein et al., 2020) and the Cambrian age model of Nelson et al. (2023), but also incorporate the regional Siberian timescale nomenclature for the basal Cambrian in our discussion and figures, as the bulk of previous work in the Khuvsgul region utilizes this framework.

We use $\delta^{13}C$ from carbonate strata as a tool for intra- and inter-basinal correlation, and acknowledge that diagenesis can alter primary carbon isotopic compositions in carbonates (Ahm et al., 2018). This alteration can be driven by a variety of factors, including eustatic variability (Swart and Eberli, 2005) and fluid convection through carbonate platforms (Kohout, 1965). Other potential drivers of variability include changes in the composition or volume of local carbon sources and sinks (Holmden et al., 1998), and changes in the dominant carbonate polymorph present in the depozone (e.g. aragonite vs. calcite, Romanek et al., 1992). However, given that both regional and global forcings, including tectonics, climate, and sea level changes, can influence these drivers, carbonate $\delta^{13}C$ chemostratigraphy can still serve as a valuable correlation tool both within and between basins at a regional or even global scale (Ahm and Husson, 2022).

Additional complexities are inherent in correlating $\delta^{13}C$ records from primary phosphogenic strata: compounded with issues of lateral discontinuity and stratigraphic condensation (Anttila et al, 2023; Föllmi, 1996; Föllmi et al., 2017), remineralization and variable redox conditions associated with phosphogenesis may also drive local $\delta^{13}C$ gradients: phosphogenesis has been shown to occur in environments that promote the authigenic precipitation of carbonate near the sulfate reduction-methanogenic transitional zone (e.g. Cui et al., 2016; 2017), resulting in variable authigenic $\delta^{13}C$ compositions. Though some of the $\delta^{13}C$ values derived from the condensed intervals of the Kheseen Fm likely incorporate an authigenic component, texturally homogenous micritic cements within primary phosphogenic strata were targeted for $\delta^{13}C$ analysis whenever possible in order to minimize potential authigenic contamination.

### *5.3 Chronostratigraphy and Neoproterozoic-Cambrian evolution of the Khuvsgul Group*

We combine our new age model with lithostratigraphic and facies observations summarized above to develop a model for the Neoproterozoic-Cambrian evolution of the Khuvsgul basin. A representative tectonic subsidence curve was calculated using a modified version of the backstripping model of Müller et al. (2018); all input data and assumed lithological characteristics are summarized in the Appendix, and tabulated in the Supplementary Information (Table S4). The model tectonic subsidence curve and a cartoon summarizing the tectonic evolution of the Khuvsgul basin(s) are shown in figure 12.

*5.3.1 Cryogenian rift-drift transition:* Following the emplacement of volcanic rocks associated with the Sarkhoi/Zavkhan arc in the Tonian and termination of arc magmatism on the margin, rifting accommodated the deposition of the uppermost Sarkhoi and Arasan siliciclastic sequences. The variable thicknesses and facies of these units can be attributed to rift-related paleotopographic variability across the basin. The development of riftogenic, localized accommodation space continued through deposition of the syn-Sturtian Ongolog Fm, followed by a mid-Cryogenian rift-drift transition to passive-margin deposition. The passive margin persisted through the early Ediacaran (fig. 12A), as evidenced by a shift towards more gradational changes in formational thickness across the basin in the Bakh Fm and overlying Khirvesteg Fm. The development of a passive margin on the western margin of the TMT is corroborated by a lack of Cryogenian and Ediacaran magmatism, and the apparent exponential decay of tectonic subsidence (fig. 12).

*5.3.2 Ediacaran hiatus:* A basinally-ubiquitous unconformity surface above basal Ediacaran strata (figs. 6, 11A) across the Khuvsgul region is potentially related to accretion on the eastern margin of the TMT. An inferred collision is supported by ca. 630-620 Ma peaks in detrital zircon age data from the Dzhida and Hamardavaa regions (Shkol'nik et al., 2016; terrane locations shown in fig. 1), which also occur in detrital zircon spectra from younger Khuvsgul Group rocks in the Khoridol Saridag Range (fig. 9). A similar hiatal surface is observed between the Shuurgat and Zuune Arts Fms. of the Tsagaan Oloom Group (Bold et al., 2016a, Smith et al., 2016), and is potentially related to accretion of the Bayankhongor ophiolite to the east.

*5.3.3 A Cambrian phosphogenic pro-foreland basin:* Above the Ediacaran unconformity surface, phosphatic strata of the basal Kheseen Fm were deposited into a nascent foreland basin associated with collision of the Agardag Arc above a west-dipping subduction zone along the western margin of the TMT (fig. 12B). In the developing pro-foreland, localized zones of primary phosphogenesis experienced uplift and reworking, which we attribute to forebulge migration. Specifically, condensed primary phosphogenic zones on a paleotopographic high centered in the easternmost Khoridol Saridag Range likely sourced phosphatic and siliceous allochems that were redeposited in allodapic grainstones to the south and west (figs. 6,13).The up-section decrease in phosphatic allochem frequency in the Kheseen Fm, as well as an overall trend towards deeper facies associations, suggests the onset of rapid subsidence associated with a developing foredeep, before an abrupt transition to coarse clastic debrites observed in section EAGC1905 at Kheseen Gol (figs. 3, 5E, 6), and massive chert horizons elsewhere in the basin. We suggest that the Kheseen Gol debrites are a wildflysch associated with the inversion of the Kheseen pro-foreland during the terminal collision of the Agardag arc (fig. 12C, D). As such, the debrites, which have a maximum depositional age of 525.19 ± 1.30 Ma (fig. 9), are potentially associated with a significant depositional hiatus or erosional unconformity and may be temporally isolated from the underlying Kheseen Fm phosphorites.

Comparison of $\delta^{13}C$ data from the lower interval of the Kheseen Fm (fig. 11A) with compiled global $\delta^{13}C$ records (fig. 11B) provides an end-member age model for the Kheseen Fm. This model assumes significant depositional hiatus or erosional unconformity between the upper Kheseen Fm phosphatic carbonates and the Kheseen Gol debrites and draws an equivalency between a decrease in median $\delta^{13}C$ values in the basal Kheseen Fm, from approximately +3‰ to -4‰, with a similar decrease following Excursion 1p into the basal Cambrian carbon isotope excursion (BACE; fig. 11B). The Kheseen phosphorites are broadly temporally equivalent to phosphatic strata of the Zuun-Arts Fm and BG2 Mb of the Bayan Gol Fm of the Zavkhan Terrane (Smith et al., 2016; fig. 11C), and, considering radioisotopic constraints that have been proposed for the base of the Cambrian on other paleocontinents (Nelson et al., 2023), have a maximum age of ~534 Ma. This correlation (fig. 11A-B) suggests that phosphogenesis in the Khuvsgul basin lasted ~3 Myr, which is comparable to the longevity of other phosphogenic environments in tectonically active Phanerozoic basins (e.g. Anttila et al., 2023).

The presence of flysch deposits in the upper Kheseen Fm suggests a tectonic reorganization of the Khuvsgul basin associated with a collision. Uplift associated with slab breakoff and subduction polarity reversal could have resulted in significant hiatus or erosion and driven the emplacement of terrigenous debrites across the terminal pro-foreland, prior to the resumption of subsidence in Erkhelnuur Fm time. Though these terrigenous debrites have thus far been described only at Kheseen Gol, *Cloudina*-bearing conglomerates and breccias of the Boxon Group (Khuvsgul-Group-equivalent strata of southern Siberia; Kheraskova and Samygin, 1992) suggest the widespread occurrence of coarse debrites in the early Cambrian.

*5.3.4 Cambrian retro-arc foreland:* The Erkhelnuur Fm was deposited into a rapidly subsiding retroarc foreland basin associated with east-dipping subduction along the western margin of the TMT (fig. 12E), with carbonate platformal growth largely keeping pace with subsidence. Shelf-slope transitional facies persist throughout the upper Erkhelnuur Fm (fig. 6), with little evidence to suggest a long-term flooding stage or drowning of the platform anywhere in the Erkhelnuur stratigraphy. The interpretation of this basin as a retroarc foreland environment is supported by the influx of clastic sediments of the Ukhaatolgoi Fm, which feature facies characteristics of flysch deposition. Detrital zircon spectra from Ukhaatolgoi Fm samples contain Ediacaran and Cambrian grains from an exotic source, presumably the uplifted Agardag arc. In the Khuvsgul region, terminal foreland sedimentation was accompanied by the emplacement and deformation of 504-503 Ma granodiorites, further supporting the interpretation of a retro-arc foreland environment (fig. 7,10), and potentially indicating the collision of another arc/terrane (likely the Gorny Altai Terrane; Dobretsov et al., 2003; Buslov et al., 2013; Bold 2016b) along the western margin of the Ikh-Mongol arc.

### *5.4 Coevolution of the Khuvsgul Group and Neoproterozoic-Cambrian strata of the Zavkhan Terrane*

With ties between the Neoproterozoic-Cambrian stratigraphy of the Zavkhan Terrane and the Khuvsgul Group proposed on the basis of lithostratigraphy (Macdonald and Jones, 2011), a new composite chemostratigraphy from the Khuvsgul Group allows us to refine these earlier correlations. The Cryogenian Bakh Fm hosts a carbon isotope profile similar to those from other Cryogenian non-glacial interlude platformal carbonate sequences around the world (fig. 11). In particular, $\delta^{13}C$ values of +4 to +6‰ in the Khurts Mb of the Bakh Fm are followed by a -3 to -8‰ interval in the Bumbulug Mb, with a recovery to positive (+6 to +8‰) values observed in the upper Bumbulug and basal Salkhitai Mbs. These trends can be directly correlated (fig. 11) to similar patterns observed in the Taishir Fm of the Tsagaan Oloom Group of the Zavkhan Terrane, the type locality of the eponymous negative $\delta^{13}C$ excursion (Macdonald et al., 2009; Johnston et al., 2012; Bold et al., 2016a). This correlation supports the Sturtian and Marinoan affinities of the Ongolog and Shar Fms, respectively, and further bolsters arguments for a unified Khuvsgul and Zavkhan passive margin history during the Cryogenian. In addition to similarities in chemostratigraphy, the Bakh Fm is broadly similar, in terms of thickness, lithology, and facies association, to temporally equivalent intervals of the Taishir Fm (Bold et el., 2016a). Barite crystal fans, sheet-crack cements, and affinities with underlying Marinoan diamictite sequences underscore the identification of the basal Khirvesteg and Ol Fms (Bold et al., 2016a) as Marinoan cap carbonate sequences within the Khuvsgul and Tsagaan Oloom Groups, respectively. Carbon isotope stratigraphy suggests a similar interpretation, with the basal portions of both formations hosting similar $\delta^{13}C$ profiles that dip to as low as -5‰ before recovering to ~ 0‰, a trend observed within Marinoan cap carbonates around the world (Bold et al., 2016a: fig. 17, and references therein). Above the Marinoan cap carbonate sequence, on both terranes, early Ediacaran strata are truncated by an Ediacaran unconformity (Bold et al., 2016a; Macdonald et al., 2009).

Above the Ediacaran hiatal surface, the timing of deposition and lithological similarities between terranes begin to diverge. On the Zavkhan Terrane, the Zuun-Arts, Bayangol, Salaagol, and Khairkhan Fms formed during the latest Ediacaran to early Stage 2 of the Cambrian (~534-520 Ma), and comprise more siliciclastic-rich strata (Smith et al., 2016). On the TMT, Khuvsgul Group strata are carbonate-dominated, and only the Kheseen Fm appears to have been deposited prior to Cambrian Stage 2, with the Erkhelnuur, and Ukhaatolgoi Fms deposited from Cambrian Stage 2 through Stage 3. These stratigraphic differences can be attributed to the development of composite foreland basins during arc-continent collision, slab reversal, and accretion along the western TMT-Zavkhan margin.

### *5.5 Diachronous collision of a Cambrian arc and development of stacked forelands*

Arc volcanism occurred west of both the TMT and the Zavkhan Terranes in the Ediacaran to Cambrian. In the south, the western margin of the Zavkhan Terrane is flanked by the Khantaishir Ophiolite, which formed ca. 570 Ma in a suprasubduction environment (Gianola et al., 2017; 2019), and arc-related igneous rocks. These include the Khantaishir Magmatic Complex, which hosts continental arc lithologies that span ~524-495 Ma (Janoušek et al. 2018). In the north, the ~570 Ma Agardag Tes-Chem ophiolite (Pfänder and Kröner, 2004) lies west of the TMT, albeit inboard of island arc-related intrusive rocks as young as 535 Ma (Rudnev et al., 2006) and ca. 522-518 Ma calc-alkaline granites of the East Tannu-Ola batholith (Rudnev et al., 2008; Mongush et al., 2011).

Janoušek et al. (2018) argued that the Khantaishir Arc, Agardag Arc, and various other early Cambrian arc rocks located west of the TMT-Zavkhan margin were part of a single arc complex, which is termed the Ikh-Mongol Arc. In contrast, Smith et al. (2016) and Bold et al. (2016b) proposed ca. 540-520 Ma arc-continent collision along the composite TMT-Zavkhan margin, followed by slab breakoff and reversal. In schematic models of the Ikh-Mongol Arc, including those found within detailed studies of its components, the arc system is typically depicted as a continental or peri-continental arc over an east-dipping subduction zone (e.g. fig. 19 of Janoušek et al., 2018). However, most of the same studies (Janoušek et al., 2018; Gianola et al., 2017, 2019) note geochemical signatures, particularly in older rocks, that describe an island-arc affinity, while the youngest rocks in the same localities are more closely associated with continental arc compositions. Furthermore, the geometric relationship between the arc rocks of the Khantaishir Arc and the suprasubduction-origin interpretation of the Khantaishir ophiolite is inconsistent with east-dipping subduction at the time of ophiolite formation.

Here, parallel to interpretations of Khantaishir Arc subduction polarity suggested by Smith et al. (2016) and Bold et al. (2016b), we propose that the Ikh-Mongol Arc initiated over a west-dipping subduction zone, resulting in the emplacement of suprasubduction ophiolites oriented east of the main locus of arc volcanism. As the oceanic crust between the arc and the TMT-Zavkhan margin was consumed, the eastward progradation of the pro-foreland onto TMT-Zavkhan marginal crust resulted in the deposition of the Tsagaan-Oloom Group and the Kheseen Fm of the Khuvsgul Group. As the composite Agardag-Khantaishir arc continued to approach and eventually collide with TMT-Zavkhan continental crust, suprasubduction-zone ophiolites were obducted and sandwiched between the arc and TMT-Zavkhan margin, with regional uplift along the margin resulting in the deposition of the Khairkhan Fm on the Zavkhan Terrane, and wildflysch deposits, erosion, and/or depostional hiatus in the upper Kheseen Fm on the TMT. Slab breakoff and reversal along the TMT-Zavkhan margin preceded the deposition of the Erkhelnuur and Ukhaatolgoi formations behind the ~522-518 Ma East Tannu-Ola batholith. Such a scenario is directly analogous to the present-day Taiwan margin (e.g. Teng et al., 2000; Clift et al., 2003).

Ikh-Mongol Arc accretion culminated with regional deformation, potentially associated with collision of the Gorny Altai Terrane (Dobretsov et al., 2003; Buslov et al., 2013; Bold 2016b) along the continental arc's western margin, which manifested as D1 structures in the Khuvsgul Region and the eastward migration of magmatism. Granulite metamorphism in the Sangilen region, which lies between the Agardag Arc and the TMT, occurred c.a. 515 Ma (Karmysheva et al., 2021), with lower temperature regional metamorphism occurring between 505 and 495 Ma (Kozakov et al., 2021). This inferred accretionary orogeny is contemporaneous with the emplacement and subsequent deformation of foliated ~504 Ma granodiorites in the autocthonous portion of the Khuvsgul basin (fig. 7, 10). In the south, rocks in the Khantaishir Magmatic Complex began to host geochemical signatures consistent with a primitive continental arc after ~520 Ma (Janoušek et al., 2018), while magmatism on the Zavkhan Terrane occurred between 509 and 507 Ma (Bold et al., 2016b).

Together, these data outline the diachronous development of composite foreland basins along the TMT-Zavkhan margin. The nascent stages of Ikh-Mongol Arc collision resulted in the deposition of the Zuun-Arts, Bayangol, Salaagol, and Khairkhan Fms of the Zavkhan Terrane and the Kheseen Fm of the Khuvsgul Group into pro-foreland basins between ~534 and ~524 Ma, with the latter strata experiencing a potentially significant depositional hiatus or erosional unconformity (fig. 11A) contemporaneous with continued deposition along the Zavkhan pro-foreland. Following slab reversal and reversal of subduction polarity, ~524-495 Ma foreland deposition on the Khuvsgul terrane occurred in a retroarc foreland basin setting.

### *5.6 Pro-foreland phosphogenesis*

Differences in the style and tempo of foreland development (Sinclair and Naylor, 2012) along the TMT-Zavkhan margin likely had significant impacts on the style and extent of phosphogenesis at each locality. Siliciclastic material is much more abundant in Cambrian strata of the Zavkhan Terrane (Smith et al., 2016) than those of the TMT (fig. 11C), and the relative proximity to (or availability of) terrigenous material in each locality resulted in different grades and styles of phosphate mineralization. Phosphatic intervals in the Zuun-Arts Fm and BG2 Mb of the Bayangol Fm include phosphatic shales, rare phosphatic hardgrounds in carbonate strata, and lags of phosphatized small shelly fossils in carbonate grainstones (Smith et al., 2016). In general, the Zuun-Arts/BG2 phosphorite hosts lower phosphorus concentrations than the Kheseen phosphorites: on the Zavkhan Terrane, phosphogenesis manifested as diffuse phosphatic material in shale, or as concentrated but isolated phosphate precipitation around biogenous material.

In contrast, primary phosphogenesis in the Kheseen Fm (fig. 13) is characterized by localized precipitation of concentrated phosphatic hardgrounds (fig. 13D, E). Although phosphatized microfossils and phosphatic allochems with biogenic textures (Anderson et al., 2017; 2019) have been identified in phosphatic grainstone beds (fig. 13B) of the Kheseen Fm, hardground-bearing zones in the basal Kheseen Fm lack abundant textural evidence of preexistent biological structures or substrates that would promote calcium fluorapatite (CFA) nucleation through direct biological mediation. Many of the phosphatic hardgrounds of the Kheseen Fm are found in close association with channelization, cross-stratification (fig. 13C) and winnowed beds (fig. 13C-E), the cooccurrence of which is indicative of an energetic, sediment-starved environment. Importantly, many of the phosphatic horizons that initially appear to be hardgrounds in hand-sample are lags of granular phosphatic allochems that are cemented with a CFA matrix (red arrow, fig. 5B), indicating that multiple generations of phosphate mineralization are present in many of the most concentrated phosphorite horizons. These observations are consistent with phosphogenic models associated with multigenerational winnowing and phosphate concentration (Baturin and Bezrukhov, 1979; Föllmi, 1996; Anttila et al., 2023), as well as models that invoke intermittent sediment starvation and low apparent sedimentation rates as primary drivers of ore-grade phosphate mineralization and concentration (Föllmi et al., 2017).

Beyond providing an avenue for multigenerational phosphogenesis and mechanical concentration, the high-energy, low-sedimentation-rate environment inferred in the primary phosphogenic zones of the Kheseen Fm may also have promoted permeability barriers conducive to the accumulation of elevated porewater phosphate concentrations: multigenerational phosphatic horizons are often bounded by micrite laminae (fig. 13D, E), which may have provided a low porosity/permeability layer that restricted or focused porewater throughflow, as well as encouraged reducing conditions that increased the concentration of labile phosphate sourced from redox-sensitive mineral phases (Sundby et al., 1986). It has been demonstrated that both directional and oscillatory currents can create “armored”, low-porosity horizons in sedimentary environments with silt-sand grainsize distributions (Wu et al., 2018), with coarser-grainsize layers bounded by finer, lower-permeability horizons. An analogous phenomenon occurred in Miocene phosphorites of the Monterey Fm, where silt- and clay-rich layers bound CFA-cemented lags of granule-pebble phosphatic clasts (Anttila et al., 2023). Additionally, the formation of authigenic and diagenetic phosphate minerals along these permeability barriers may function as a positive feedback through the addition of low-porosity, low-permeability material along a given horizon (Föllmi et al., 2005).

### *5.7 Drivers of phosphogenesis and implications for a global Ediacaran-Cambrian phosphogenic event*

Despite differences in phosphorite texture and grade, tectonically mediated paleotopography in both the Khuvsgul and Zavkhan basins provided the necessary depositional conditions to accumulate phosphorus and precipitate/concentrate authigenic phosphate in the sediment column. We suggest that the eastward migration of a forebulge during the development of the Khuvsgul and Zavkhan pro-forelands drove the formation of paleotopographic highs (fig. 13F), which hosted sedimentary conditions ideal for phosphogenesis. In many ways, this scenario is analogous to a model for authigenic Superior-type iron ore generation in foreland basin environments (Hoffman, 1987), in which the migration of foreland topography drives ore-generating conditions in a migrating, foredeep-axis-parallel band along the entire foreland margin. Phosphogenesis occurred in foreland basin environments throughout the latest Neoproterozoic and Phanerozoic, including examples from the Ediacaran (Flicoteaux and Trompette., 1998; Moreira et al., 2021), Permian (Maughan, 1994), and Cretaceous (Föllmi, 1996). Along the TMT-Zavkhan margin, paleotopographic highs harbored energetic depositional environments that record evidence of abundant erosion and reworking (fig. 13A-E), winnowing (fig. 13D), and varying degrees of sediment starvation. These features are commonly observed in other Phanerozoic phosphorites (e.g. Föllmi, 1990; Föllmi et al., 2017; Anttila et al., 2023), and may be a critical component of condensed phosphorite formation: an energetic, winnowing depozone allows for the repetitive restructuring of the redoxocline at the sediment-water interface, which can greatly impact the lability and mineralogical association of phosphorus in the sediment column.

Labile phosphorus can be transferred from the water column to the sediment either with deposited organic material (Redfield, 1958), or as inorganic phosphate bound to metal oxyhydroxide minerals (Shaffer, 1986; Froelich, 1988). Both of these phosphorus shuttles are inherently redox-sensitive: the remineralization of organic matter, achievable through a variety of metabolic pathways, results in the liberation of organically-bound phosphorus as phosphate (e.g. Froelich et al., 1982; Ingall and Van Capellen, 1990; Berner et al., 1993) as phosphate, while inorganic phosphate bound to Fe and Mn oxyhydroxide minerals becomes labile under reducing conditions (Sundby et al., 1986; O'Brien et al., 1990). Biological mediation of redox conditions adjacent to the sediment-water interface may be critical for modulating both phosphate liberation and precipitation: sulfur-metabolizing microbial ecologies have been shown to increase porewater phosphate concentrations and drive apatite precipitation in experimental (Goldhammer et al., 2010; Brock and Schulz-Vogt, 2011), modern (Schulz and Schulz, 2005; Arning et al., 2008), and Phanerozoic (Arning et al., 2009; Berndmeyer et al., 2012; Salama et al., 2015) phosphogenic environments, with geochemical (Sanders et al., 2024) and putative paleontological (Bailey et al., 2007; 2013) evidence suggesting the occurrence of similar processes in Ediacaran-Cambrian phosphorites. Recurrent redoxocline development in microbial communities (e.g. within stromatolites, sensu Sanders and Groztinger, 2021; ) or in the sediment column (through repetitive deposition, hiatus, and reworking/removal in winnowing sedimentary environments) promotes the repeated remobilization of redox-sensitive mineral- and organic-bound phosphate, a fraction of which may precipitate as relatively-insoluble authigenic minerals (Föllmi, 1996, and references therein). These authigenic CFA nodules or lamina are less susceptible to removal during winnowing than fine sediment or organic material, resulting in the relative immobility and eventual reburial of authigenic phosphatic material that can: a) serve as an ideal nucleation substrate for future authigenic precipitation (Van Cappellen et al., 1993), and; b) create low porosity/permeability layers that further concentrate pore-water phosphate (e.g. Föllmi et al., 2005).

In this model, the most critical factors governing phosphogenesis are: i) the prevalence and abundance of shuttling mechanisms (e.g. organic material and/or redox-sensitive minerals) to efficiently transfer phosphate to or across the sediment-water-interface, and; ii) the effectiveness of the local depositional environment in modulating phosphate release, retention, and precipitation in the sediment. We propose that changes associated with these factors, rather than changes in gross marine phosphate abundance, are responsible for the global Ediacaran-Cambrian increase in phosphogenesis. Phosphorus concentrations in marine shales indicate that marine phosphate abundance was elevated to near-Phanerozoic levels by the Tonian (Planavsky et al., 2023), with shallow marine carbonates also recording elevated levels of marine phosphate in the early Neoproterozoic (Roest-Ellis et al., 2023). As such, the relative dearth of Tonian and Cryogenian phosphorites and the apparent Ediacaran-Cambrian increase in phosphogenesis may instead reflect a change that affected the mechanism or locus of authigenic phosphate accumulation.

One such change is the gradual and sustained increase in the oxidative potential in Earth's surface environments (Stockey et al., 2024) following the Cryogenian Snowball Earth events, which were associated with a return of iron formations in the geological record (Cox et al., 2013) and a precipitous decline in the abundance of seawater sulfate (Hurtgen et al., 2002). We suggest that the Ediacaran-Cambrian increase in phosphogenesis reflects the opening of a taphonomic window, during which redox conditions conducive to phosphogenesis expanded into progressively deeper marginal marine settings (e.g. Zhang et al., 2019, and references therein). These depositional environments may be more likely to be preserved in the stratigraphic record relative to the proximal, peritidal depozones that hosted phosphogenesis during periods with lower oxidative potential (Nelson et al., 2010), resulting in an apparent increase in the abundance of phosphorites in the rock record across the Neoproterozoic-Phanerozoic transition. In this scenario, an increase in $pO_2$ increased terrestrial sulfide oxidation and the delivery of sulfate to the oceans (Lyons and Gill, 2010), providing fuel for enhanced sulfate reduction of organic matter (Berner, 1977; Kipp and Stueken, 2017; Cui et al., 2017; Laakso et al., 2020; Dodd et al., 2023), and increasing the potential for phosphate mobilization and shuttling across the sediment-water interface in marginal marine depozones.

Although the establishment of requisite redox potentials in progressively deeper environments set the stage for phosphogenesis to occur within marginal marine settings, the locus, timing, and style of authigenic phosphate accumulation in Ediacaran-Cambrian phosphorites was ultimately determined by local, depozone-dependent sedimentological and putative biologically-mediated conditions. The driving role of these local controls is underscored by the diachroneity of Ediacaran-Cambrian phosphorites across nearly 130 Myr (fig. 14). Despite their dispersion in both time and space, all well-described Ediacaran-Cambrian phosphorites summarized in figure 14 host sedimentological evidence for intermittently-energetic depositional conditions, sedimentary reworking, and localized condensation. As we demonstrate above, and as may have been the case for other Ediacaran-Cambrian foreland basin phosphorites, the phosphogenic environments in the Khuvsgul and Zavkhan basins were directly modulated by local tectonic processes through the generation of topography.

### *5.8 Acanthomorphs of the Kheseen Fm: a long-lived biota*

Microfossils, including Doushantuo-Pertatataka-Type acanthomorphic acritarchs, are found within reworked phosphorites of the Kheseen Fm within the easternmost Khoridol Saridag Range (Anderson et al., 2017; 2019; locations in fig. 3, and stratigraphic position in fig. 11A). Doushantuo-Pertatataka-Type acanthomorphs were a cosmopolitan organism in the Ediacaran (Cohen and Macdonald, 2015) that appeared soon after the terminal Cryogenian (McFadden et al., 2009), and have been hypothesized (Xiao et al., 2014), albeit controversially (Cunningham et al., 2017), to represent early animal embryos. Doushantuo-Pertataka-Type acanthomorphic acritarchs were initially thought to disappear from the fossil record prior to or during the Shuram carbon isotope excursion (Zhou et al., 2017), a globally-synchronous phenomenon that occurred between 574 and 567 Ma (Rooney et al., 2020). However, discoveries of acanthomorphic achritarchs in putatively late-Ediacaran strata (Golubkova et al., 2015; Ouyang et al., 2017; Anderson et al., 2017) refuted this idea, with the occurrence of acanthomorphic acritarchs in late Ediacaran and basal Cambrian (544-530 Ma) strata of the Oppokun Fm of northern Siberia (Grazhdankin et al., 2020) confirming the long-lived nature of these taxa (fig. 14). Our new chronostratigraphic model revises the age of the Kheseen Fm fossil assemblage described by Anderson et al. (2019) to be within the recovery of the BACE and prior to excursion 2p (fig 11A-B), constraining the ages of this interval to between ~533-531 Ma, and making this assemblage one of the youngest known phosphatized Doushantuo-Pertatataka-Type fossil localities in the world (fig. 14). Moreover, this age constraint demonstrates that Doushantuo-

Pertatataka-type assemblages occurred, at localities around the globe, across a span of more than 90 million years.

## 6. CONCLUSIONS

New geological mapping, chemostratigraphy, biostratigraphy, and U-Pb zircon geochronology inform a new age and tectonic model for the Khuvsgul Group. The Khuvsgul Group was deposited into a series of stacked basins that developed along the western margin of the Tuva-Mongolia Terrane. The Cryogenian Ongolog, Bakh, Shar, and basal Ediacaran Khirvesteg Fms were deposited along a passive margin, prior to a prolonged depositional hiatus in the middle and late Ediacaran. Phosphorites of the Kheseen Fm, which host a Doushantuo-Pertatataka-Type microfossil assemblage, were deposited into a nascent pro-foreland basin associated with the Agardag arc ca. 534 and 531 Ma. Wildflysch deposition and several putative exposure surfaces observed around the basin at the top of the Kheseen Fm record slab breakoff, foreland inversion, and a *ca.* 525 Ma reversal in subduction polarity, prior to the deposition of the ~523-518 Ma Erkhelnuur Fm in a retroarc foreland. Collision along the western outboard margin of the Ikh-Mongol arc resulted in uplift and the emplacement of the Ukhaatolgoi Fm flysch, which directly preceded the emplacement of granodiorites on the autocthonous TMT. These folded intrusive rocks constrain the age of north-south trending structures in the Khuvsgul region to *ca.* 504 Ma, while a second set of north-northeast - south-southwest trending structures and fabrics indicates collision of the TMT with southern Siberia prior to 448 Ma.

The new age and tectonic model outlined above strengthens ties between the Khuvsgul Group of the TMT and the Tsagaan Oloom Group of the Zavkhan Terrane, and supports the notion of a shared TMT-Zavkhan margin throughout the Neoproterozoic and Cambrian. The model also demonstrates that phosphogenesis occurred synchronously along this composite margin in the Terreneuvian, albeit with different phosphogenic styles: abundant siliciclastic input resulted in relatively diffuse phosphate mineralization on the Zavkhan Terrane, while sediment starvation and winnowing processes drove the deposition of highly concentrated phosphate deposits in the Kheseen Fm of the Khuvsgul Group. As has been demonstrated for younger Phanerozoic phosphorites, the locus and style of phosphogenesis along the TMT-Zavkhan margin was tectonically modulated, with primary phosphogenesis occurring in shallow, energetic depozones putatively associated with the eastward migration of the forebulge of the Ikh-Mongol

Arc pro-foreland. To this end, we suggest that the increase in Ediacaran-Cambrian phosphogenesis reflects the taphonomy of a redox-dependent depositional process, rather than a shift in global marine phosphate abundance: an increase in marine sulfate concentrations in the wake of the Cryogenian may have allowed microbial sulfate reduction (and redox conditions favorable to phosphogenesis) to expand into marginal marine environments that are likely to be preserved in the rock record.

* * *

## ACKNOWLEDGEMENTS

This work was supported by the National Science Foundation (NSF) Frontier Research in Earth Science (FRES) Grant FRES1925990 and the National Aeronautics and Space Administration (NASA) Massachusets Institute of Technology (MIT) Astrobiology node NASA Geobiology grant NNH10ZDA001N-EXO to F.A. Macdonald. E. Anttila was supported in part by NSF Graduate Research Fellowship (GRFP) 2139319. We thank E. Baiarsaikhan, E. Erdene, Sam LoBianco, Peter Otness, and Judy Pu for assistance, stimulating conversations, and camaraderie in the field, and Uyanga Bold for guidance both scientifically and logistically. We thank M. Munkhbataar and Ariunsanaa Dorj for logistical assistance, and the Ministry of Environment of Mongolia, and rangers and staff of the Khuvsgul Nuur National Park and Khoridol Saaridag Protected Zone for logistal assistance, permits, and access. We thank Galen Halverson and Thi Hao Bui for usage of the stable isotope measurement facilities at McGill University, Ted Present and John Grotzinger for usage of the microXRF at California Institute of Technology, and Andrew Kylander Clark and John Cottle for assistance with LA-ICPMS measurements at UC Santa Barbara. We thank Emmy Smith for helpful discussions, and thank Michael Kipp and an anonymous reviewer for salient comments that directly improved the manuscript. Finally, we dedicate this work to the memory of Batsukh Erdene, one of the most knowledgeable, capable, steadfast, and kind individuals whom we are glad to have known.

* * *

## COMPETING INTEREST STATEMENT

The Authors declare that they have no competing interests.

* * *

## AUTHOR CONTRIBUTIONS

E.S.C. Anttila: *conceptualization, field work, laboratory work/analyses, writing, editing/revision.*

F.A. Macdonald: *funding acquisition, conceptualization, editing/revision, supervision.*

B. Schoene: *editing/revision, supervision.*

S.P. Gaynor: *laboratory work and analyses, editing/revision.*

* * *

## REFERENCES

Ahm, A. S. C., Bjerrum, C. J., Blättler, C. L., Swart, P. K., & Higgins, J. A. (2018). Quantifying early marine diagenesis in shallow-water carbonate sediments. *Geochimica et Cosmochimica Acta*, *236*, 140-159. https://doi.org/10.1016/j.gca.2018.02.042

Ahm, A. S., & Husson, J. (2022). *Local and Global Controls on Carbon Isotope Chemostratigraphy*. Cambridge University Press. https://doi.org/10.1017/9781009028882

Anderson, R. P., Macdonald, F. A., Jones, D. S., McMahon, S., & Briggs, D. E. (2017). Doushantuo-type microfossils from latest Ediacaran phosphorites of northern Mongolia. *Geology*, *45*(12), 1079-1082. https://doi.org/10.1130/G39576.1

Anderson, R. P., McMahon, S., Macdonald, F. A., Jones, D. S., & Briggs, D. E. (2019). Palaeobiology of latest Ediacaran phosphorites from the upper Khesen Formation, Khuvsgul Group, northern Mongolia. *Journal of Systematic Palaeontology*, *17*(6), 501-532. https://doi.org/10.1080/14772019.2018.1443977

Anttila, E. S., Macdonald, F., & Bold, U. (2021). Stratigraphy of the Khuvsgul Group, Mongolia. *Mongolian Geoscientist*, *26*(52), 2-15. https://doi.org/10.5564/mgs.v26i52.1516

Anttila, E. S., Macdonald, F. A., Szymanowski, D., Schoene, B., Kylander-Clark, A., Danhof, C., & Jones, D. S. (2023). Timing and tempo of organic carbon burial in the Monterey Formation of the Santa Barbara Basin and relationships with Miocene climate. *Earth and Planetary Science Letters*, *620*, 118343. https://doi.org/10.1016/j.epsl.2023.118343

Arning, E. T., Birgel, D., Schulz-Vogt, H. N., Holmkvist, L., J∅ rgensen, B. B., Larson, A., & Peckmann, J. (2008). Lipid biomarker patterns of phosphogenic sediments from upwelling regions. *Geomicrobiology Journal*, *25*(2), 69-82. https://doi.org/10.1080/01490450801934854

Arning, E. T., Birgel, D., Brunner, B., & Peckmann, J. (2009). Bacterial formation of phosphatic laminites off Peru. *Geobiology*, *7*(3), 295-307. https://doi.org/10.1111/j.1472-4669.2009.00197.x

Bailey, J. V., Joye, S. B., Kalanetra, K. M., Flood, B. E., & Corsetti, F. A. (2007). Evidence of giant sulphur bacteria in Neoproterozoic phosphorites. *Nature*, *445*(7124), 198-201. doi:10.1038/nature05457

Bailey, J. V., Corsetti, F. A., Greene, S. E., Crosby, C. H., Liu, P., & Orphan, V. J. (2013). Filamentous sulfur bacteria preserved in modern and ancient phosphatic sediments: implications for the role of oxygen and bacteria in phosphogenesis. *Geobiology*, *11*(5), 397-405. https://doi.org/10.1111/gbi.12046

Banerjee, D. M., Basu, P. C., & Srivastava, N. (1980). Petrology, mineralogy, geochemistry, and origin of the Precambrian Aravallian phosphorite deposits of Udaipur and Jhabua, India. *Economic Geology*, *75*(8), 1181-1199. https://doi.org/10.2113/gsecongeo.75.8.1181

Barfod, G. H., Vervoort, J. D., Montanez, I. P., & Riebold, S. (2004, June). Lu-Hf geochronology of phosphates in ancient sediments. In *GEOCHIMICA ET COSMOCHIMICA ACTA* (Vol. 68, No. 11, pp. A336-A336).

Baturin, G. N., & Bezrukov, P. L. (1979). Phosphorites on the sea floor and their origin. *Marine Geology*, *31*(3-4), 317-332. https://doi.org/10.1016/0025-3227(79)90040-9

Berndmeyer, C., Birgel, D., Brunner, B., Wehrmann, L. M., Jöns, N., Bach, W., ... & Peckmann, J. (2012). The influence of bacterial activity on phosphorite formation in the Miocene Monterey Formation, California. *Palaeogeography, Palaeoclimatology, Palaeoecology*, *317*, 171-181. https://doi.org/10.1016/j.palaeo.2012.01.004

Berner, R. A. (1977). Stoichiometric models for nutrient regeneration m anoxic sediments 1. *Limnology and Oceanography*, *22*(5), 781-786. https://doi.org/10.4319/lo.1977.22.5.0781

Berner, R. A., Ruttenberg, K. C., Ingall, E. D., & Rao, J. L. (1993). The nature of phosphorus burial in modern marine sediments. In *Interactions of C, N, P and S biogeochemical cycles and global change* (pp. 365-378). Springer Berlin Heidelberg. https://doi.org/10.1007/978-3-642-76064-8_15

Bertrand-Sarfati, J., Flicoteaux, R., Moussine-Pouchkine, A., & Ait Kaci, A. A. (1997). Lower Cambrian apatitic stromatolites and phospharenites related to the glacio-eustatic cratonic rebound (Sahara, Algeria). *Journal of Sedimentary Research*, *67*(5), 957-974. https://doi.org/10.1306/D426868A-2B26-11D7-8648000102C1865D

Bold, U., Smith, E. F., Rooney, A. D., Bowring, S. A., Buchwaldt, R., Dudás, F. Ő., ... & Macdonald, F. A. (2016a). Neoproterozoic stratigraphy of the Zavkhan terrane of Mongolia: The backbone for Cryogenian and early Ediacaran chemostratigraphic records. *American Journal of Science*, *316*(1), 1-63. https://doi.org/10.2475/01.2016.01

Bold, U., Crowley, J. L., Smith, E. F., Sambuu, O., & Macdonald, F. A. (2016b). Neoproterozoic to early Paleozoic tectonic evolution of the Zavkhan terrane of Mongolia: Implications for continental growth in the Central Asian orogenic belt. *Lithosphere*, *8*(6), 729-750. https://doi.org/10.1130/L549.1

Bold, U., Isozaki, Y., Aoki, S., Sakata, S., Ishikawa, A., Sawaki, Y., & Sawada, H. (2019). Precambrian basement, provenance implication, and tectonic evolution of the Gargan block of the Tuva-Mongolia terranes, Central Asian Orogenic Belt. *Gondwana Research*, *75*, 172-183. https://doi.org/10.1016/j.gr.2019.05.003

Bowring, J. F., McLean, N. M., & Bowring, S. A. (2011). Engineering cyber infrastructure for U-Pb geochronology: Tripoli and U-Pb_Redux. *Geochemistry, Geophysics, Geosystems*, *12*(6). https://doi.org/10.1029/2010GC003479

Bowyer, F. T., Zhuravlev, A. Y., Wood, R., Shields, G. A., Zhou, Y., Curtis, A., ... & Zhu, M. (2022). Calibrating the temporal and spatial dynamics of the Ediacaran-Cambrian radiation of animals. *Earth-Science Reviews*, *225*, 103913. https://doi.org/10.1016/j.earscirev.2021.103913

Brock, J., & Schulz-Vogt, H. N. (2011). Sulfide induces phosphate release from polyphosphate in cultures of a marine Beggiatoa strain. *The ISME journal*, *5*(3), 497-506. https://doi.org/10.1038/ismej.2010.135

Buihover, B.N., Volkov, R. I., Ilyin, A.B., Pushlenkov, U.P., Savin, B.E., Semenova, O.A., Solyanikov, B.P., Spirkin, A.I., Tikhonova, O.K., Tikhonov, B.I., Uflayand, A.K. (1968). Geologic map, Khubsugul Aimag, Mongolia Peoples Republic. List M-47-IC,X,XI. Contract no. 1497 (in Russian).

Burchette, T. P., & Wright, V. P. (1992). Carbonate ramp depositional systems. *Sedimentary geology*, *79*(1-4), 3-57. https://doi.org/10.1016/0037-0738(92)90003-A

Buslov, M. M., Saphonova, I. Y., Watanabe, T., Obut, O. T., Fujiwara, Y., Iwata, K., ... & Kazansky, A. Y. (2001). Evolution of the Paleo-Asian Ocean (Altai-Sayan Region, Central Asia) and collision of possible Gondwana-derived terranes with the southern marginal part of the Siberian continent. *Geosciences Journal*, *5*, 203-224. https://doi.org/10.1007/BF02910304

Buslov, M. M., Watanabe, T., Saphonova, I. Y., Iwata, K., Travin, A., & Akiyama, M. (2002). A Vendian-Cambrian island arc system of the Siberian continent in Gorny Altai (Russia, Central Asia). *Gondwana Research*, *5*(4), 781-800. https://doi.org/10.1016/S1342-937X(05)70913-8

Buslov, M. M., Ryabinin, A. B., Zhimulev, F. I., & Travin, A. V. (2009). Manifestations of the Late Carboniferous and Early Permian stages of formation of nappe-fold structures in the southern framework of the Siberian platform (East Sayany, South Siberia). In *Doklady Earth Sciences* (Vol. 428, No. 1, p. 1105). Springer Nature BV.

Buslov, M. M., Geng, H., Travin, A. V., Otgonbaatar, D., Kulikova, A. V., Ming, C., ... & Trofimova, D. A. (2013). Tectonics and geodynamics of Gorny Altai and adjacent structures of the Altai–Sayan folded area. *Russian Geology and Geophysics*, *54*(10), 1250-1271 https://doi.org/10.1016/j.rgg.2013.09.009

Clift, P. D., Schouten, H., & Draut, A. E. (2003). A general model of arc-continent collision and subduction polarity reversal from Taiwan and the Irish Caledonides. *Geological Society, London, Special Publications*, *219*(1), 81-98. https://doi.org/10.1144/GSL.SP.2003.219.01.04

Cohen, P. A., & Macdonald, F. A. (2015). The Proterozoic record of eukaryotes. *Paleobiology*, *41*(4), 610-632. https://doi.org/10.1017/pab.2015.25

Colman, A. S., & Holland, H. D. (2000). The Global Diagenetic Flux of Phosphorus from Marine Sediments to the Oceans: Redox Sensitivity and the Control of Atmospheric Oxygen Levels. https://doi.org/10.2110/pec.00.66.0053

Condon, D., Zhu, M., Bowring, S., Wang, W., Yang, A., & Jin, Y. (2005). U-Pb ages from the neoproterozoic Doushantuo Formation, China. *science*, *308*(5718), 95-98. DOI: 10.1126/science.1107765

Condon, D. J., Schoene, B., McLean, N. M., Bowring, S. A., & Parrish, R. R. (2015). Metrology and traceability of U–Pb isotope dilution geochronology (EARTHTIME Tracer Calibration Part I). *Geochimica et Cosmochimica Acta*, *164*, 464-480. https://doi.org/10.1016/j.gca.2015.05.026

Cook, P. J., & McElhinny, M. W. (1979). A reevaluation of the spatial and temporal distribution of sedimentary phosphate deposits in the light of plate tectonics. *Economic Geology*, *74*(2), 315-330. https://doi.org/10.2113/gsecongeo.74.2.315

Cook, P.J., and Shergold, J.H. (1986). *Phosphate Deposits of the World: Volume 1.* Cambridge University Press.

Cook, P. J. (1992). Phosphogenesis around the Proterozoic-Phanerozoic transition. *Journal of the Geological Society*, *149*(4), 615-620. https://doi.org/10.1144/gsjgs.149.4.0615

Cox, G. M., Halverson, G. P., Minarik, W. G., Le Heron, D. P., Macdonald, F. A., Bellefroid, E. J., & Strauss, J. V. (2013). Neoproterozoic iron formation: An evaluation of its temporal, environmental and tectonic significance. *Chemical Geology*, *362*, 232-249. https://doi.org/10.1016/j.chemgeo.2013.08.002

Cui, H., Xiao, S., Zhou, C., Peng, Y., Kaufman, A. J., & Plummer, R. E. (2016). Phosphogenesis associated with the Shuram Excursion: Petrographic and geochemical observations from the Ediacaran Doushantuo Formation of South China. *Sedimentary Geology*, *341*, 134-146 https://doi.org/10.1016/j.sedgeo.2016.05.008

Cui, H., Kaufman, A. J., Xiao, S., Zhou, C., & Liu, X. M. (2017). Was the Ediacaran Shuram Excursion a globally synchronized early diagenetic event? Insights from methane-derived authigenic carbonates in the uppermost Doushantuo Formation, South China. *Chemical Geology*, *450*, 59-80. https://doi.org/10.1016/j.chemgeo.2016.12.010

Cunningham, J. A., Vargas, K., Yin, Z., Bengtson, S., & Donoghue, P. C. (2017). The Weng'an Biota (Doushantuo Formation): an Ediacaran window on soft-bodied and multicellular microorganisms. *Journal of the Geological Society*, *174*(5), 793-802. https://doi.org/10.1144/jgs2016-142

Demidenko, Y. E., Zhegallo, E. A., Parkhaev, P. Y., & Shuvalova, Y. V. (2003). Age of phosphorites from the Khubsugul Basin (Mongolia).

Dobretsov, N. L., Buslov, M. M., & Vernikovsky, V. A. (2003). Neoproterozoic to Early Ordovician evolution of the Paleo-Asian Ocean: implications to the break-up of Rodinia. *Gondwana Research*, *6*(2), 143-159. https://doi.org/10.1016/S1342-937X(05)70966-7

Dodd, M. S., Shi, W., Li, C., Zhang, Z., Cheng, M., Gu, H., ... & Lyons, T. W. (2023). Uncovering the Ediacaran phosphorus cycle. *Nature*, 1-7. https://doi.org/10.1038/s41586-023-06077-6

Domack, E. W., & Hoffman, P. F. (2011). An ice grounding-line wedge from the Ghaub glaciation (635 Ma) on the distal foreslope of the Otavi carbonate platform, Namibia, and its bearing on the snowball Earth hypothesis. *Bulletin*, *123*(7-8), 1448-1477. https://doi.org/10.1130/B30217.1

Domeier, M. (2018). Early Paleozoic tectonics of Asia: Towards a full-plate model. *Geoscience Frontiers*, *9*(3), 789-862. https://doi.org/10.1016/j.gsf.2017.11.012

Donov, N. A., Edemsky, H. B. & Ilyin, A. V. (1967). Cambrian phosphorites of Mongolia Popular Republic. *Sovetskaya Geologia*, 3, 55–60

Donskaya, T. V., Gladkochub, D. P., Fedorovsky, V. S., Sklyarov, E. V., Cho, M., Sergeev, S. A., & Kim, J. (2017). Pre-collisional (> 0.5 Ga) complexes of the Olkhon terrane (southern Siberia) as an echo of events in the Central Asian Orogenic Belt. *Gondwana Research*, *42*, 243-263. https://doi.org/10.1016/j.gr.2016.10.016

Flicoteaux, R., & Trompette, R. (1998). Cratonic and foreland Early Cambrian phosphorites of West Africa: Palaeoceanographical and climatical contexts. *Palaeogeography, Palaeoclimatology, Palaeoecology*, *139*(3-4), 107-120. https://doi.org/10.1016/S0031-0182(97)00141-7

Föllmi, K. B. (1990). Condensation and phosphogenesis: example of the Helvetic mid-Cretaceous (northern Tethyan margin). *Geological Society, London, Special Publications*, *52*(1), 237-252. https://doi.org/10.1144/GSL.SP.1990.052.01.17

Föllmi, K. B. (1996). The phosphorus cycle, phosphogenesis and marine phosphate-rich deposits. *Earth-Science Reviews*, *40*(1-2), 55-124. https://doi.org/10.1016/0012-8252(95)00049-6

Föllmi, K. B., Badertscher, C., de Kaenel, E., Stille, P., John, C. M., Adatte, T., & Steinmann, P. (2005). Phosphogenesis and organic-carbon preservation in the Miocene Monterey Formation at Naples Beach, California—The Monterey hypothesis revisited. *Geological Society of America Bulletin*, *117*(5-6), 589-619. https://doi.org/10.1130/B25524.1

Föllmi, K. B., Thomet, P., Lévy, S., KAENEL, E. D., Spangenberg, J. E., Adatte, T., ... & Garrison, R. E. (2017). The impact of hydrodynamics, authigenesis, and basin morphology on sediment accumulation in an upwelling environment: The Miocene Monterey Formation at Shell Beach and Mussel Rock (Pismo and Santa Maria basins, Central California, USA). *Journal of Sedimentary Research*, *87*(9), 986-1018. https://doi.org/10.1130/B32061.1

Froelich, P. N., Bender, M. L., Luedtke, N. A., Heath, G. R., & DeVries, T. (1982). Marine phosphorus cycle. *Am. J. Sci.;(United States)*, *282*(4). https://doi.org/10.2475/ajs.282.4.474

Froelich, P. N. (1988). Kinetic control of dissolved phosphate in natural rivers and estuaries: a primer on the phosphate buffer mechanism 1. *Limnology and oceanography*, *33*(4part2), 649-668. https://doi.org/10.4319/lo.1988.33.4part2.0649

Gerstenberger, H., & Haase, G. (1997). A highly effective emitter substance for mass spectrometric Pb isotope ratio determinations. *Chemical geology*, *136*(3-4), 309-312. https://doi.org/10.1016/S0009-2541(96)00033-2

Gianola, O., Schmidt, M. W., Jagoutz, O., & Sambuu, O. (2017). Incipient boninitic arc crust built on denudated mantle: the Khantaishir ophiolite (western Mongolia). *Contributions to Mineralogy and Petrology*, *172*, 1-18. https://doi.org/10.1007/s00410-017-1415-4

Gianola, O., Schmidt, M. W., Jagoutz, O., Rickli, J., Bruguier, O., & Sambuu, O. (2019). The Crust–Mantle Transition of the Khantaishir Arc Ophiolite (Western Mongolia). *Journal of Petrology*, *60*(4), 673-700. https://doi.org/10.1093/petrology/egz009

Goldhammer, T., Brüchert, V., Ferdelman, T. G., & Zabel, M. (2010). Microbial sequestration of phosphorus in anoxic upwelling sediments. *Nature Geoscience*, *3*(8), 557-561. https://doi.org/10.1038/ngeo913

Golubkova, E. Y., Zaitseva, T. S., Kuznetsov, A. B., Dovzhikova, E. G., & Maslov, A. V. (2015, June). Microfossils and Rb-Sr age of glauconite in the key section of the Upper Proterozoic of the northeastern part of the Russian plate (Keltmen-1 borehole). In *Doklady Earth Sciences* (Vol. 462, pp. 547-551). Pleiades Publishing. https://doi.org/10.1134/S1028334X15060045

Gradstein, F. M., Ogg, J. G., Schmitz, M. D., & Ogg, G. M. (Eds.). (2020). *Geologic time scale 2020*. Elsevier.

Grazhdankin, D., Nagovitsin, K., Golubkova, E., Karlova, G., Kochnev, B., Rogov, V., & Marusin, V. (2020). Doushantuo-Pertatataka–type acanthomorphs and Ediacaran ecosystem stability. *Geology*, *48*(7), 708-712. https://doi.org/10.1130/G47467.1

Grey, K., & Calver, C. R. (2007). Correlating the ediacaran of Australia. *Geological Society, London, Special Publications*, *286*(1), 115-135. https://doi.org/10.1144/SP286.8

Hartmann, J., & Moosdorf, N. (2011). Chemical weathering rates of silicate-dominated lithological classes and associated liberation rates of phosphorus on the Japanese Archipelago—Implications for global scale analysis. *Chemical Geology*, *287*(3-4), 125-157. https://doi.org/10.1016/j.chemgeo.2010.12.004

Hiess, J., Condon, D. J., McLean, N., & Noble, S. R. (2012). 238U/235U systematics in terrestrial uranium-bearing minerals. *Science*, *335*(6076), 1610-1614. https://doi.org/10.1126/science.1215507

Hoffman, P. F. (1987). Early Proterozoic foredeeps, foredeep magmatism, and Superior-type iron-formations of the Canadian Shield. *Proterozoic lithospheric evolution*, *17*, 85-98. https://doi.org/10.1029/GD017p0085

Hoffman, P. F., Macdonald, F. A., & Halverson, G. P. (2011). Chapter 5 Chemical sediments associated with Neoproterozoic glaciation: iron formation, cap carbonate, barite and phosphorite. *Geological Society, London, Memoirs*, *36*(1), 67-80. https://doi.org/10.1144/M36.5

Holmden, C., Creaser, R. A., Muehlenbachs, K. L. S. A., Leslie, S. A., & Bergstrom, S. M. (1998). Isotopic evidence for geochemical decoupling between ancient epeiric seas and bordering oceans: implications for secular curves. *Geology*, *26*(6), 567-570. https://doi.org/10.1130/0091-7613(1998)026<0567:IEFGDB>2.3.CO;2

Horstwood, M. S., Košler, J., Gehrels, G., Jackson, S. E., McLean, N. M., Paton, C., ... & Schoene, B. (2016). Community-derived standards for LA-ICP-MS U-(Th-) Pb geochronology–Uncertainty propagation, age interpretation and data reporting. *Geostandards and Geoanalytical Research*, *40*(3), 311-332. https://doi.org/10.1111/j.1751-908X.2016.00379.x

Horton, F. (2015). Did phosphorus derived from the weathering of large igneous provinces fertilize the Neoproterozoic ocean? *Geochemistry, Geophysics, Geosystems*, *16*(6), 1723-1738. https://doi.org/10.1002/2015GC005792

Hurtgen, M. T., Arthur, M. A., Suits, N. S., & Kaufman, A. J. (2002). The sulfur isotopic composition of Neoproterozoic seawater sulfate: implications for a snowball Earth?. *Earth and Planetary Science Letters*, *203*(1), 413-429. https://doi.org/10.1016/S0012-821X(02)00804-X

Ilyin, A.V. and Zhuravleva, I.T., 1968, On the boundary between the Cambrian and the Precambrian at Prikhusugulie (Mongolian PR). *Dolkady Akademii Nauk SSSR,* v. 182, p. 1164-1166 (in Russian).

lyin, A. V. (1971). The Tuva–Mongolia Massif, Tr. *NIL Zarubezh-geologii (Proc. of NIL Zarubezhgeologiya), Nedra, Moskva*, *22*, 27-36.

Ilyin, A. V. (1973). Khubsugul Phosphorite-Bearing Basin. *Geologicheskiy Institut, Akademiya Nauk SSSR*, Moscow (in Russian).

Ilyin, A. V., & Ratnikova, G. I. (1981). Primary, bedded, structureless phosphorite of the Khubsugul Basin, Mongolia. *Journal of Sedimentary Research*, *51*(4), 1215-1222. https://doi.org/10.1306/212F7E69-2B24-11D7-8648000102C1865D

Ilyin, A. V. (2004). The Khubsugul phosphate-bearing basin: New data and concepts. *Lithology and Mineral Resources*, *39*, 454-467. https://doi.org/10.1023/B:LIMI.0000040735.76025.80

Ingall, E. D., & Van Cappellen, P. (1990). Relation between sedimentation rate and burial of organic phosphorus and organic carbon in marine sediments. *Geochimica et Cosmochimica Acta*, *54*(2), 373-386. https://doi.org/10.1016/0016-7037(90)90326-G

Jackson, S. E., Pearson, N. J., Griffin, W. L., & Belousova, E. A. (2004). The application of laser ablation-inductively coupled plasma-mass spectrometry to in situ U–Pb zircon geochronology. *Chemical geology*, *211*(1-2), 47-69. https://doi.org/10.1016/j.chemgeo.2004.06.017

Janoušek, V., Jiang, Y., Burianek, D., Schulmann, K., Hanžl, P., Soejono, I., Kröner, A., Altanbaatar, B., Vojtech, E., Lexa, O., Ganchuluun, T., and Košler, J. (2018). Cambrian–ordovician magmatism of the Ikh-Mongol Arc system exemplified by the Khantaishir Magmatic Complex (Lake Zone, south–central Mongolia). *Gondwana Research*, *54*, 122-149. https://doi.org/10.1016/j.gr.2017.10.003

Johnston, D. T., Macdonald, F. A., Gill, B. C., Hoffman, P. F., & Schrag, D. P. (2012). Uncovering the Neoproterozoic carbon cycle. *Nature*, *483*(7389), 320-323. https://doi.org/10.1038/nature10854

Karmysheva, I. V., Vladimirov, V. G., Rudnev, S. N., Yakovlev, V. A., & Semenova, D. V. (2021). Syntectonic metamorphism of a collisional zone in the Tuva-Mongolian massif, Central Asian Orogenic belt: PT conditions, U-Pb ages and tectonic setting. *Journal of Asian Earth Sciences*, *220*, 104919. https://doi.org/10.1016/j.jseaes.2021.104919

Khain, E. V., Bibikova, E. V., Kröner, A., Zhuravlev, D. Z., Sklyarov, E. V., Fedotova, A. A., & Kravchenko-Berezhnoy, I. R. (2002). The most ancient ophiolite of the Central Asian fold belt: U–Pb and Pb–Pb zircon ages for the Dunzhugur Complex, Eastern Sayan, Siberia, and geodynamic implications. *Earth and Planetary Science Letters*, *199*(3-4), 311-325. https://doi.org/10.1016/S0012-821X(02)00587-3

Kherzaskova, T. N. & Samygin, S. G. (1992). Tectonic conditions in the East Sayan Vendian – Middle Cambrian terrigenous carbonate association. *Geotectonics*, 26, 445–458.

Kheraskova, T. N., Samygin, S. G., Ruzhentsev, S. V., & Mossakovsky, A. A. (1995). Late Riphean marginal-continental volcanic belt of East Gondwana: transactions of Russian Academy of Sciences. *Earth Sciences Section*, *342*, 661-664.

Khukhuudei, U., Kusky, T., Otgonbayar, O., & Wang, L. (2020). the early palaeozoic mega-thrusting of the gondwana-derived altay–lake zone in Western Mongolia: Implications for the development of the central asian orogenic belt and paleo-asian ocean evolution. *Geological Journal*, *55*(3), 2129-2149. https://doi.org/10.1002/gj.3753

Kipp, M. A., & Stüeken, E. E. (2017). Biomass recycling and Earth's early phosphorus cycle. *Science advances*, *3*(11), eaao4795 DOI: 10.1126/sciadv.aao4795

Kohout, F. A. (1965). A hypothesis concerning cyclic flow of salt water related to geothermal heating in the Floridan aquifer. *Transactions of the New York Academy of Sciences*, *28*(2), 249-271.

Korobov, M.N., (1980). Lower Cambrian biostratigraphy and miomeran trilobites of Mongolia *Sovmestnaya Sovetsko-Mongol'skaya Geologicheskaya Ekspeditsiya, Trudy,* v. 26, p. 5–108. [in Russian]

Korobov, M.N., (1989). Lower Cambrian biostratigraphy and polymeran trilobites of Mongolia. *Sovmestnaya Sovetsko-Mongol'skaya Geologicheskaya Ekspeditsiya, Trudy,* v. 48, p. 1–204. [in Russian]

Korovnikov, I. V., & Lazarev, F. D. (2021). New findings of lower cambrian trilobites in the southern hövsgöl area (Mongolia) and their significance for stratigraphy and interregional correlation. *Russian Geology and Geophysics*, *62*(12), 1350-1358. https://doi.org/10.2113/RGG20204174

Kozakov, I. K., Kovach, V. P., Salnikova, E. B., Kröner, A., Adamskaya, E. V., Azimov, P. Y., ... & Plotkina, Y. V. (2021). Geochronology and Geodynamic Settings of Metamorphic Complexes in the Southwestern Part of the Tuva-Mongolian Terrane, Central Asian Foldbelt. *Stratigraphy and Geological Correlation*, *29*, 389-410. https://doi.org/10.1134/S0869593821030035

Kröner, A., Windley, B. F., Badarch, G., Tomurtogoo, O., Hegner, E., Jahn, B. M., ... & Wingate, M. T. D. (2007). Accretionary growth and crust formation in the Central Asian

Orogenic Belt and comparison with the Arabian-Nubian shield. https://doi.org/10.1130/2007.1200(11)

Kröner, A., Kovach, V., Belousova, E., Hegner, E., Armstrong, R., Dolgopolova, A., ... & Rytsk, E. (2014). Reassessment of continental growth during the accretionary history of the Central Asian Orogenic Belt. *Gondwana Research*, *25*(1), 103-125. https://doi.org/10.1016/j.gr.2012.12.023

Krogh, T. E. (1973). A low-contamination method for hydrothermal decomposition of zircon and extraction of U and Pb for isotopic age determinations. *Geochimica et Cosmochimica Acta*, *37*(3), 485-494. https://doi.org/10.1016/0016-7037(73)90213-5

Kuzmichev, A. B., Bibikova, E. V., & Zhuravlev, D. Z. (2001). Neoproterozoic (~ 800 Ma) orogeny in the Tuva-Mongolia Massif (Siberia): island arc–continent collision at the northeast Rodinia margin. *Precambrian Research*, *110*(1-4), 109-126. https://doi.org/10.1016/S0301-9268(01)00183-8

Kuzmichev, A., Sklyarov, E., Postnikov, A., & Bibikova, E. (2007). The Oka belt (southern Siberia and northern Mongolia): A Neoproterozoic analog of the Japanese Shimanto belt?. *Island Arc*, *16*(2), 224-242. https://doi.org/10.1111/j.1440-1738.2007.00568.x

Kuzmichev, A. B., & Larionov, A. N. (2011). The Sarkhoi Group in East Sayan: Neoproterozoic (~ 770–800 Ma) volcanic belt of the Andean type. *Russian Geology and Geophysics*, *52*(7), 685-700. https://doi.org/10.1016/j.rgg.2011.06.001

Kuzmichev, A. B. (2015). Neoproterozoic accretion of the Tuva-Mongolian massif, one of the Precambrian terranes in the Central Asian Orogenic Belt. *Composition and evolution of Central Asian Orogenic Belt: geology, evolution, tectonics, and models*, 66-92.

Kylander-Clark, A. R., Hacker, B. R., & Cottle, J. M. (2013). Laser-ablation split-stream ICP petrochronology. *Chemical Geology*, *345*, 99-112. https://doi.org/10.1016/j.chemgeo.2013.02.019

Laakso, T. A., Sperling, E. A., Johnston, D. T., & Knoll, A. H. (2020). Ediacaran reorganization of the marine phosphorus cycle. *Proceedings of the National Academy of Sciences*, *117*(22), 11961-11967. https://doi.org/10.1073/pnas.1916738117

Liu, P., Yin, C., Gao, L., Tang, F., & Chen, S. (2009). New material of microfossils from the Ediacaran Doushantuo Formation in the Zhangcunping area, Yichang, Hubei Province and its zircon SHRIMP U-Pb age. *Chinese Science Bulletin*, *54*(6), 1058-1064. https://doi.org/10.1007/s11434-008-0589-6

Liu, Z. R., & Zhou, M. F. (2017). Meishucun phosphorite succession (SW China) records redox changes of the early Cambrian ocean. *Bulletin*, *129*(11-12), 1554-1567. https://doi.org/10.1130/B31612.1

Liu, G., Qiao, X., Yu, P., Zhou, Y., Zhao, B., & Xiong, W. (2021). Rupture kinematics of the 11 January 2021 Mw 6.7 Hovsgol, Mongolia, earthquake and implications in the Western Baikal rift zone. *Seismological Research Letters*, *92*(6), 3318-3326. https://doi.org/10.1785/0220210061

Lyons, T. W., & Gill, B. C. (2010). Ancient sulfur cycling and oxygenation of the early biosphere. *Elements*, *6*(2), 93-99. https://doi.org/10.2113/gselements.6.2.93

Macdonald, F. A., Jones, D. S., & Schrag, D. P. (2009). Stratigraphic and tectonic implications of a newly discovered glacial diamictite–cap carbonate couplet in southwestern Mongolia. *Geology*, *37*(2), 123-126. https://doi.org/10.1130/G24797A.1

Macdonald, F. A., & Jones, D. S. (2011). Chapter 30 The Khubsugul Group, Northern Mongolia. *Geological Society, London, Memoirs*, *36*(1), 339-345. https://doi.org/10.1144/M36.30

Mattinson, J. M., Graubard, C. M., Parkinson, D. L., & McClelland, W. C. (1996). U-Pb reverse discordance in zircons: the role of fine-scale oscillatory zoning and sub-micron transport of Pb. *GEOPHYSICAL MONOGRAPH-AMERICAN GEOPHYSICAL UNION*, *95*, 355-370.

Mattinson, J. M. (2005). Zircon U–Pb chemical abrasion ("CA-TIMS") method: combined annealing and multi-step partial dissolution analysis for improved precision and accuracy of zircon ages. *Chemical Geology*, *220*(1-2), 47-66. https://doi.org/10.1016/j.chemgeo.2005.03.011

Maughan, E.K. (1994). Phosphoria Formation and its resource significance in the western interior, USA. In: Embry, A.F., Beauchamp, B., Glass, D.J. (Eds.), Pangea: Global Environments and Resources. Can. Soc. Petrol. Geol. Mem., vol. 17, pp. 479 – 495. Calgary

Mazumdar, A., & Banerjee, D. M. (1998). Stable isotope geochemistry of Early Cambrian Tal phosphorite of Krol Belt, Lesser Himalaya. *Mineralogical Magazine*, *62*(2), 977-978. https://doi.org/10.1130/0091-7613(1998)026<0899:SSSITE>2.3.CO;2

Mazumdar, A., Banerjee, D. M., Schidlowski, M., & Balaram, V. (1999). Rare-earth elements and stable isotope geochemistry of early Cambrian chert-phosphorite assemblages from the Lower Tal Formation of the Krol Belt (Lesser Himalaya, India). *Chemical geology*, *156*(1-4), 275-297. https://doi.org/10.1016/S0009-2541(98)00187-9

McFadden, K. A., Xiao, S., Zhou, C., & Kowalewski, M. (2009). Quantitative evaluation of the biostratigraphic distribution of acanthomorphic acritarchs in the Ediacaran Doushantuo Formation in the Yangtze Gorges area, South China. *Precambrian Research*, *173*(1-4), 170-190. https://doi.org/10.1016/j.precamres.2009.03.009

McLean, N. M., Bowring, J. F., & Bowring, S. A. (2011). An algorithm for U-Pb isotope dilution data reduction and uncertainty propagation. *Geochemistry, Geophysics, Geosystems*, *12*(6). https://doi.org/10.1029/2010GC003478

McLean, N. M., Condon, D. J., Schoene, B., & Bowring, S. A. (2015). Evaluating uncertainties in the calibration of isotopic reference materials and multi-element isotopic tracers (EARTHTIME Tracer Calibration Part II). *Geochimica et Cosmochimica Acta*, *164*, 481-501. https://doi.org/10.1016/j.gca.2015.02.040

Meert, J. G., Gibsher, A. S., Levashova, N. M., Grice, W. C., Kamenov, G. D., & Ryabinin, A. B. (2011). Glaciation and~ 770 Ma Ediacara (?) fossils from the lesser Karatau microcontinent, Kazakhstan. *Gondwana Research*, *19*(4), 867-880. https://doi.org/10.1016/j.gr.2010.11.008

Misi, A., & Kyle, J. R. (1994). Upper Proterozoic carbonate stratigraphy, diagenesis, and stromatolitic phosphorite formation, Irecê Basin, Bahia, Brazil. *Journal of Sedimentary Research*, *64*(2a), 299-310. https://doi.org/10.1306/D4267D84-2B26-11D7-8648000102C1865D

Mongolian Survey (1988). Geologic Map, Uranduush Uul. Geologic map M-47-45-A. (in Mongolian)

Mongush, A. A., Lebedev, V. I., Kovach, V. P., Sal'nikova, E. B., Druzhkova, E. K., Yakovleva, S. Z., ... & Serov, P. A. (2011). The tectonomagmatic evolution of structure-lithologic complexes in the Tannu-Ola zone, Tuva, in the Late Vendian–Early Cambrian (from geochemical, Nd isotope, and geochronological data). *Russian Geology and Geophysics*, *52*(5), 503-516. DOI: 10.1134/S1028334X11060328

Morais, L., Fairchild, T. R., Freitas, B. T., Rudnitzki, I. D., Silva, E. P., Lahr, D., ... & Trindade, R. I. F. D. (2021). Doushantuo-Pertatataka—like acritarchs from the Late Ediacaran Bocaina Formation (Corumbá Group, Brazil). *Frontiers in Earth Science*,1233. https://doi.org/10.3389/feart.2021.787011

Moreira, D. S., Uhlein, A., Uhlein, G. J., Sial, A. N., & Koester, E. (2021). Ediacaran/Early Cambrian Serra da Saudade Formation, Bambuí Group: the sedimentary record of a foreland basin in Southeastern Brazil. *Brazilian Journal of Geology*, *51*. https://doi.org/10.1590/2317-4889202120210029

Müller, R. D., Cannon, J., Williams, S., & Dutkiewicz, A. (2018). PyBacktrack 1.0: A tool for reconstructing paleobathymetry on oceanic and continental crust. *Geochemistry, Geophysics, Geosystems*, *19*(6), 1898-1909. https://doi.org/10.1029/2017GC007313

Munkhtsengel, B., Byambaa, J., & Tamiraa, A. (2021). Phosphate Deposits. *Mineral Resources of Mongolia*, 349-383. https://doi.org/10.1007/978-981-15-5943-3_12

Nelson, G. J., Pufahl, P. K., & Hiatt, E. E. (2010). Paleoceanographic constraints on Precambrian phosphorite accumulation, Baraga group, Michigan, USA. *Sedimentary Geology*, *226*(1-4), 9-21. https://doi.org/10.1016/j.sedgeo.2010.02.001

Nelson, L. L., Crowley, J. L., Smith, E. F., Schwartz, D. M., Hodgin, E. B., & Schmitz, M. D. (2023). Cambrian explosion condensed: High-precision geochronology of the lower Wood

Canyon Formation, Nevada. *Proceedings of the National Academy of Sciences*, *120*(30), e2301478120. https://doi.org/10.1073/pnas.2301478120

O'Brien, G. W., Milnes, A. R., Veeh, H. H., Heggie, D. T., Riggs, S. R., Cullen, D. J., ... & Cook, P. J. (1990). Sedimentation dynamics and redox iron-cycling: controlling factors for the apatite—glauconite association on the East Australian continental margin. *Geological Society, London, Special Publications*, *52*(1), 61-86. https://doi.org/10.1144/GSL.SP.1990.052.01.06

Osokin, P. V. & Tyzhinov, A. V. (1998). Precambrian Tilloids of the Oka- Khubsugul phosphorite-bearing basin (Eastern Sayan, Northwestern Mongolia). *Lithology and Mineral Resources*, 33, 142–154

Ouyang, Q., Guan, C., Zhou, C., & Xiao, S. (2017). Acanthomorphic acritarchs of the Doushantuo Formation from an upper slope section in northwestern Hunan Province, South China, with implications for early–middle Ediacaran biostratigraphy. *Precambrian Research*, *298*, 512-529. https://doi.org/10.1016/j.precamres.2017.07.005

Papineau, D. (2010). Global biogeochemical changes at both ends of the Proterozoic: insights from phosphorites. *Astrobiology*, *10*(2), 165-181. https://doi.org/10.1089/ast.2009.0360

Park, Y., Swanson-Hysell, N. L., MacLennan, S. A., Maloof, A. C., Gebreslassie, M., Tremblay, M. M., Schoene, B., Alene, M., Anttila, E.S.C., Tesema, T., & Haileab, B. (2020). The lead-up to the Sturtian Snowball Earth: Neoproterozoic chemostratigraphy time-calibrated by the Tambien Group of Ethiopia. *GSA Bulletin*, *132*(5-6), 1119-1149. https://doi.org/10.1130/B35178.1

Parry, L. A., Boggiani, P. C., Condon, D. J., Garwood, R. J., Leme, J. D. M., McIlroy, D., ... & Liu, A. G. (2017). Ichnological evidence for meiofaunal bilaterians from the terminal Ediacaran and earliest Cambrian of Brazil. *Nature Ecology & Evolution*, *1*(10), 1455-1464. https://doi.org/10.1038/s41559-017-0301-9

Paton, C., Woodhead, J. D., Hellstrom, J. C., Hergt, J. M., Greig, A., & Maas, R. (2010). Improved laser ablation U-Pb zircon geochronology through robust downhole fractionation correction. *Geochemistry, Geophysics, Geosystems*, *11*(3). https://doi.org/10.1029/2009GC002618

Pfänder, J. A., & Kröner, A. (2004). Tectono-magmatic evolution, age and emplacement of the Agardagh Tes-Chem ophiolite in Tuva, Central Asia: crustal growth by island arc accretion. *Developments in Precambrian Geology*, *13*, 207-221. https://doi.org/10.1016/S0166-2635(04)13006-5

Planavsky, N. J., Asael, D., Rooney, A. D., Robbins, L. J., Gill, B. C., Dehler, C. M., ... & Reinhard, C. T. (2023). A sedimentary record of the evolution of the global marine phosphorus cycle. *Geobiology*, *21*(2), 168-174. https://doi.org/10.1111/gbi.12536

Redfield, A. C. (1958). The biological control of chemical factors in the environment. *American scientist*, *46*(3), 230A-221.

Reinhard, C. T., Planavsky, N. J., Gill, B. C., Ozaki, K., Robbins, L. J., Lyons, T. W., ... & Konhauser, K. O. (2017). Evolution of the global phosphorus cycle. *Nature*, *541*(7637), 386-389. https://doi.org/10.1038/nature20772

Roest-Ellis, S., Richardson, J. A., Phillips, B. L., Mehra, A., Webb, S. M., Cohen, P. A., ... & Tosca, N. J. (2023). Tonian Carbonates Record Phosphate-Rich Shallow Seas. *Geochemistry, Geophysics, Geosystems*, *24*(5), e2023GC010974. https://doi.org/10.1029/2023GC010974

Romanek, C. S., Grossman, E. L., & Morse, J. W. (1992). Carbon isotopic fractionation in synthetic aragonite and calcite: effects of temperature and precipitation rate. *Geochimica et cosmochimica acta*, *56*(1), 419-430. https://doi.org/10.1016/0016-7037(92)90142-6

Rooney, A. D., Cantine, M. D., Bergmann, K. D., Gómez-Pérez, I., Al Baloushi, B., Boag, T. H., ... & Strauss, J. V. (2020). Calibrating the coevolution of Ediacaran life and environment. *Proceedings of the National Academy of Sciences*, *117*(29), 16824-16830. https://doi.org/10.1073/pnas.2002918117

Rudnev, S.N., Vladimirov, A.G., Ponomarchuk, V.A., Bibikova, E.V., Sergeev, S.A., Plotkina, Y.V., Bayanova, T.B. (2006). The Kaakhem polychronous granitoid batholith, eastern Tuva: composition, age, sources, and geodynamic setting. *Litosfera*, 200, 3–33 (in Russian).

Rudnev, S. N., Borisov, S. M., Babin, G. A., Levchenkov, O. A., Makeev, A. F., Serov, P. A., ... & Plotkina, Y. V. (2008). Early Paleozoic batholiths in the northern part of the Kuznetsk Alatau: composition, age, and sources. *Petrology*, *16*, 395-419. https://doi.org/10.1134/S086959110804005X

Ruttenberg, K. C. The global phosphorus cycle, in *Treatise on Geochemistry* Vol. 8 (eds Holland, H. D. & Turekian, K. K.) 585–643 (Pergamon, 2003). https://doi.org/10.1016/B0-08-043751-6/08153-6

Ruzhentsev, S. V., & Burashnikov, V. V. (1995). Tectonics of the western Mongolian Salairides. *Geotectonics*, *29*(5), 379-394.

Salama, W., El-Kammar, A., Saunders, M., Morsy, R., & Kong, C. (2015). Microbial pathways and palaeoenvironmental conditions involved in the formation of phosphorite grains, Safaga District, Egypt. *Sedimentary geology*, *325*, 41-58. https://doi.org/10.1016/j.sedgeo.2015.05.004

Sanders, C., & Grotzinger, J. (2021). Sedimentological and stratigraphic constraints on depositional environment for Ediacaran carbonate rocks of the São Francisco Craton: Implications for phosphogenesis and paleoecology. *Precambrian Research*, *363*, 106328. https://doi.org/10.1016/j.precamres.2021.106328

Sanders, C., Present, T., Marroquin, S., & Grotzinger, J. (2024). Sulfur geochemistry of the Salitre Formation phosphorites: Implications for the role of microbial ecology and sulfur cycling in phosphogenesis on an Ediacaran carbonate platform. *Geochimica et Cosmochimica Acta*, *367*, 41-57. https://doi.org/10.1016/j.gca.2023.12.033

Schulz, H. N., & Schulz, H. D. (2005). Large sulfur bacteria and the formation of phosphorite. *Science*, *307*(5708), 416-418. https://doi.org/10.1126/science.1103096

Sergeev, V. N., Schopf, J. W., & Kudryavtsev, A. B. (2020). Global microfossil changes through the Precambrian-Cambrian phosphogenic event: the Shabakta Formation of the phosphorite-bearing Maly Karatau Range, South Kazakhstan. *Precambrian Research*, *349*, 105386. https://doi.org/10.1016/j.precamres.2019.105386

Shaffer, G. (1986). Phosphate pumps and shuttles in the Black Sea. *Nature*, *321*(6069), 515-517. https://doi.org/10.1038/321515a0

Sheldon, R. P. (1984). Ice-ring origin of the Earth's atmosphere and hydrosphere and late Proterozoic – Cambrian phosphogenesis*, Phosphorite, Geological Survey of India Special Publication*, 17, Udaipur, Rajasthan, India.

Shields, G., Stille, P., & Brasier, M. D. (2000). Isotopic records across two phosphorite giant episodes compared: the Precambrian-Cambrian and the late Cretaceous-recent. https://doi.org/10.2110/pec.00.66.0103

Shkol'nik, S. I., Stanevich, A. M., Reznitskii, L. Z., & Savelieva, V. B. (2016). New data about structure and time of formation of the Khamar-Daban terrane: U-Pb LA-ICP-MS zircon ages. *Stratigraphy and Geological Correlation*, *24*, 19-38. https://doi.org/10.1134/S086959381506009X

Shiraishi, F., Ohnishi, S., Hayasaka, Y., Hanzawa, Y., Takashima, C., Okumura, T., & Kano, A. (2019). Potential photosynthetic impact on phosphate stromatolite formation after the Marinoan glaciation: Paleoceanographic implications. *Sedimentary Geology*, *380*, 65-82. https://doi.org/10.1016/j.sedgeo.2018.11.014

Sinclair, H. D., & Naylor, M. (2012). Foreland basin subsidence driven by topographic growth versus plate subduction. *Bulletin*, *124*(3-4), 368-379. https://doi.org/10.1130/B30383.1

Sláma, J., Košler, J., Condon, D. J., Crowley, J. L., Gerdes, A., Hanchar, J. M., ... & Whitehouse, M. J. (2008). Plešovice zircon—a new natural reference material for U–Pb and Hf isotopic microanalysis. *Chemical Geology*, *249*(1-2), 1-35.https://doi.org/10.1016/j.chemgeo.2007.11.005

Smith, E. F., Macdonald, F. A., Petach, T. A., Bold, U., & Schrag, D. P. (2016). Integrated stratigraphic, geochemical, and paleontological late Ediacaran to early Cambrian records from southwestern Mongolia. *Bulletin*, *128*(3-4), 442-468. https://doi.org/10.1130/B31248.1

Southgate, P. N. (1980). Cambrian stromatolitic phosphorites from the Georgina Basin, Australia. *Nature*, *285*(5764), 395-397. https://doi.org/10.1038/285395a0

Spencer, C. J., Kirkland, C. L., & Taylor, R. J. (2016). Strategies towards statistically robust interpretations of in situ U–Pb zircon geochronology. *Geoscience Frontiers*, *7*(4), 581-589. https://doi.org/10.1016/j.gsf.2015.11.006

Stockey, R. G., Cole, D. B., Farrell, U. C., Agić, H., Boag, T. H., Brocks, J. J., Canfield, D.E., Chang, M., Crockford, P.W., Cui, H., Dahl, T.W., Del Mouro, L., Dewing, K., Dornbos, S.Q., Emmings, J.F., Gaines, R.R., Gibson, T.M., Gill, B.C., Gilleaudeau, G.J., Goldberg, K., Guilbaud, R., Halverson, G., Hammarlund, E.U., Hantsoo, K., Henderson, M.A., Henderson, C.M., Hodgskiss, M.S.W., Jarrett, A.J.M., Johnston, D.T., Kabanov, P., Kimmig, J., Knoll, A.H., Kunzmann, M., LeRoy, M.A., Li, C., Loydell, D.K., Macdonald, F.A., Magnall, J. M., Mills, N.T., Och, L.M., O'Connell, B., Pages, A., Peters, S.E., Porter, S.M., Poulton, S.W., Ritzer, S.R., Rooney, A.D., Schoepfer, S., Smith, E.F., Strauss, J.V., Uhlein, G.J., White, T., Wood, R.A., Woltz, C.R., Yurchenko, I., Planavsky, N.J., & Sperling, E. A. (2024). Sustained increases in atmospheric oxygen and marine productivity in the Neoproterozoic and Palaeozoic eras. *Nature Geoscience*, 1-8. https://doi.org/10.1038/s41561-024-01479-1

Sundby, B., Anderson, L. G., Hall, P. O., Iverfeldt, Å., van der Loeff, M. M. R., & Westerlund, S. F. (1986). The effect of oxygen on release and uptake of cobalt, manganese, iron and phosphate at the sediment-water interface. *Geochimica et Cosmochimica Acta*, *50*(6), 1281-1288. https://doi.org/10.1016/0016-7037(86)90411-4

Swart, P. K., & Eberli, G. (2005). The nature of the δ13C of periplatform sediments: Implications for stratigraphy and the global carbon cycle. *Sedimentary Geology*, *175*(1-4), 115-129. https://doi.org/10.1016/j.sedgeo.2004.12.029

Szymanowski, D., & Schoene, B. (2020). U–Pb ID-TIMS geochronology using ATONA amplifiers. *Journal of Analytical Atomic Spectrometry*, *35*(6), 1207-1216. https://doi.org/10.1039/D0JA00135J

Teng, L. S., Lee, C. T., Tsai, Y. B., & Hsiao, L. Y. (2000). Slab breakoff as a mechanism for flipping of subduction polarity in Taiwan. *Geology*, *28*(2), 155-158. https://doi.org/10.1130/0091-7613(2000)28<155:SBAAMF>2.0.CO;2

Tyrrell, T. (1999). The relative influences of nitrogen and phosphorus on oceanic primary production. *Nature*, *400*(6744), 525-531. https://doi.org/10.1038/22941

Uhlein, G. J., Uhlein, A., Halverson, G. P., Stevenson, R., Caxito, F. A., Cox, G. M., & Carvalho, J. F. (2016). The Carrancas Formation, Bambuí Group: a record of pre-Marinoan sedimentation on the southern São Francisco craton, Brazil. *Journal of South American Earth Sciences*, *71*, 1-16. https://doi.org/10.1016/j.jsames.2016.06.009

Valetich, M., Zivak, D., Spandler, C., Degeling, H., & Grigorescu, M. (2022). REE enrichment of phosphorites: An example of the Cambrian Georgina Basin of Australia. *Chemical Geology*, *588*, 120654. https://doi.org/10.1016/j.chemgeo.2021.120654

Van Cappellen, P., Gaillard, J. F., & Rabouille, C. (1993). Biogeochemical transformations in sediments: kinetic models of early diagenesis. In *Interactions of C, N, P and S biogeochemical cycles and global change* (pp. 401-445). Springer Berlin Heidelberg. https://doi.org/10.1007/978-3-642-76064-8_17

Vermeesch, P. (2018). IsoplotR: A free and open toolbox for geochronology. *Geoscience Frontiers*, *9*(5), 1479-1493. https://doi.org/10.1016/j.gsf.2018.04.001

Wendt, I., & Carl, C. (1991). The statistical distribution of the mean squared weighted deviation. *Chemical Geology: Isotope Geoscience Section*, *86*(4), 275-285. https://doi.org/10.1016/0168-9622(91)90010-T

Wiedenbeck, M. A. P. C., Alle, P., Corfu, F. Y., Griffin, W. L., Meier, M., Oberli, F. V., ... & Spiegel, W. (1995). Three natural zircon standards for U-Th-Pb, Lu-Hf, trace element and REE analyses. *Geostandards newsletter*, *19*(1), 1-23. https://doi.org/10.1111/j.1751-908X.1995.tb00147.x

Wilde, S. A. (2015). Final amalgamation of the Central Asian Orogenic Belt in NE China: Paleo-Asian Ocean closure versus Paleo-Pacific plate subduction—A review of the evidence. *Tectonophysics*, *662*, 345-362. https://doi.org/10.1016/j.tecto.2015.05.006

Willman, S., Peel, J. S., Ineson, J. R., Schovsbo, N. H., Rugen, E. J., & Frei, R. (2020). Ediacaran Doushantuo-type biota discovered in Laurentia. *Communications Biology*, *3*(1), 647. https://doi.org/10.1038/s42003-020-01381-7

Windley, B. F., Alexeiev, D., Xiao, W., Kröner, A., & Badarch, G. (2007). Tectonic models for accretion of the Central Asian Orogenic Belt. *Journal of the Geological Society*, *164*(1), 31-47. https://doi.org/10.1144/0016-76492006-02

Wu, X., Baas, J. H., Parsons, D. R., Eggenhuisen, J., Amoudry, L., Cartigny, M., ... & Ruessink, G. (2018). Wave ripple development on mixed clay-sand substrates: effects of clay winnowing and armoring. *Journal of Geophysical Research: Earth Surface*, *123*(11), 2784-2801. https://doi.org/10.1029/2018JF004681

Xiao, S., Zhang, Y., & Knoll, A. H. (1998). Three-dimensional preservation of algae and animal embryos in a Neoproterozoic phosphorite. *Nature*, *391*(6667), 553-558. https://doi.org/10.1038/35318

Xiao, S., & Knoll, A. H. (1999). Fossil preservation in the Neoproterozoic Doushantuo phosphorite lagerstätte,South China. *Lethaia*, *32*(3), 219-238. https://doi.org/10.1111/j.1502-3931.1999.tb00541.x

Xiao, S., & Knoll, A. H. (2000). Phosphatized animal embryos from the Neoproterozoic Doushantuo formation at Weng'an, Guizhou, South China. *Journal of Paleontology*, *74*(5), 767-788. https://doi.org/10.1666/0022-3360(2000)074<0767:PAEFTN>2.0.CO;2

Xiao, W., Windley, B. F., Hao, J., & Zhai, M. (2003). Accretion leading to collision and the Permian Solonker suture, Inner Mongolia, China: Termination of the central Asian orogenic belt. *Tectonics*, *22*(6). https://doi.org/10.1029/2002TC001484

Xiao, S., Zhou, C., Liu, P., Wang, D., & Yuan, X. (2014). Phosphatized Acanthomorphic Acritarchs and Related Microfossils from the Ediacaran Doushantuo Formation at Weng'an (South China) and their Implications for Biostratigraphic Correlation. *Journal of Paleontology*, *88*(1), 1-67. https://doi.org/10.1666/12-157R

Xiao, S., Jiang, G., Ye, Q., Ouyang, Q., Banerjee, D. M., Singh, B. P., ... & Hughes, N. C. (2022). Systematic paleontology, acritarch biostratigraphy, and δ13C chemostratigraphy of the early Ediacaran Krol A Formation, Lesser Himalaya, northern India. *Journal of Paleontology*, 1-62. doi: 10.1017/jpa.2022.7

Yang, C., Rooney, A. D., Condon, D. J., Li, X. H., Grazhdankin, D. V., Bowyer, F. T., ... & Zhu, M. (2021). The tempo of Ediacaran evolution. *Science advances*, *7*(45), eabi9643. https://doi.org/10.1126/sciadv.abi9643

Yang, C., Li, X. H., & Zhu, M. Y. (2022). Tectonic regime transition of the western South China Block in early Cambrian: Evidence from the Meishucun volcanic ash beds. *Palaeoworld*, *31*(4), 591-599. https://doi.org/10.1016/j.palwor.2022.03.003

Zhegallo, E. A. (2000). *Atlas of microorganisms from ancient phosphorites of Khubsugul (Mongolia)*. National Aeronautics and Space Administration, Marshall Space Flight Center.

Zhou, C., Xiao, S., Wang, W., Guan, C., Ouyang, Q., & Chen, Z. (2017). The stratigraphic complexity of the middle Ediacaran carbon isotopic record in the Yangtze Gorges area, South China, and its implications for the age and chemostratigraphic significance of the Shuram excursion. *Precambrian Research*, *288*, 23-38. https://doi.org/10.1016/j.precamres.2016.11.007

* * *

## APPENDIX

***1. Carbonate Geochemistry*** - powdered carbonate samples from sections EA1701-05, JP1716-17, MG32, EA1801,-02,-05 and -20 were analyzed in the Stable Isotope Laboratory of the Precambrian Research Office at McGill University. Subsamples of each aliquot of carbonate powder were loaded into glass vials and individually dissolved in $H_3PO_4$ on a NuCarb automated carbonate preparation device. The resultant $CO_2$ analyte from each sample was measured on a Nu Instruments Perspective IRMS. Both $\delta^{13}C$ and $\delta^{18}O$ measurements have an analytical uncertainty of <0.05‰ (1σ ) based on measurements of NCM and UQ-6 standards.

Samples from all other sections were analyzed at the Center for Stable Isotope Biogeochemistry at the University of California Berkeley. 10-100 microgram subsamples of each powder aliquot were reacted with concentrated $H_3PO_4$ at 90ºC for 10 mins to generate $CO_2$ gas for coupled $\delta^{13}C$ and $\delta^{18}O$ analysis using a GV IsoPrime mass spectrometer with Dual-Inlet and MultiCarb systems. Several replicates of one international standard NBS19, and two lab standards $CaCO_3$-I & II were measured along with approximately 40 unknowns for each run. The overall external analytical precision was about $\pm$0.05‰ for $\delta^{13}C$ and about $\pm$0.07‰ for $\delta^{18}O$.

**2. Zircon Geochronology** - Samples were cleaned and trimmed to remove potential contamination, and pulverized in an industrial jaw crusher. The resultant <500 micron fraction was collected, and subsequently washed in an antiflocculant solution to remove ultrafine material. Samples were then panned to isolate heavy minerals. Samples containing few zircon were further magnetically separated with a Frantz device (0.4A at a 20º incline), and put through a final density separation in methylene iodide. Zircon grains were individually picked from resultant heavy mineral separates, annealed in a muffle furnace for 48 hours at 900ºC, mounted in epoxy, and polished. The internal structures of the grains were mapped with cathodoluminescence (CL) imaging using a Cameca SX-100 Electron Probe Micro-Analyzer (EPMA) with a CL detector.

*2.1 Laser ablation inductively coupled plasma mass spectrometry (LA-ICPMS) analyses*

LA-ICPMS U-Pb geochronological analyses on zircon were completed at UCSB, using a Cetac/Photon Machines Analyte Excite 193 nm excimer laser attached to a Nu Plasma 3D multicollector ICPMS, following the methods of Kylander-Clark et al. (2013). Each zircon was ablated with a 20µm laser spot. The zircon 91500 (Wiedenbeck et al., 1995) was used for age calibration. Secondary zircon reference materials included 9435, AUSZ, Mudtank, GJ1 (Jackson et al., 2004), and Plesovice (Sláma et al., 2008). *Iolite* (Paton et al., 2010) was used to correct for U-Pb mass bias and drift following the methods of Kylander-Clark et al. (2013) and Horstwood et al. (2016). The resultant U and Pb isotopic ratios were reduced according to methods outlined in Kylander-Clark et al. (2013). Dates for each analyzed grain were calculated by importing reduced $^{238}U/^{206}Pb$ and $^{207}Pb/^{206}Pb$ ratios into *IsoplotR* (Vermeesch, 2018). For appropriate magmatic samples, a weighted mean age for each sample was calculated by isolating a group of analyses that conform to statistical standards of a single magmatic population as outlined in Spencer et al. (2016) and references therein.

Detrital zircon normalized probability plots were created for all detrital samples. Discordant analyses from detrital samples were removed by excluding all analyses exhibiting more than 15% discordance. Reversely discordant analyses greater than -10% discordant were also included in the compilation, with reverse discordance assumed to be attributed to a range of potential factors (see Mattinson et al., 1996) putatively associated with various metamorphic events in the region. Ages from the resultant filtered dataset were incorporated into a kernel density estimation (KDE) function with 5 Myr bins (full code available in the Supplementary Information/GitHub repository). Because the detrital populations of interest in our samples are of Tonian and younger age, we present detrital spectra of ages up to 1Ga, and as such only utilize the $Pb^{206}/U^{238}$ ages of each analysis in the KDE. Maximum depositional ages (MDAs) were determined by using the age of the youngest individual grain in the sample, or the weighted mean of the youngest group of grains in the case of samples with a cluster of young analyses that conform to MSWD criteria for a single magmatic population (Wendt and Carl., 1991; Spencer et al., 2016). Additional CA-ID-TIMS analyses were conducted on a subset of grains used to calculate MDAs, methods for which are outlined below.

*2.2 Chemical abrasion isotope dilution thermal ionization mass spectrometry (CA-ID-TIMS) analyses*

Individual grains from the population of zircons that make up the LA-ICPMS weighted mean age for magmatic samples or the MDA of detrital samples were analyzed with single zircon U-Pb chemical abrasion isotope dilution thermal ionization mass spectrometry (CA-ID-TIMS) at Princeton University, following standard chemical abrasion methods modified from Mattinson (2005). Previously annealed single zircons were plucked from epoxy mounts, transferred to Teflon beakers, and rinsed with 3N $HNO_3$. Grains were removed from the acid rinse and loaded into 200 µl Savillex microcapsules with ca. 90 µl 29M HF. Microcapsules were assembled in a Parr bomb and zircons were initially leached at 180ºC for 12 hours to remove domains in the crystal lattice that may have experienced lead loss. These first leaching experiments caused complete dissolution of many grains, so a subsequent round of leaching was completed at 180ºC for only 4.5 hours in order to avoid complete destruction of the grains. While this leaching step did not result in the total dissolution of any zircon crystals, it introduced the possibility of the incorporation of crystallographic domains with possible lead-loss into the resultant analyte. Only one zircon (EA1905-46B) from this lower-duration leach appears to have incorporated significant lead loss; as a result, we omit the data from this grain from maximum depositional age calculations for this sample, but have included the data in Table SI3.

Following leaching, zircon grains were transferred to Teflon beakers, and repeatedly rinsed in 3N $HNO_3$ and 6N HCl. The crystals were then transferred back to clean microcapsules, spiked with the EARTHTIME $^{205}$Pb-$^{233}$U-$^{235}$U tracer (ET535; Condon et al., 2015; McLean et al., 2015) and placed back into a Parr bomb for dissolution in ca. 90 µl 29M HF for 60 h at 210ºC. The resulting solutions were then dried down, converted to chlorides in the Parr bomb overnight, and dried down once more on the hot plate. The samples were then redissolved in 3N HCl and loaded into 50 µl microcolumns filled with AG-1 X8 resin, where U-Pb and trace element solutions were separated by anion exchange following methods modified from Krogh (1973). The U-Pb solution was dried down in a Teflon beaker on the hot plate with a microdrop of 0.015M $H_3PO_4$. Each aliquot was then redissolved in a silica gel emitter (Gerstenberger and Haase, 1997), and loaded with an ultrafine pipette onto a single outgassed zoned-refined rhenium filament.

Lead and U isotopic measurements were performed with one of two Isotopx Phoenix thermal ionization mass spectrometers (TIMS) at Princeton University. Pb isotopes were measured using peak-hopping mode on a Daly photomultiplier ion-counter, while U isotopes were measured as $UO_2$ in static mode with either Faraday cups coupled to traditional $10^{12}$ Ω amplifiers, or to ATONA amplifiers (Szymanowski and Schoene, 2020). Instrumental mass fractionation for Pb was corrected with a factor (0.14 or 0.18 %/amu) derived from a long-term compilation of in-run $^{202}$Pb/$^{205}$Pb values of previous measurements of samples spiked with an ET2535 trace solution on each TIMS instrument. The dead time corrections for of the Daly amplifier systems was kept constant throughout the period of the study, but was monitored through repeat analyses of the NIST SRM 982 Pb isotope standard over a range of intensities. All common Pb was considered laboratory blank and was corrected using the long-term isotopic composition of the Pb blank at Princeton University. U runs were corrected for fractionation using the known $^{233}$U/$^{235}$U composition of the spike (Condon et al., 2015) and assuming a sample $^{238}$U/$^{235}$U of 137.818 ± 0.045 (2σ; Hiess et al., 2012). An $^{18}$O/$^{16}$O value of 0.002051 ± 0.000010

(1σ) was used to correct for interferences in $UO_2$ analyses based on previous measurements of the U500 standard solution (Szymanowski and Schoene, 2020).

Data was compiled and reduced in *Tripoli* and *ET_Redux* (Bowring et al., 2011; McLean et al., 2011). Initial $^{230}$Th disequilibrium in the $^{206}$Pb/$^{238}$U system was corrected for each grain by estimating $(Th/U)_{magma}$ using a fixed $(Th/U)_{zircon\text{-}magma}$ partition coefficient ratio of 0.19 ± 0.06 (1s) based on a compilation of natural zircon–melt pairs, and uncertainties for the $(Th/U)_{magma}$ were propagated into final date uncertainty for each grain. Weighted-mean ages were calculated in *ET_Redux.*

*3. Backstripping calculations*

A representative tectonic subsidence curve for the Khuvsgul Group was calculated by entering stratigraphic thickness estimates, model ages, approximations of lithological composition, and estimated paleo-depths of deposition for all Khuvsgul Group strata into the backstripping model of Müller et al. (2018). All model inputs, as well assumptions about lithological density, porosity, and permeability, are tabulated in Table SI4; full code used to generate fig. 12 is available within the Supplemental Information as an attached GitHub repository.

* * *

# FIGURES

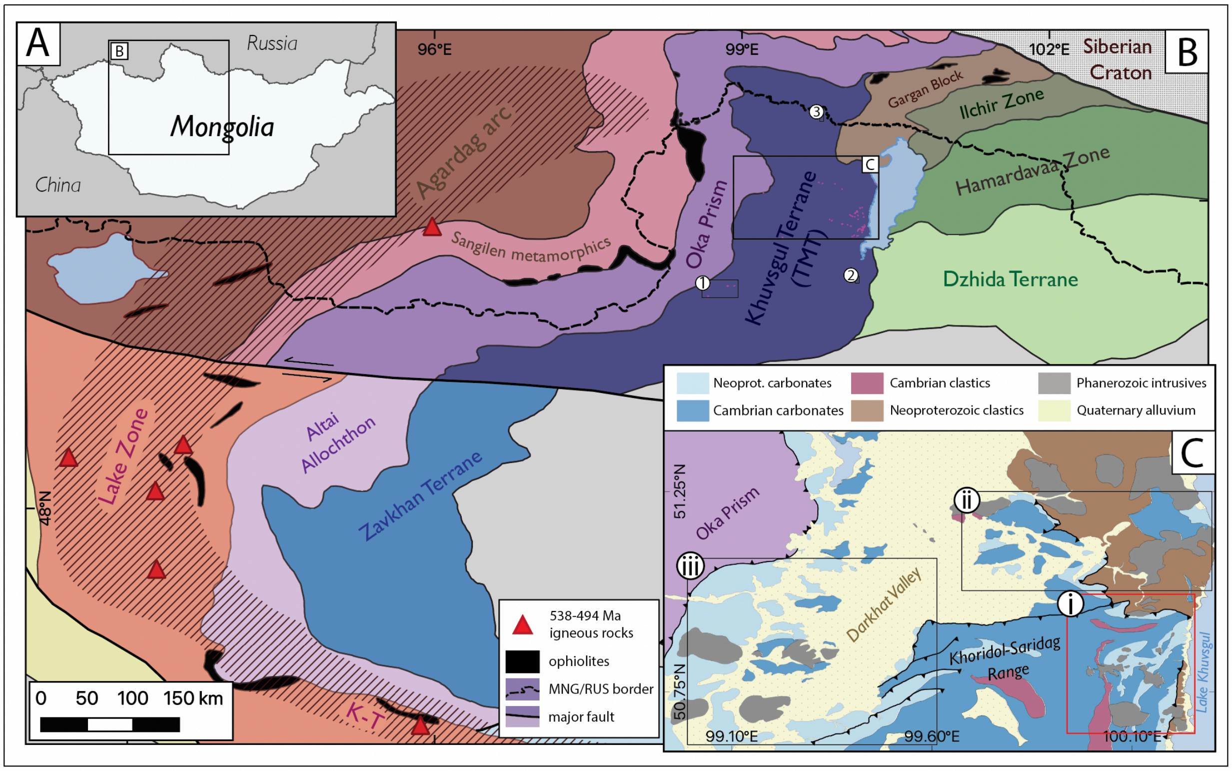


Figure 1. Location and geological context of study area: A) geopolitical overview map, contextualizing B) the Mongolian Central Asian Orogenic Belt, modified from Bold et al. (2016b; 2019) and Kuzmichev (2015). The Khuvsgul Terrane forms the core of the composite Tuva Mongolia Terrane (TMT). The location of 538-494 Ma igneous rocks, as well as the hashed area indicating the putative extent of the Ikh-Mongol continental arc, are modified from Janoušek et al. (2018). The numerals 1, 2, and 3 indicate the positions of the Bayan Zurgh, Eg Gol, and Khoroo Gol study areas, respectively. C) Generalized geologic map of the main Khuvsgul study area, compiled from both original and extant geological mapping (Buihover et al., 1968). Boxes with numerals i, ii, and iii indicate the extent of the Khoridol Saridag, northern, and Darkhat Valley mapping regions, respectively. A 1:100,000 geological map of the Khoridol Saridag mapping area can be found in figure 3; geologic maps of the Northern and Darkhat Valley mapping areas can be found in the Supplementary Information.

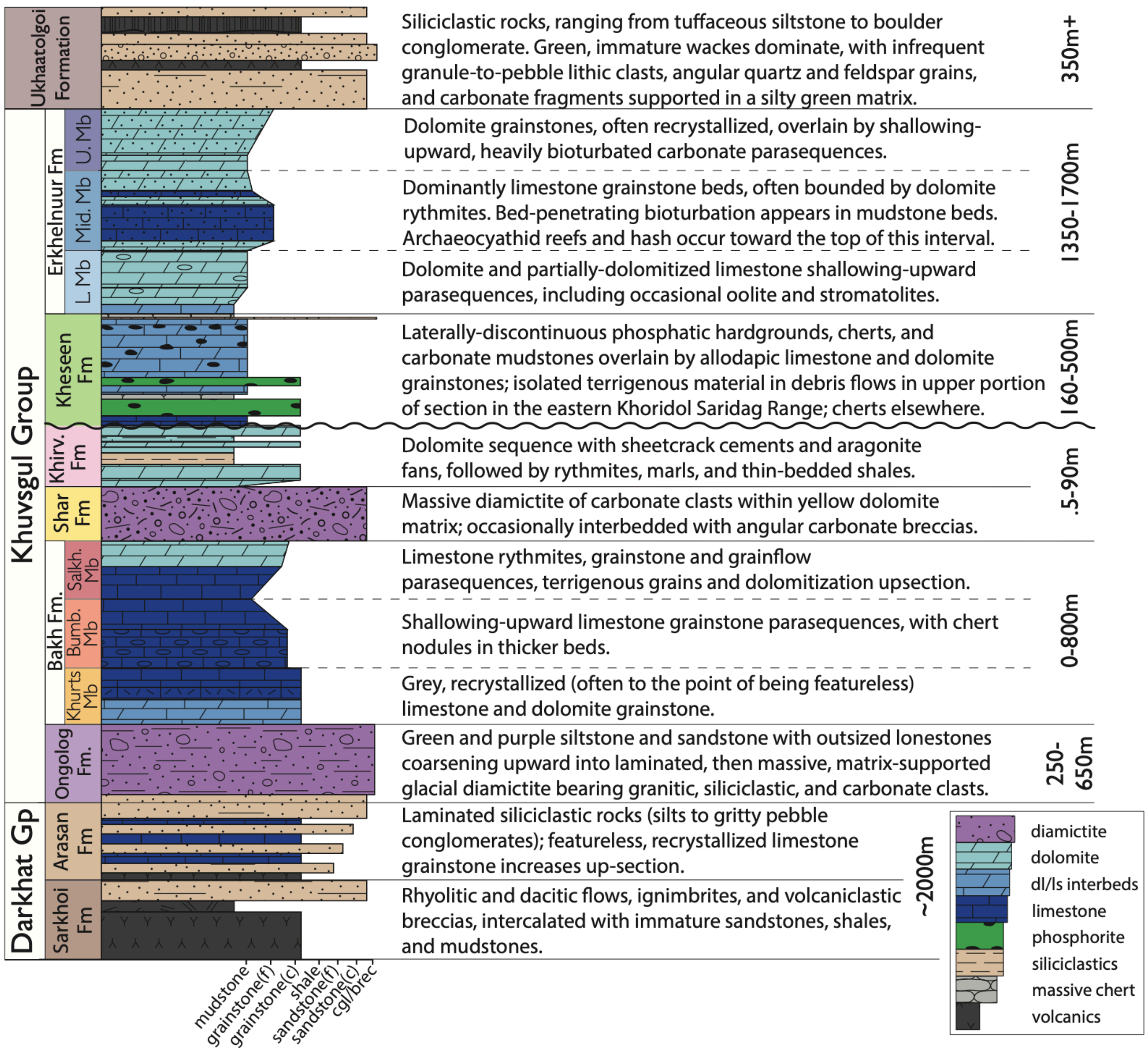


Figure 2. Generalized stratigraphy of the Khuvsgul Group and adjacent strata, after Anttila et al. (2021).

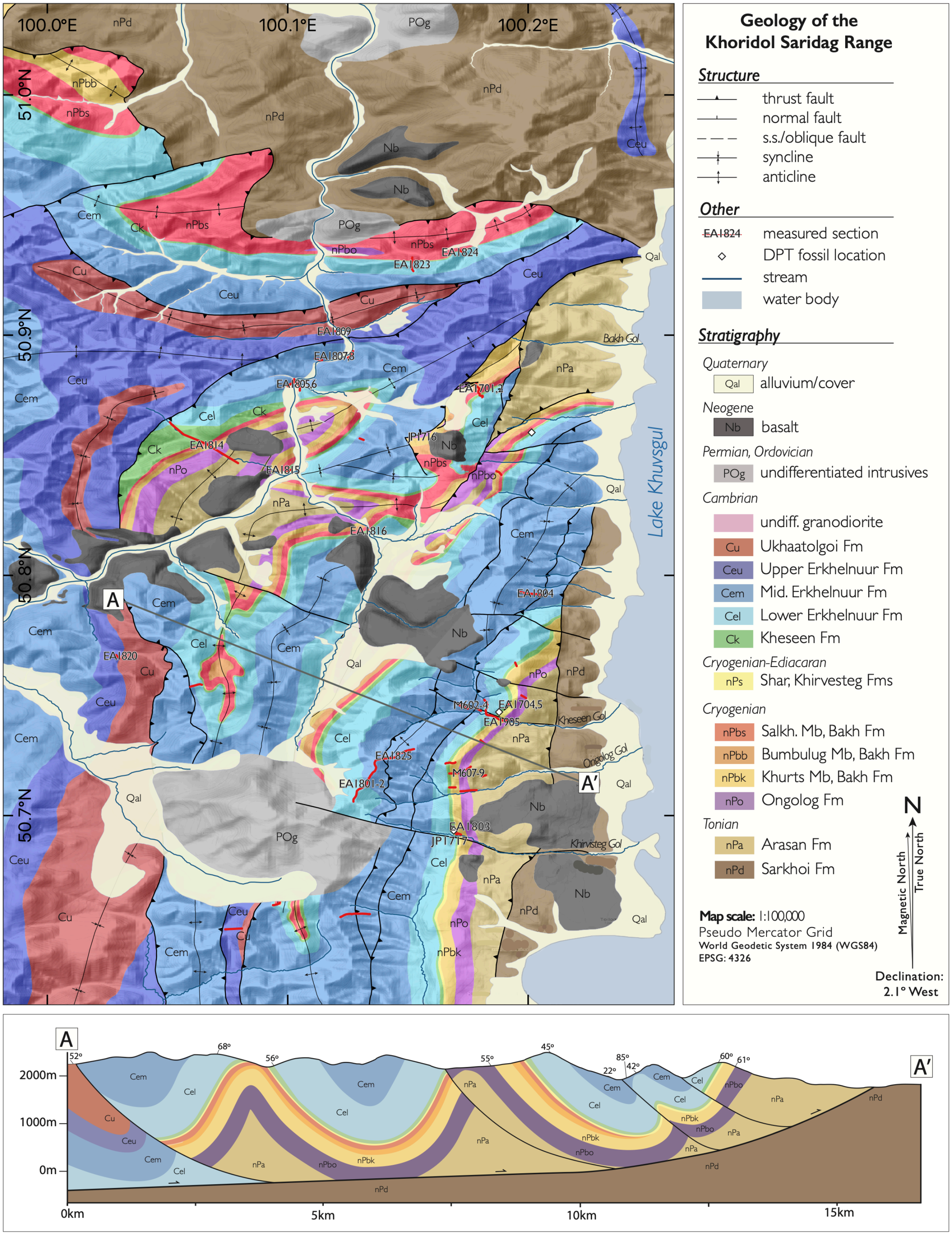


Figure 3: Original geologic map of the Khuvsgul Group in the Khoridol Saridag Range. The location of schematic cross section A-A' is shown in the main map panel. A companion map highlighting the broad structural features of this map area is provided in the Supplementary Information (fig. S1).

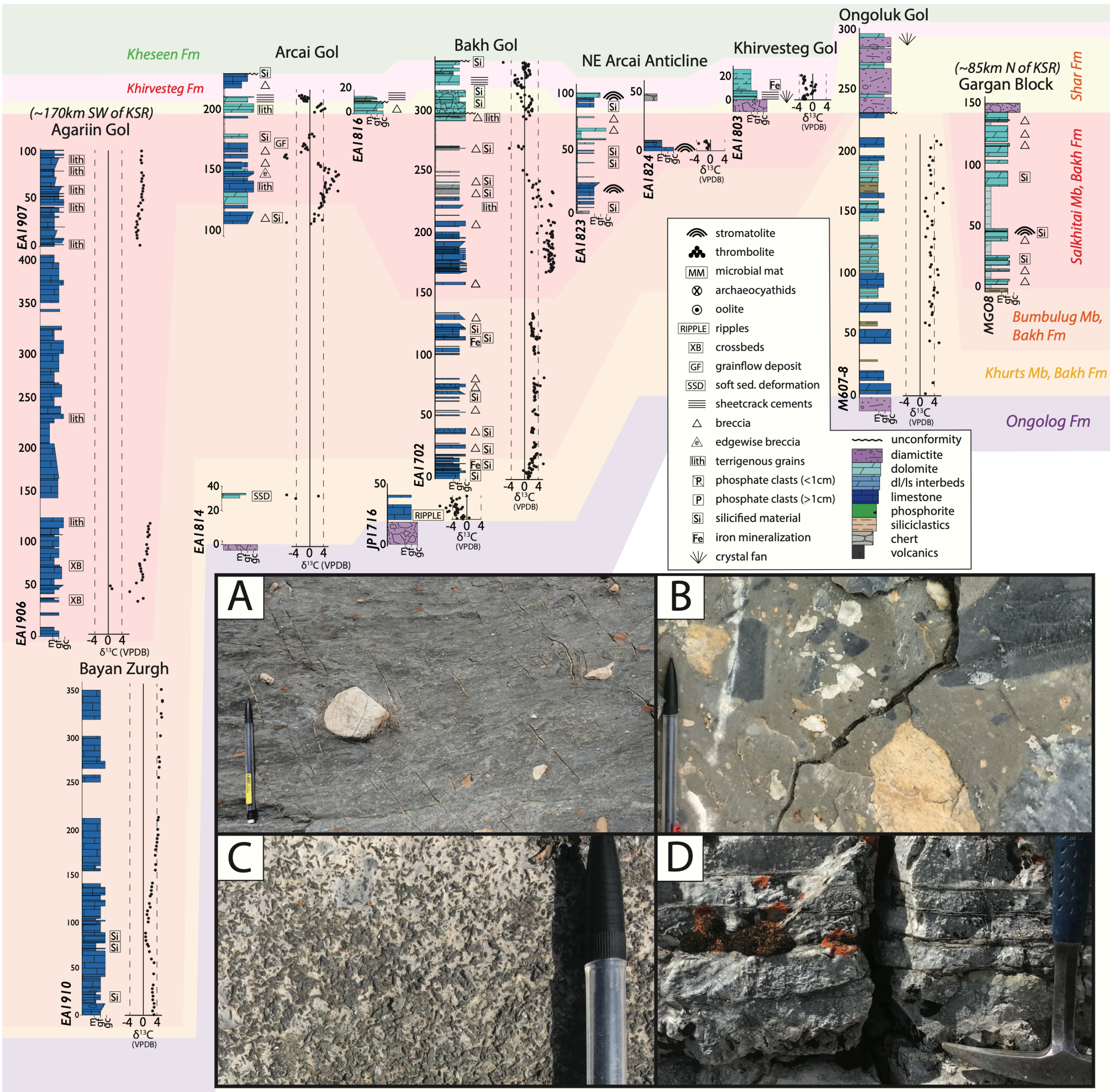


Figure 4: Cryogenian chemostratigraphy of the Khuvsgul Group, with field photographs of Cryogenian lithologies depicted in inset panels A-D. Stratigraphic sections are arranged, from left to right, along a broadly southwest-northeast transect. Geochemical data and section locations are collated in the Supplementary Information (Tables S1, S3). A) massive, matrix supported diacmictite of the Ongolog Fm. B) massive diamictite of the Shar Fm, featuring carbonate clasts in a dolostone matrix. C) barite pseudomorphs on a dolomite grainstone bedding plane in the basal Khirvesteg Fm. D) sheetcrack cements in dolomite mudstones of the basal Khirvesteg Fm. The mechanical pencil in panels A-C is 15.5 cm in overall length; the hammer in panel D is 33 cm long overall.

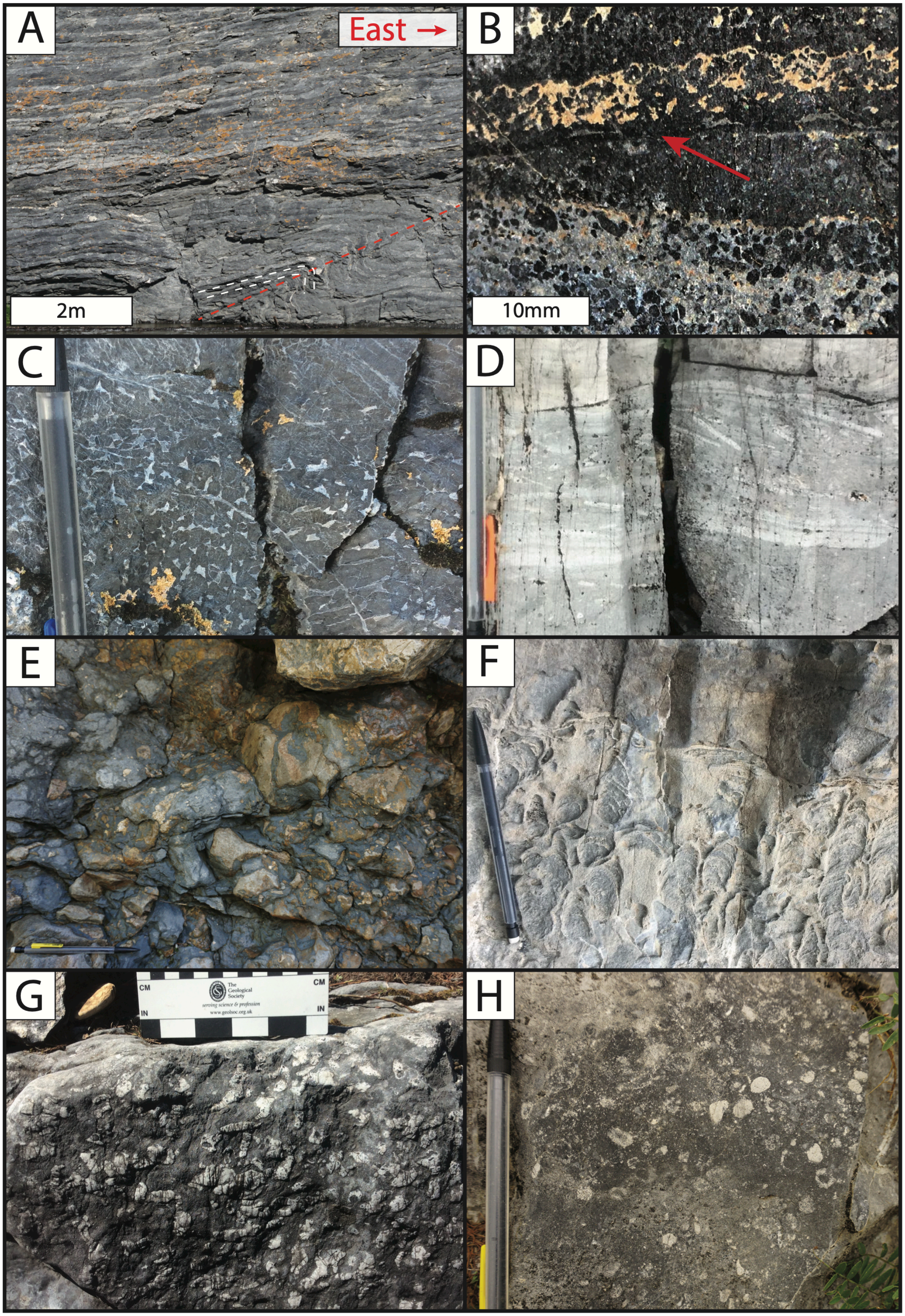
A
East →
2m
B
10mm
C
D
E
F
G
CM
IN
The Geological Society
serving science & profession
www.geolsoc.org.uk
CM
IN
H

2218

Figure 5. Field photographs of Khuvsgul Group strata. A) Outcrop-scale photograph of well-bedded mudstone-grainstone parasequences of the Salkhitai Mb of the Bakh Fm near Agariin Gol. White dashed lines highlight bedding planes through a m-scale fold, with elongated west-dipping fold arms indicating top-to-the-east shear. The trend of the fold axis highlighted by the red dashed line is parallel to the trend of D1 structures in the Khoridol Saridag Range. B) phosphatic grainstone of the Kheseen Fm, featuring truncated bedding as well as horizons indicative of primary/multigenerational phosphogenesis. The red arrow indicates the location of a multigenerational phosphogenic horizon (phosphatic allochems in authigenic CFA cement). C) thrombolytic texture in a phosphatic grainstone interval of the Kheseen Fm. D) imbricate, edgewise breccia horizon within the Kheseen Fm, featuring rip-up clasts of underlying strata. E) wildflysch of the upper Kheseen Fm at Kheseen Gol. Clasts include material similar to underlying Kheseen strata, suggesting an erosive contact at the base of the interval. F) digitate stromatolites in a dolomite grainstone interval of the Middle Mb of the Erkhelnuur Fm. G) bed-penetrating ichnofossils in a limestone grainstone bed of the Middle Mb of the Erkhelnuur Fm. H) disassociated archaeocyathid allochems in dolomite grainstone bed of the Upper Mb of the Erkhelnuur Fm. The mechanical pencil in panels C-F and H is 15.5 cm in overall length.

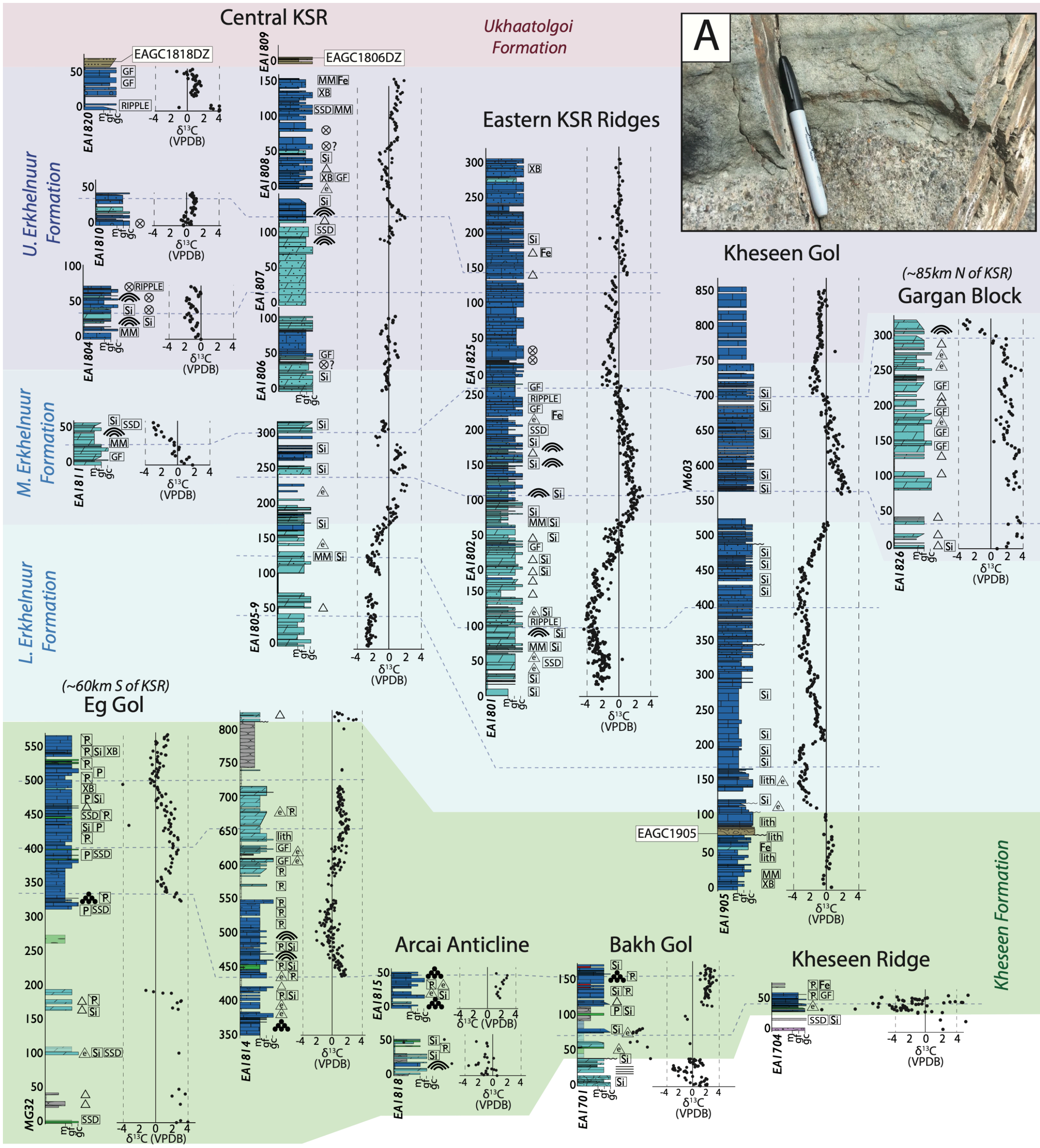


Figure 6. Cambrian chemostratigraphy of the Khuvsgul Group, and a field photograph of the Ukhaatologoi Fm (inset panel A). Stratigraphic sections are arranged, from left to right, along a broadly southwest-northeast transect. A legend defining all lithological and sedimentary symbology can be found in Figure 11. Geochemical data and section locations are collated in Supplementary Information (Tables S1, S3. The stratigraphic heights of geochronological samples collected within the measured sections presented here are highlighted with white-boxed labels. The pen in panel A is 13.7 cm in overall length.

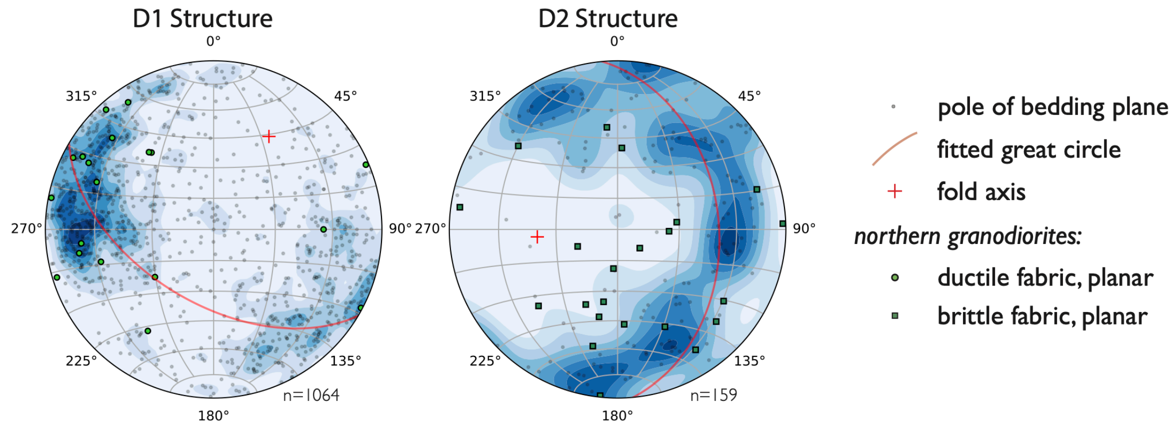


Figure 7: Stereonets showing the orientations of km-scale folds in the Khoridol Saridag Range that are representative of D1 and D2 structures, respectively. Individual bedding measurements are depicted as poles to bedding planes. Ductile fabrics (dominantly folded foliation) observed in granodiorites from the Northern mapping region (including EAGC1942, 1943, and 1944) are shown on the D1 stereonet, while brittle fabrics (dominantly small-scale, cm-offset faults) observed in the same granodiorites are superimposed on the D2 stereonet. D1 structures are interpreted to be coeval with (or marginally postdate) the emplacement of the granodiorites, while D2 structures likely postdate granodiorite emplacement. The map locations of all major D1 and D2 structures in the Khoridol Saridag and northern mapping regions, as well as representative structural measurements, are presented in the Supplementary Information (fig. S1).

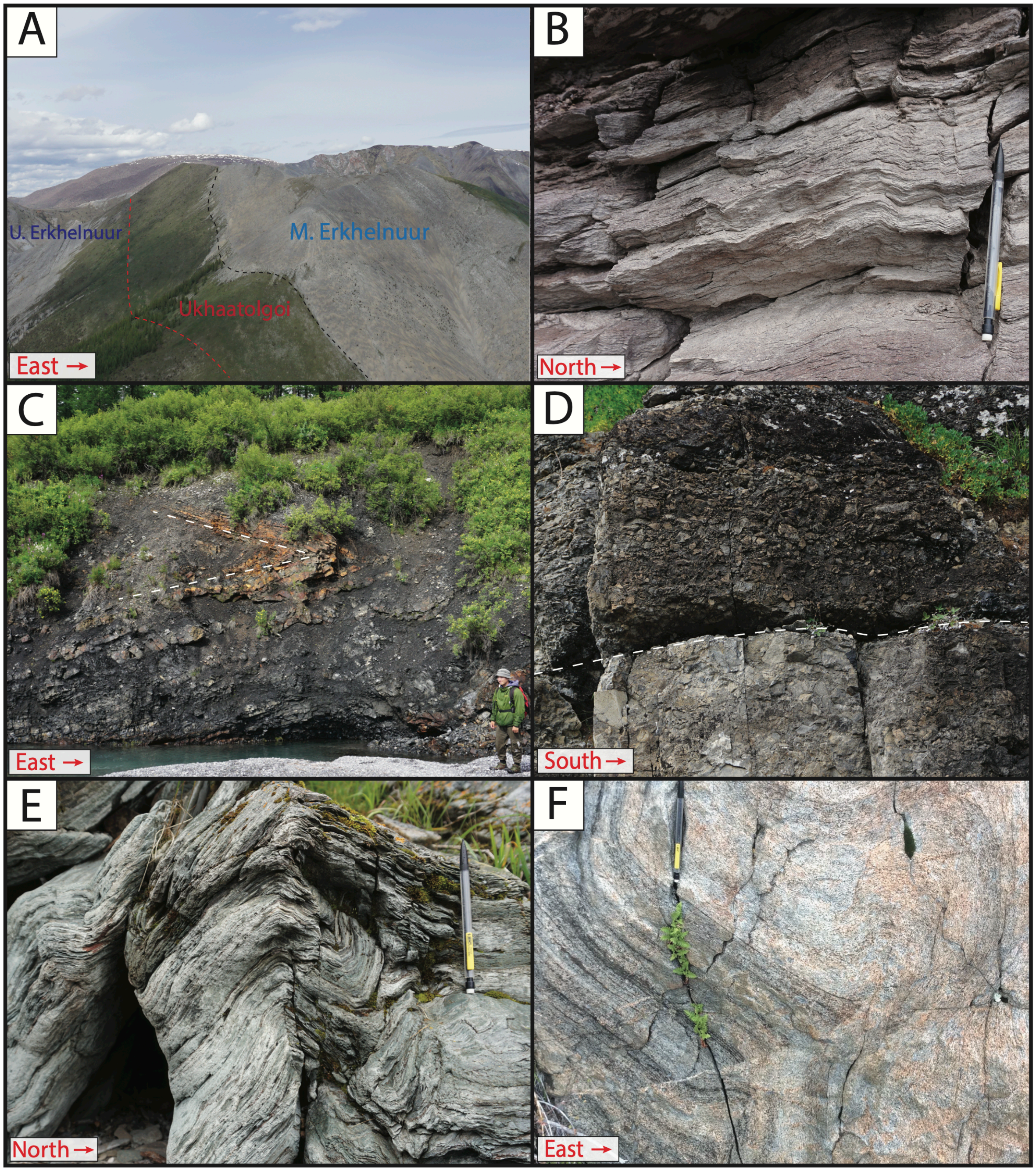


Figure 8. Field photographs detailing structural elements of the greater Khuvsgul study area. A) a laterally-discontinous sliver of Ukhaatolgoi Fm sediment forms the footwall of an east-dipping backthrust in the southeast Khoridol Saridag Range. B) crenulation cleavage in a fine-grained lithic wacke of a Sarkhoi Fm outcrop approximately 1 km north of the Arcai Gol Thrust. Elongated cleavage planes, dipping to the south-southwest, indicate shear in a top-to-the-north-northeast direction, consistent with the putative throw of the Arcai Gol Thrust. Primary bedding planes are dipping to the west (broadly into the page). C) chevron folds in the Salkhitai Mb of the Bakh Fm, eastern Darkhat Valley. Approximately 1.7-m-tall geologist for scale. Folds are broadly D1 parallel, and indicate eastward vergence, putatively associated with their proximity to D) cataclasites adjacent to a major east-dipping backthrust (fault surface highlighted with a white dashed line) running along the western margin of the Darkhat Valley and defining the western extent of the Khoridol Saridag Range. E) fabrics representative of those observed in siliciclastic lithologies across the Northern mapping area. F) foliations in granodiorite (EAGC1942) of the northern area are broadly axial-parallel to D1 structures. The mechanical pencil in panels B, E, and F is 15.5 cm in overall length.

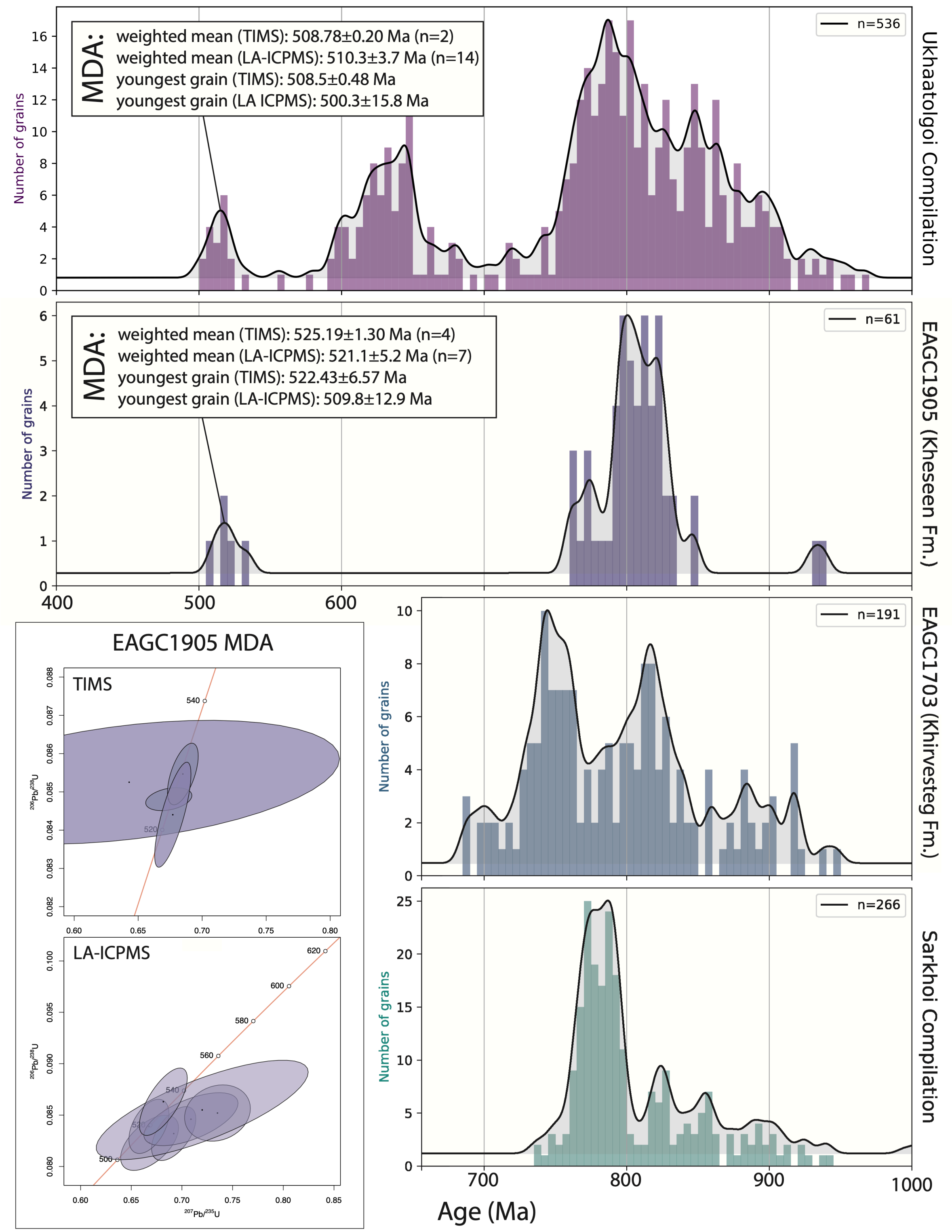


Figure 9. Detrital zircon age spectra from the Khuvsgul study area arranged by relative stratigraphic height. Upper inset panels show maximum depositional age (MDA) constraints for the Kheseen Fm. (EAGC1905) and the Ukhaatolgoi Fm. (compilation of multiple samples) respectively, as determined by the youngest grain and youngest population of zircon analyzed by both CA-ID-TIMS and LA-ICPMS. Lower left inset: concordia diagrams for CA-ID-TIMS and LA-ICPMS analyses of the youngest grains in EAGC1905. All sample locations and geochronological data are compiled in the Supplementary Information (Table S3).

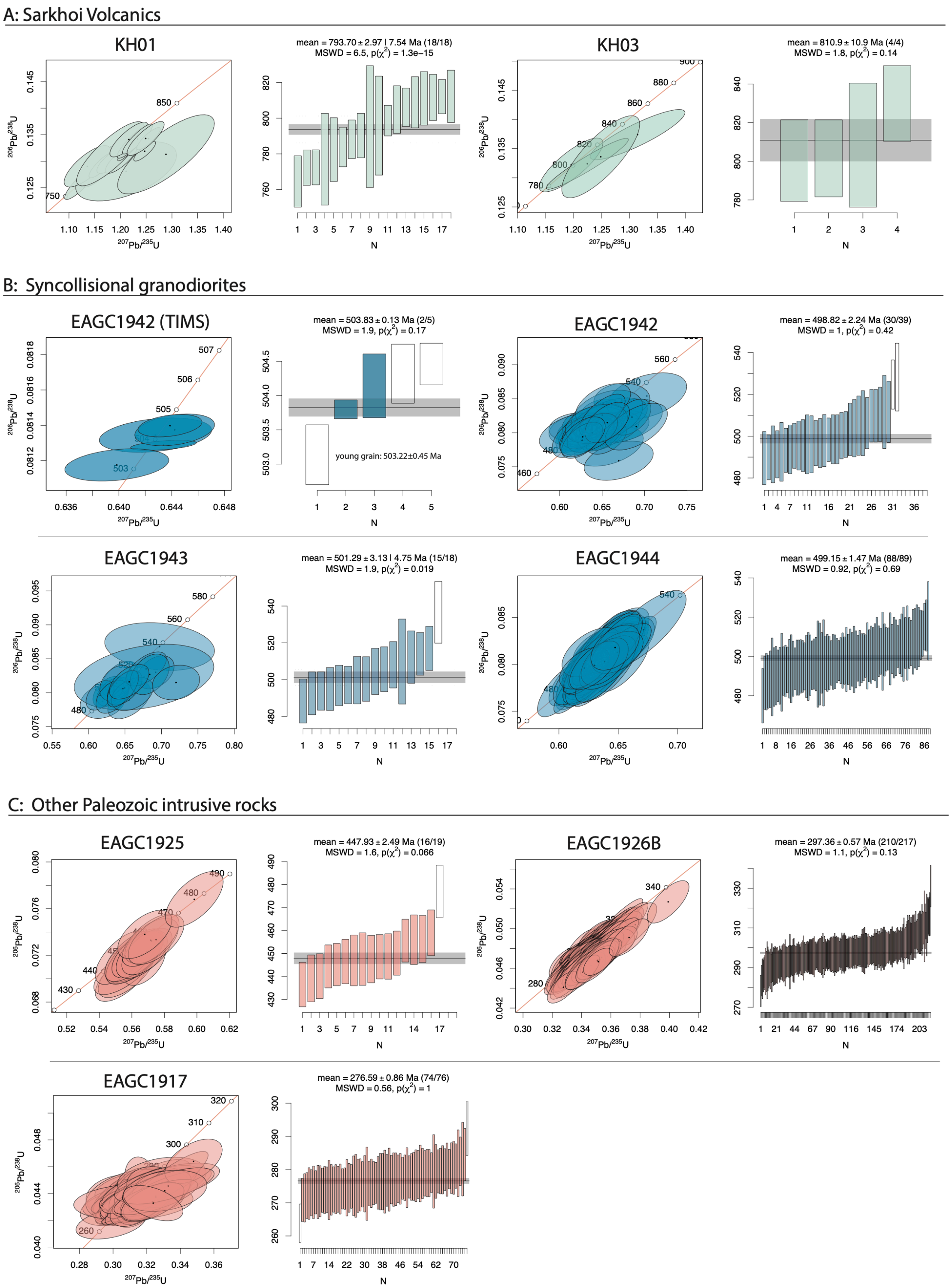


Figure 10. Concordia diagrams and weighted-mean plots for magmatic zircon populations from A) volcanic rocks of the Sarkhoi Fm, B) granodiorites from the northern mapping area and C) igneous intrusive rocks postdating D1/D2 deformational events. LA-ICPMS and CA-ID-TIMS data are collated in the Supplementary Information (Table S3).

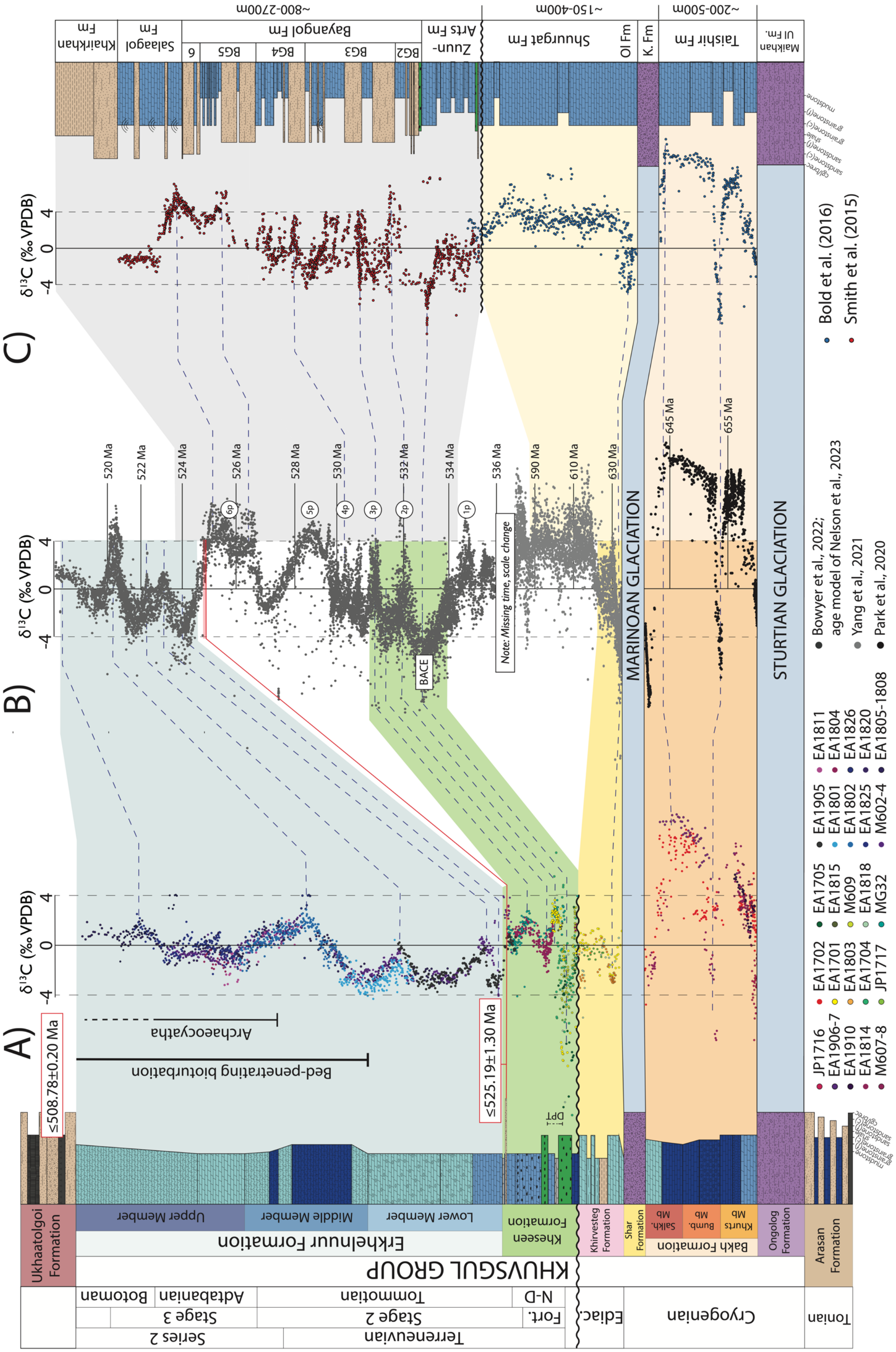
A)
B)
C)
δ13C (‰ VPDB)
KHUVSGUL GROUP
Erkhelnuur Formation
Upper Member
Middle Member
Lower Member
Kheseen Formation
Ukhaatolgoi Formation
Khirvesteg Formation
Shar Formation
Bakh Formation
Khurts Mb
Bumb. Mb
Salkh. Mb
Ongolog Formation
Arasan Formation
Terreneuvian
Series 2
Stage 2
Stage 3
Fort.
N-D
Tomotian
Atdabanian
Botoman
Ediac.
Cryogenian
Tonian
≤508.78±0.20 Ma
≤525.19±1.30 Ma
Bed-penetrating bioturbation
Archaeocyatha
DPT
MARINOAN GLACIATION
STURTIAN GLACIATION
BACE
Note: Missing time, scale change
520 Ma
522 Ma
524 Ma
526 Ma
528 Ma
530 Ma
532 Ma
534 Ma
536 Ma
590 Ma
610 Ma
630 Ma
645 Ma
655 Ma
1p
2p
3p
4p
5p
6p
Khairkhan Fm
Salaagol Fm
Bayangol Fm
BG2
BG3
BG4
BG5
6
Zuun-Arts Fm
Shuurgat Fm
Ol Fm
K. Fm
Taishir Fm
Maikhan Ul Fm.
~800-2700m
~150-400m
~200-500m
JP1716
EA1906-7
EA1910
EA1814
M607-8
EA1702
EA1701
EA1803
EA1704
JP1717
EA1705
EA1815
M609
EA1818
MG32
EA1905
EA1801
EA1802
EA1825
M602-4
EA1811
EA1804
EA1826
EA1820
EA1805-1808
Bowyer et al., 2022; age model of Nelson et al., 2023
Yang et al., 2021
Park et al., 2020
Bold et al. (2016)
Smith et al. (2015)

Figure 11. Age model and compiled chemostratigraphy for the Khuvsgul Group. A) a $\delta^{13}C$ compilation from the Khuvsgul group is correlated with B) a global $\delta^{13}C$ compilation and C) a composite $\delta^{13}C$ chemostratigraphy from Cryogenian-Cambrian strata of the Zavkhan Terrane. Note that while we use the global chemostratigraphic compilation of Bowyer et al. (2022), we utilize the Cambrian age model of Nelson et al. (2023).

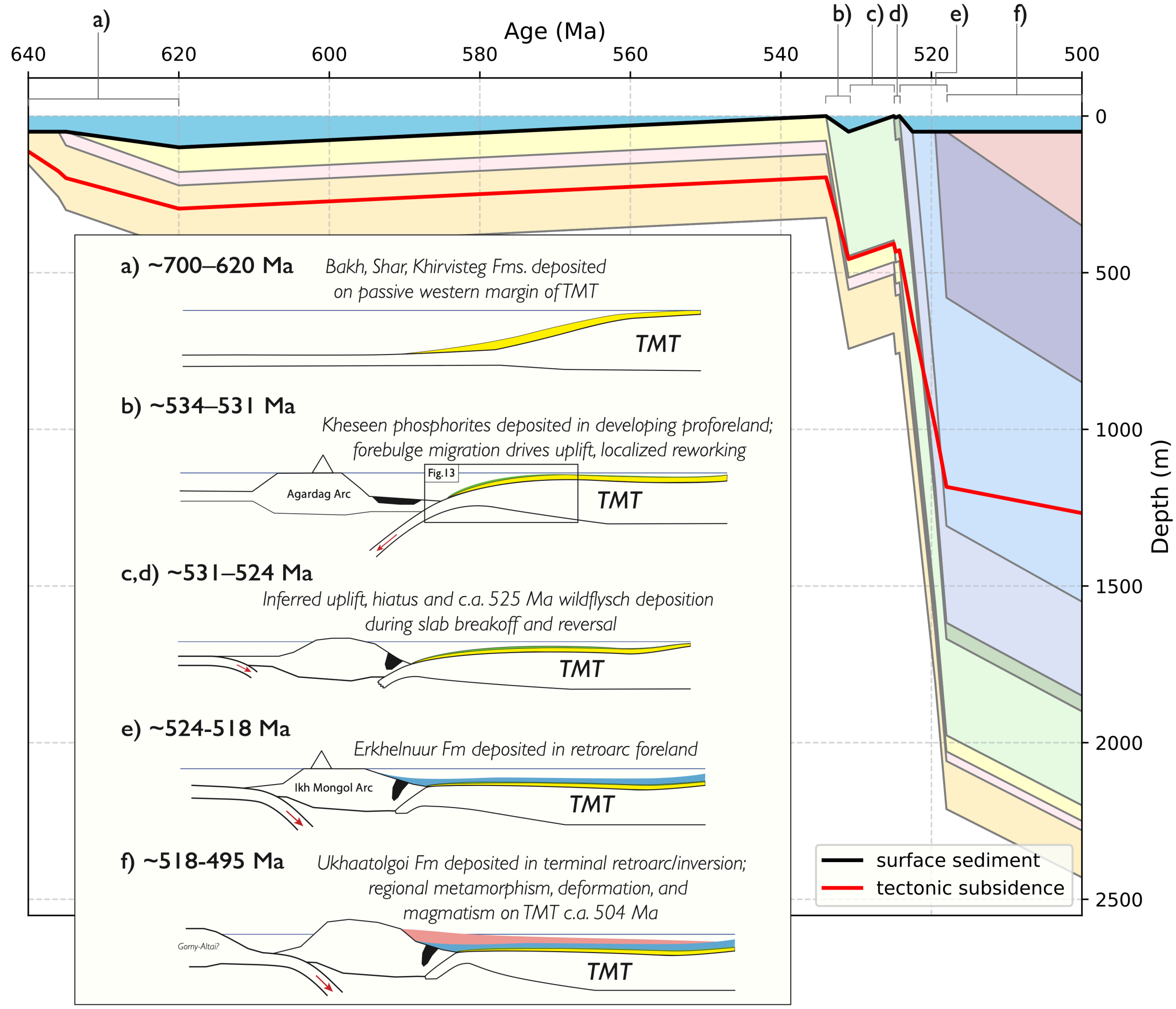


Figure 12. Tectonic subsidence model for the Khuvsgul Group, paired with a schematic tectonic model (inset panel) of the western margin of the Tuva-Mongolia Terrane in Khuvsgul Group time. a) passive margin deposition occurred along the western margin of the TMT during the Cryogenian and early Ediacaran, prior to a prolonged depositional hiatus along the margin. b) deposition of the fossiliferous phosphorites of the Kheseen Fm occurred in a pro-foreland basin associated with the approaching Agardag Arc; see figure 13 for detailed schematic of phosphogenic environment. c,d) collision of the Agardag Arc resulted in slab breakoff and subduction polarity reversal; uplift associated with these events inverted the pro-foreland, caused putative erosion/hiatus, and resulted in the deposition of wildflysch in the eastern Khoridol Saridag Range. e) resumption of E-dipping subduction along the western margin resulted in Ikh-Mongol Arc magmatism, and the deposition of the Erkhelnuur Fm into the Ikh-Mongol retroarc foreland. f) collision along the western margin of the Ikh-Mongol arc resulted in regional metamorphism, inversion of the retroarc foreland, deposition of the Ukhaatolgoi Fm., and the emplacement of granodiorites c.a. 504 Ma.

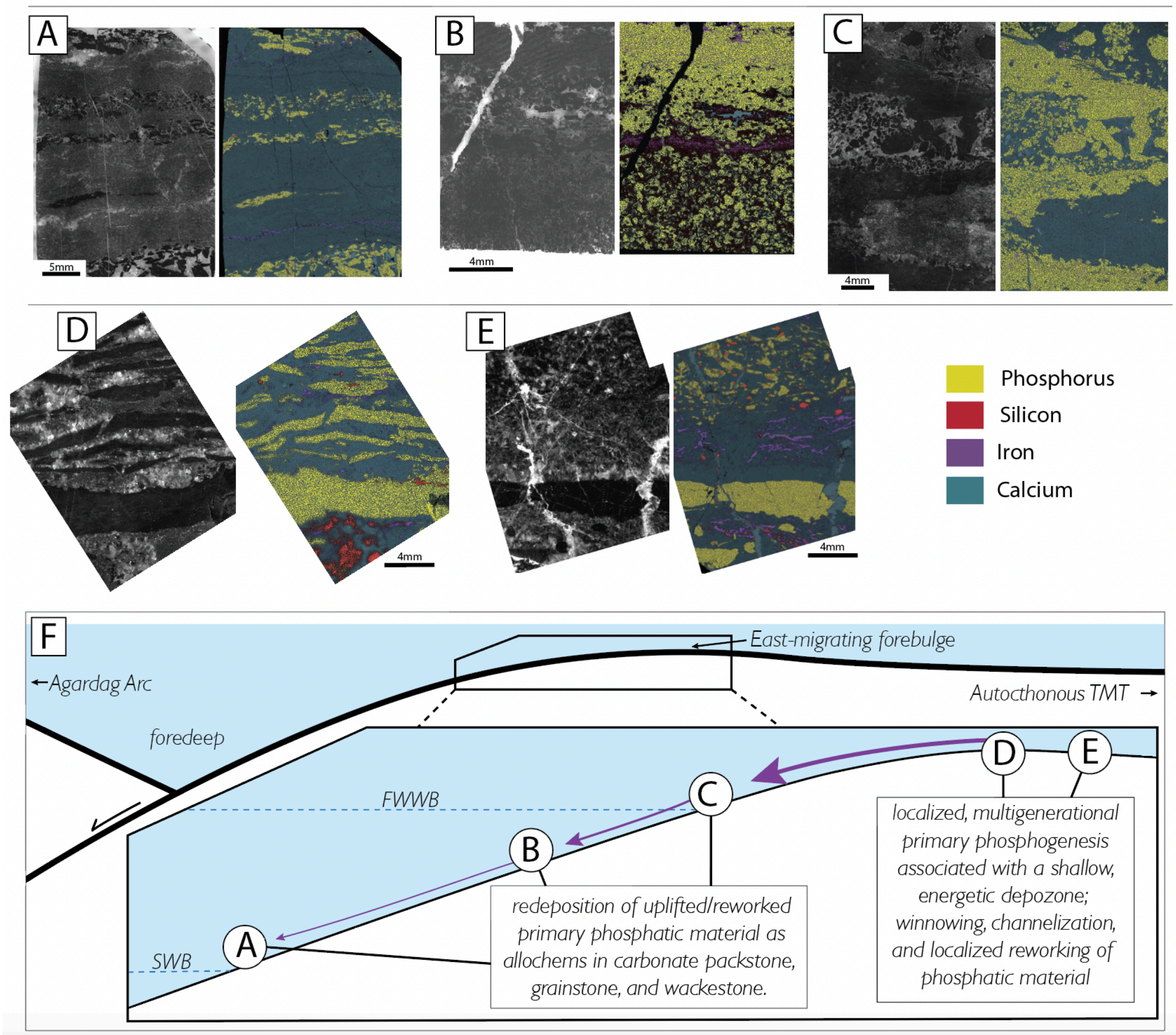


Figure 13. Kheseen Fm. phosphorite facies, presented as a thick-section photograph (left) and micro-XRF-derived elemental map (right). A) phosphatic allochems within grainstone horizons in interbedded limestone grainstone and mudstone. B) fining upward grainstone predominantly composed of phosphatic grains, with infrequent void-filling micritic cement. C) cross-bedded phosphatic wackestone and limestone grainstone. Note variably angular phosphatic clasts in coarsest wackestone horizon. D) Phosphatic hardground and overlying intraclast breccia, with tabular phosphatic clasts supported in a limestone grainstone matrix. Note siliceous cementation of limestone grainstone below basal phosphatic hardground. E) Phosphatic hardground, below limestone grainstone and wackestone with angular phosphatic and chert allochems. F) cartoon schematic model of the Kheseen Fm. phosphogenic sedimentary environment. The putative depositional environments of phosphorite facies A-E are shown, with predominantly-reworked facies (A-C) occurring at or below fair-weather-wave base (FWWB), and likely above storm-wave base (SWB). Facies D and E are indicative of primary, multigenerational phosphogenesis in a shallow, energetic environment, likely on a banktop/local topographic high. The development of locally-variable topography was likely mediated by the eastward migration of a forebulge associated with the collision of the Agardag Arc.

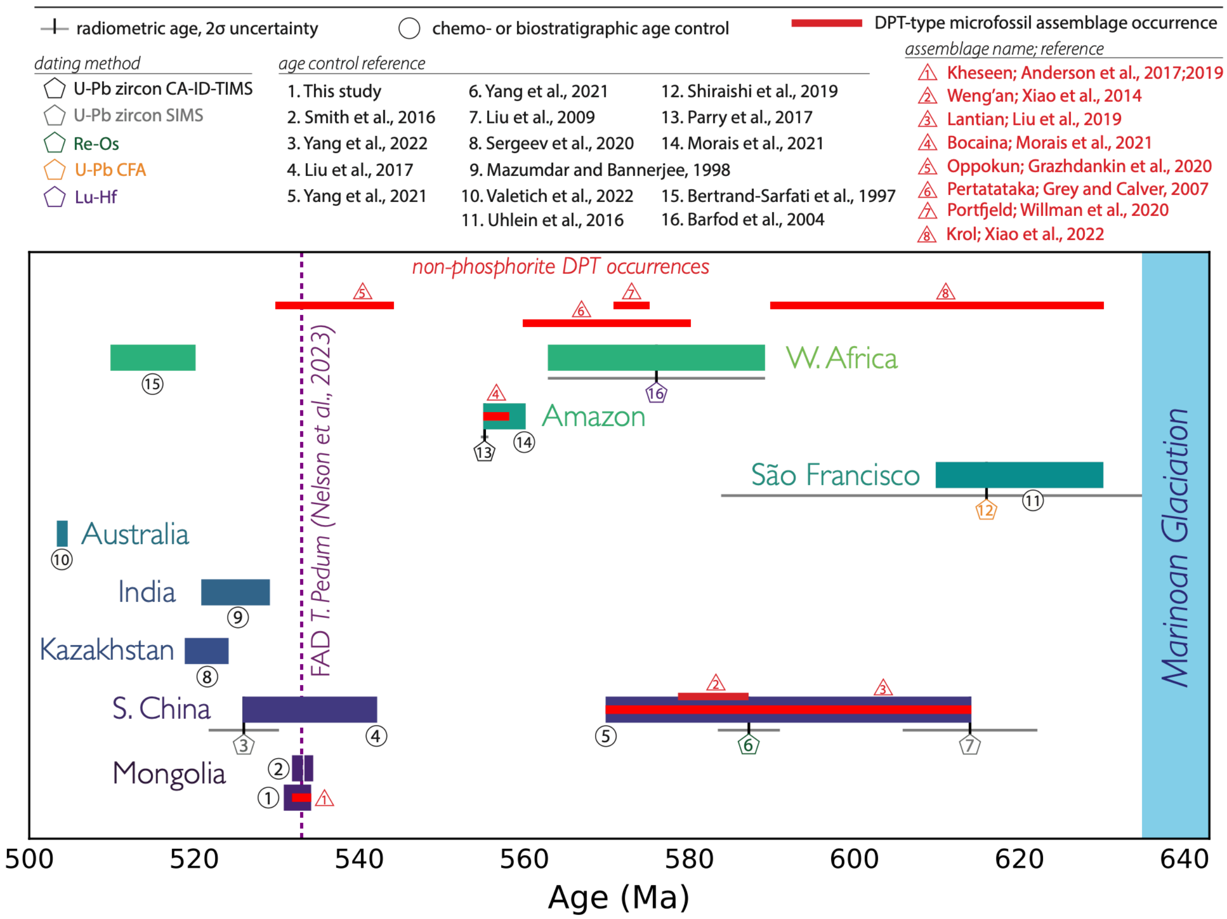


Figure 14. Age and duration of Ediacaran and Cambrian phosphorite occurrences, grouped by craton. The temporal range of Doushantuo-Pertatataka-Type microfossil assemblages, including those not associated with phosphorites, are depicted in red.

# SUPPLEMENTARY INFORMATION: Cambrian foreland phosphogenesis in the Khuvsgul Basin of Mongolia

**Eliel S. C. Anttila[1a*], Francis A. Macdonald[1b], Blair Schoene[2], and Sean P. Gaynor[2c]**
*[1]Department of Earth Science, University of California Santa Barbara, Santa Barbara, CA, 93117, USA*
*[2]Department of Geosciences, Princeton University, Princeton, NJ, 08544, USA*
*[a]Now at the Department of Earth Sciences, ETH Zürich, Zürich, 8092, CH*
*[b]Now at the Department of Earth and Planetary Science, University of California Berkeley, Berkeley, CA, 94720, USA*
*[c]Now at the Geology, Geophysics, and Geochemistry Science Center, United States Geological Survey, Denver, CO, 80225, USA*
**Corresponding author: eanttila@ethz.ch*

This supplementary information includes a simplified geological map highlighting the structural features of the Khoridol-Saridag and portions of the northern mapping regions (fig. S1) of the Khuvsgul Group study area, a geological map of the northern mapping region (fig. S2), and a geological map of the Darkhat Valley mapping region (fig. S3). Photomicrographs of thin sections from intrusive igneous geochronological samples are shown in figure S4. Figure captions for each supplemental figure are collated below.

Also included are several tables detailing the locations of all measured sections referenced in the text (Table S1), all carbonate chemostratigraphic data (Table S2), all geochronological data (Table S3), and all parameters used to build the tectonic subsidence model for the Khuvsgul Group (Table S4).

Code used to generate figures for the main manuscript text can be accessed at:

https://github.com/eliel-anttila/Anttila_et_al_Khuvsgul_2024.git

* * *

# SUPPLEMENTARY FIGURES

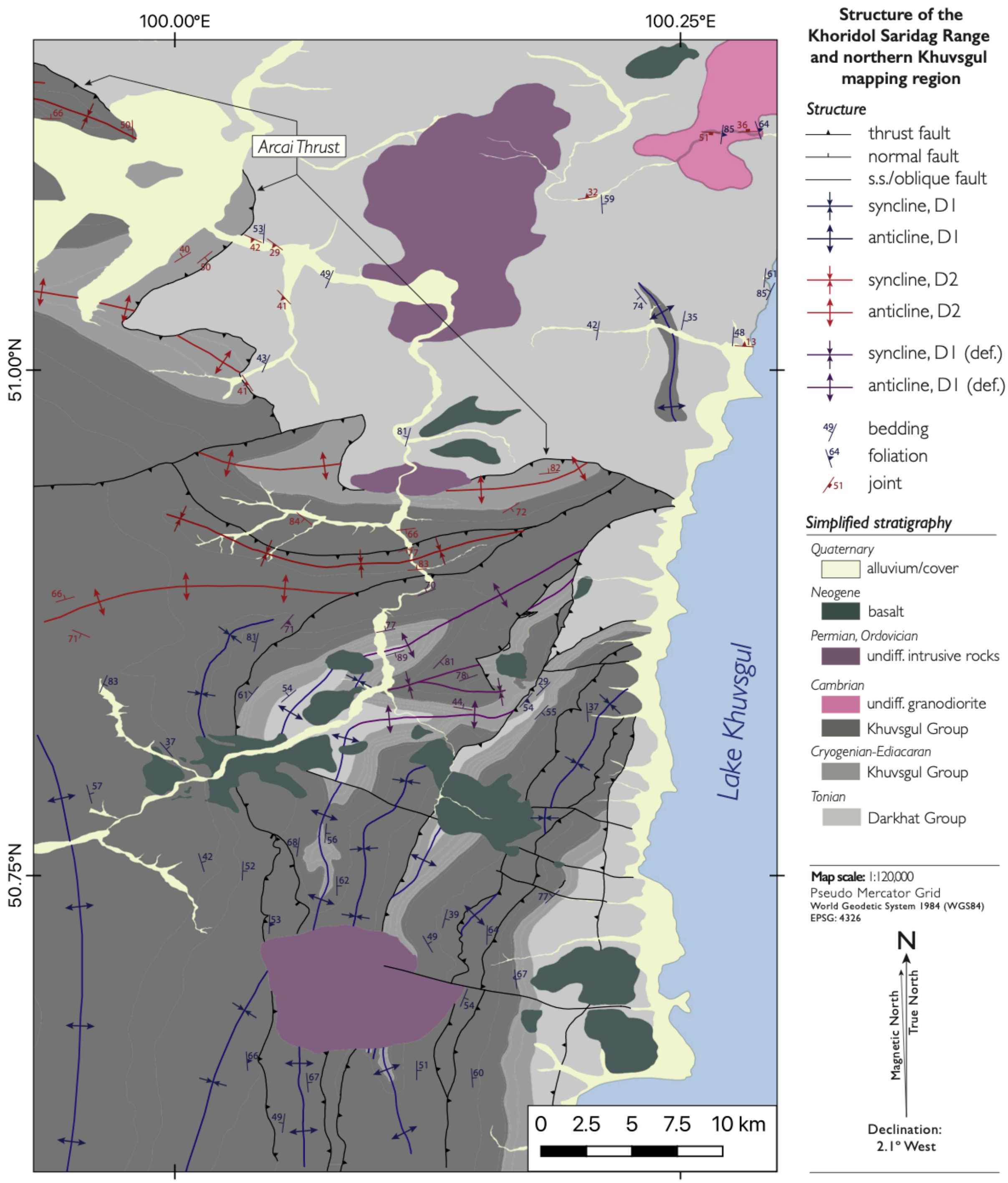


Figure S1. Simplified geological map of the Khoridol Saridag and a portion of the northern mapping areas, highlighting structural data. Structures and data associated with dominantly E-W trending compression (D1) are colored dark blue, while structures and data associated with later NNE-SSW-trending compression (D2) are colored red. Purple structures and data indicate D1 structures that were subsequently deformed during D2. The position of the Arcai Thrust, which superimposes the para-allochthonous Khuvsgul Group strata that make up the Khoridol Saridag Range atop autocthonous Darkhat Group and Khuvsgul Group sequences, is indicated by the black arrows towards the top of the map.

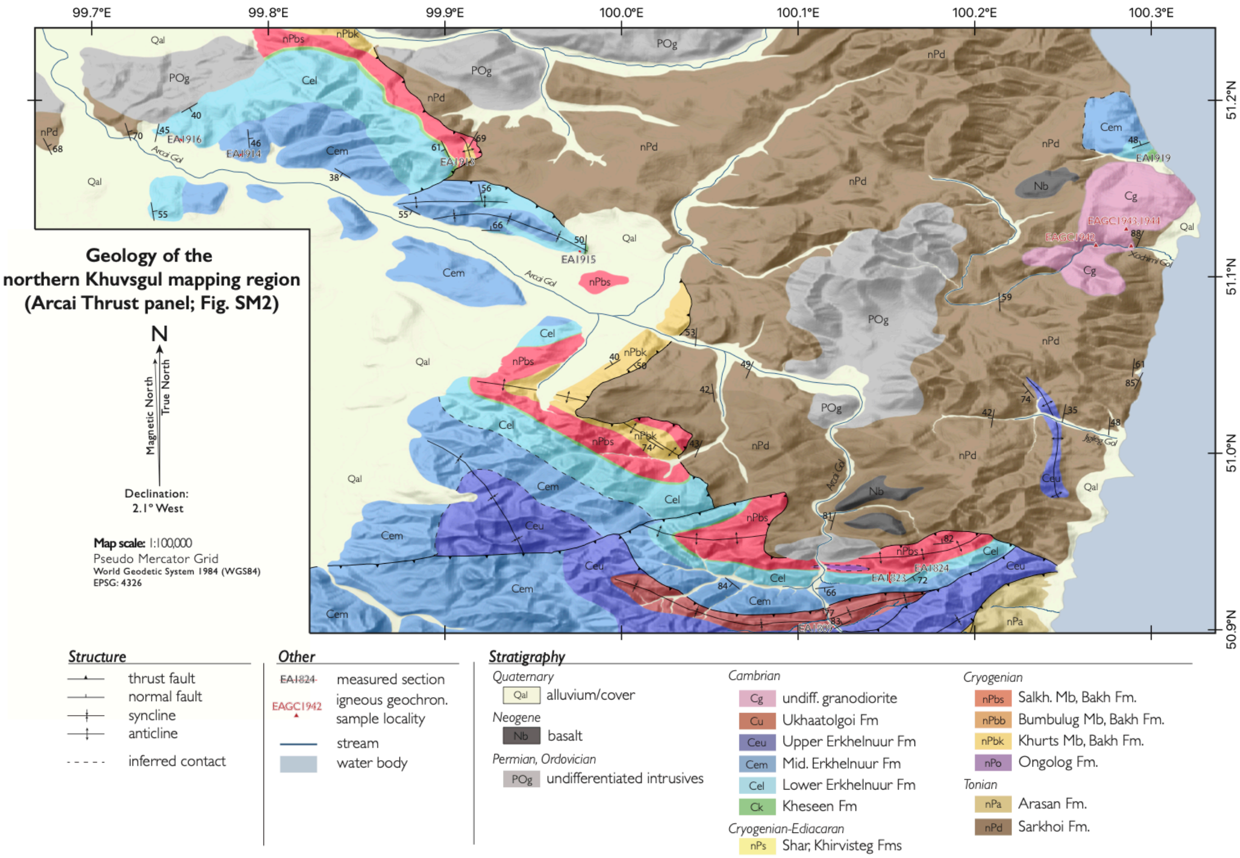


Figure S2. Original geological map of the northern mapping region.

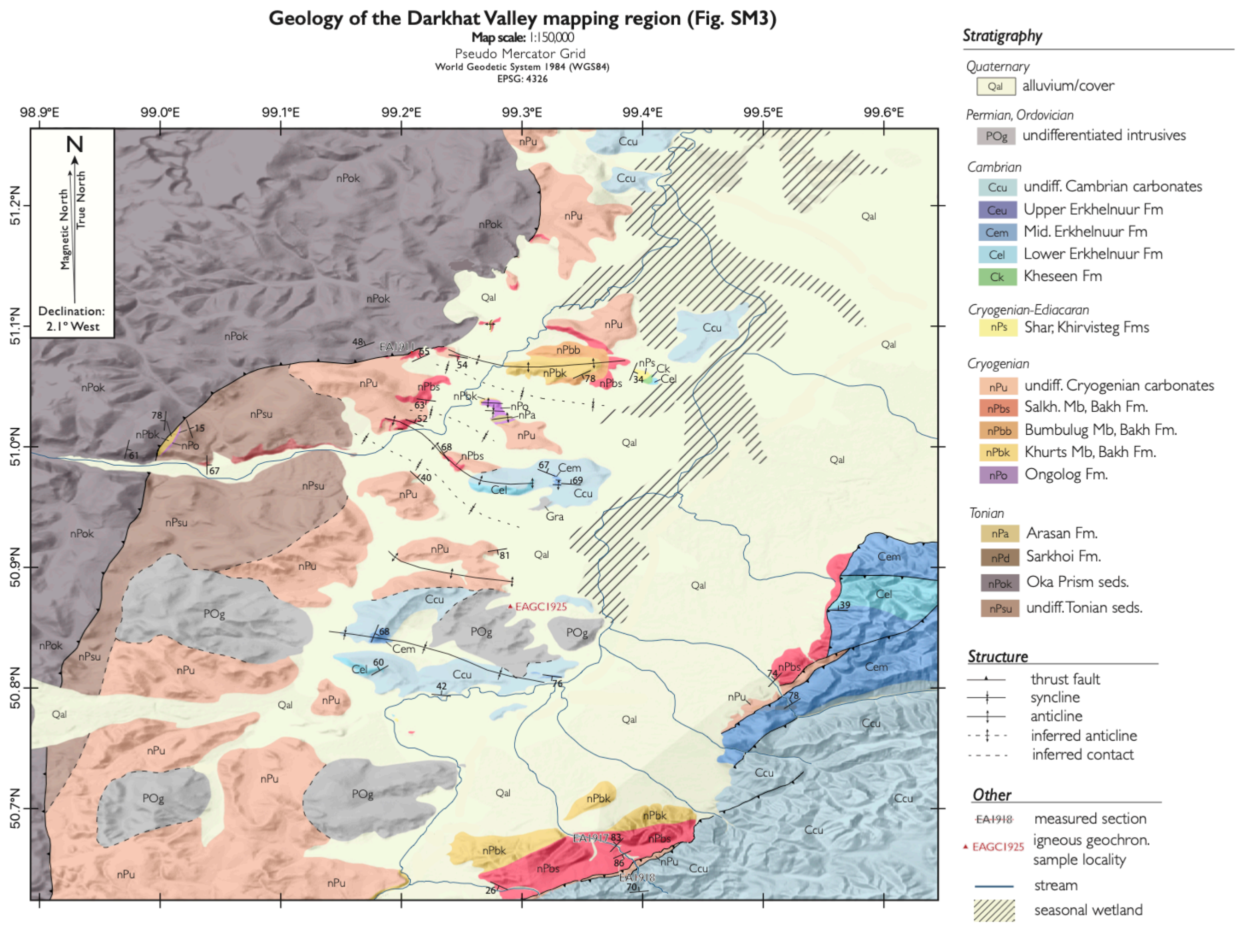


Figure S3. Original geological map of the Darkhat Valley mapping region.

2524 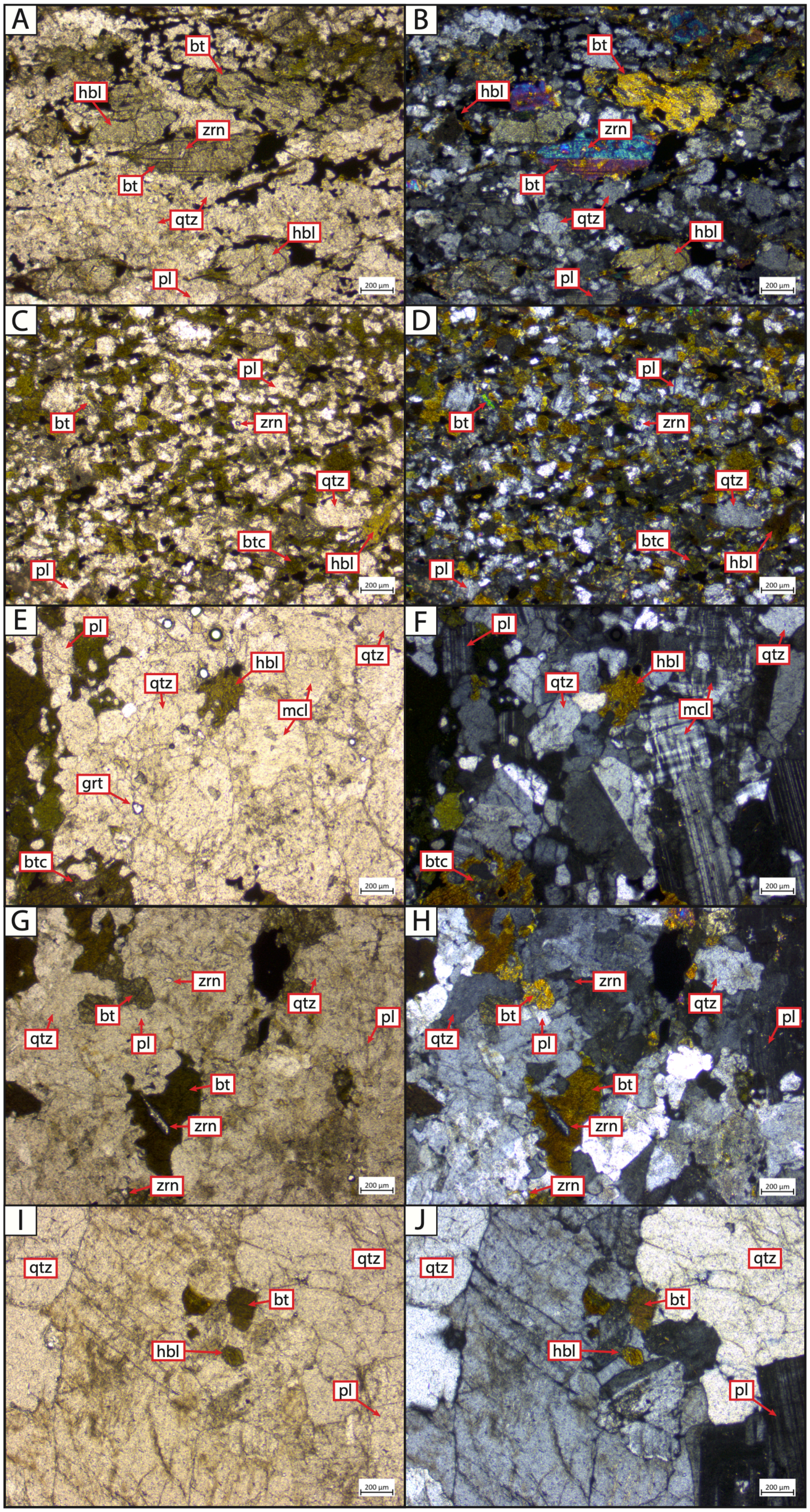

Figure S4. Thin-section photomicrographs of intrusive igneous geochronological samples. qtz=quartz, pl=plagioclase, bt=biotite, hbl=hornblende, zrn=zircon, btc=chloritized biotite, mcl=microcline. Detail of a foliated portion of sample EAGC1942 in plane-polarized (panel A) and cross-polarized (panel B) transmitted light. Note partially-chloritized biotite at top-right of both panels, as well as a zircon inclusion within the biotite at the center of both panels. Detail of a dark band in heavily-foliated portion of sample EAGC1943, in plane polarized (panel C) and cross-polarized (panel D) transmitted light. Chloritized biotite is visible throughout both panels, with infrequent, unaltered biotite and partially-altered hornblende. Gneissic textures in thin section reflect heavy foliation observable in both hand-sample and in outcrop. Portion of sample EAGC 1944 in plane polarized (E) and cross-polarized (F) transmitted light. Note chloritized biotite at bottom left of both panels, as well as microcline with well-developed tartan twinning, at center-right of both panels. Detail of a portion of sample EAGC1925, in plane polarized (G) and cross-polarized (H) transmitted light. Note zircon within biotite (center-left, both panels). Detail of a portion of sample EAGC1926B, in both plane polarized (I) and cross-polarized (H) transmitted light.

* * *